Otto Scheibelhofer

Spectroscopic Methods for Pharmaceutical Process and Product Quality Monitoring

DOCTORAL THESIS

For obtaining the academic degree of

Doktor der technischen Wissenschaften

Doctoral Programme of Technical Sciences
Technical Physics

Graz University of Technology

Graz University of Technology

Supervisor:

Ao.Univ.-Prof. Mag. Dr.rer.nat. Robert Schennach

Institute of Solid State Physics

in cooperation with

Research Center Pharmaceutical Engineering GmbH

Graz, August 2014

Scheibelhofer Otto
Spectroscopic Methods
for Pharmaceutical Process and
Product Quality Monitoring
Dissertation

First assessor
Ao. Univ.-Prof. Mag. Dr.rer.nat. Robert Schennach
Institute of Solid State Physics,
Graz University of Technology

Second assessor
Prof. Dr. Dr. h.c. Peter Kleinebudde
Institute of Pharmaceutics and Biopharmaceutics,
Heinrich-Heine-Universität Düsseldorf

This document was written with TeXnicCenter, typeset with LaTeX, based on KOMA script, and compiled with pdfLaTeX2e and `Biber`.

Deutsche Fassung:
Beschluss der Curricula-Kommission für Bachelor-, Master- und Diplomstudien vom 10.11.2008
Genehmigung des Senates am 1.12.2008

EIDESSTATTLICHE ERKLÄRUNG

Ich erkläre an Eides statt, dass ich die vorliegende Arbeit selbstständig verfasst, andere als die angegebenen Quellen/Hilfsmittel nicht benutzt, und die den benutzten Quellen wörtlich und inhaltlich entnommenen Stellen als solche kenntlich gemacht habe.

Graz, am ……………………………   ………………………………………………..
(Unterschrift)

Englische Fassung:

STATUTORY DECLARATION

I declare that I have authored this thesis independently, that I have not used other than the declared sources / resources, and that I have explicitly marked all material which has been quoted either literally or by content from the used sources.

……………………………   ………………………………………………..
date   (signature)

Abstract

The application of near-infrared spectroscopy in the pharmaceutical industry is an active field of research that has brought forward many interesting results in the last years.

The distinguishing criteria of this thesis is the application of multipoint set-ups. This is, not only a single probe is used in a pharmaceutical unit operation to determine the process state and the product quality, but several probes at different positions are harnessed, to enhance the gained knowledge. The availability of several positions not only brings repetition of the same information, but enables the mapping of concentration gradients, sensor functionality self-checks, tracing of material and much more.

Hence, for the correct use of several probes, their comparability has to be ensured, which is the starting point of this thesis. Different realizations of multiprobeable set-ups, namely fiber multiplexing, chemical imaging, and fiber-to-imaging adapters were used.

For blending processes, traditionally sampling is a big issue. Hence, the new options available when applying a multiprobe set-up for sampling have been explored. This has direct consequences on how a blending state can be assessed.

As a second process, fluid-bed coating was investigated. The correct positioning of a sensor in a fluid bed is a tender task, as a compromise has to be found between a suitable position and the stability of the air flow pattern in the fluid bed. Window fouling turned out to be a critical issue, and a method to circumvent biased measurements by fouling was introduced.

Kurzbeschreibung

Die Anwendung von Nahinfrarot-Spektroskopie in der pharmazeutischen Industrie ist ein aktiver Forschungsbereich und hat in den letzten Jahren viele Ergebnisse gezeitigt.

Das herausstechende Merkmal der vorliegenden Dissertation ist die Anwendung von Multisondensystemen. Dies bedeutet, dass nicht nur eine Sonde in einer Produktionseinheit verwendet wurde um den Prozess und die Produktqualität zu bewerten, sondern mehrere Sonden an mehreren Positionen eingesetzt wurden um das Wissen über den Prozess zu vervielfältigen. Der Einsatz mehrerer Sonden bringt nicht nur eine Wiederholung der vorhandenen Information, sondern ermöglicht unter anderem die Erkennung des Verlaufs von Konzentrationen, die gegenseitige Kontrolle von Sensoren, die Verfolgung von Materialflüssen, und vieles mehr.

Für den korrekten Einsatz von mehreren Sonden ist es notwendig, die Vergleichbarkeit der Messungen zu sichern; dies ist der Startpunkt dieser Dissertation. Verschiedene Möglichkeiten der Realisierung von Mehrsondensystemen wurden verwendet, namentlich Faserschalter, bildgebende Spektroskopie, und Projektion von mehreren Sonden auf ein bildgebendes System.

Für Mischprozesse ist die korrekte Probenahme seit jeher ein wichtiges Thema. Durch die Möglichkeit von Multisondensystem eröffnen sich bisher nicht durchführbare Wege zur Bestimmung der Mischhomogenität, die hier dargestellt und diskutiert werden.

Als weiterer Prozess wurde die Beschichtung von Partikeln in einer Wirbelschicht betrachtet. Die korrekte Positionierung von Sonden wird hier durch die Empfindlichkeit der Strömungsverhältnisse erschwert. Es hat sich herausgestellt, dass die Belegung der Nahinfrarotsonden kritisch im betrachteten Prozess ist; Daher wurde eine Methode dies zu korrigieren entwickelt, die ebenfalls hier vorgestellt werden soll.

Table of Contents

Abstract . . . vii
Kurzbeschreibung . . . viii

Table of Contents ix

Motivation . . . 1
Outline . . . 2
Published Work . . . 3

1 Introduction 5
1.1 Near-Infrared Spectroscopy for Process Monitoring . . . 5
  1.1.1 Process Analytical Technology . . . 5
1.2 Near Infrared Spectroscopy as PAT-Tool . . . 6
  1.2.1 Applications of NIR Spectroscopy in the Pharmaceutical Industries . . . 7
  1.2.2 Regulatory Requirements for NIR in the Pharmaceutical Environment . . . 8
  1.2.3 Trends in NIR . . . 8
1.3 The Application of Hyperspectral Imaging . . . 9
1.4 The Application of Multipoint Near-Infrared Spectroscopy . . . 10
1.5 Controlled Blending Processes via NIR . . . 12

2 Theoretical Background 15
2.1 Near-Infrared Light and Matter Interaction . . . 15
  2.1.1 Properties of Light . . . 15
  2.1.2 Interaction of Light and Matter . . . 15
  2.1.3 Absorption . . . 16
  2.1.4 Scattering . . . 18
  2.1.5 Description of Diffuse Reflection . . . 19
  2.1.6 Modes of Measurements . . . 20
2.2 Near-Infrared-Spectroscopy . . . 21
  2.2.1 Spectrometer Instrumentation . . . 21

2.2.2 Near-Infrared Probes . . . 24
2.2.3 Quantitative Spectral Interpretation . . . 25
2.3 Multivariate Data Analysis for The Interpretation of Spectra . . . 26
2.3.1 Spectral Transformations . . . 26
2.3.2 Variable Scaling . . . 32
2.3.3 Principal Component Analysis (PCA) . . . 33
2.3.4 Multiple Linear Regression (MLR) . . . 39
2.3.5 Projection to Latent Space (PLS) . . . 40
2.3.6 Alternative Methods for Quantitative Spectral Interpretation 45
2.4 Mixing of Solids . . . 46
2.4.1 Mechanisms of Mixing and Segregation . . . 46
2.4.2 Mixture Homogeneity . . . 47
2.4.3 Concept of Depth of Scrutiny . . . 49
2.4.4 Determining Homogeneity In-Process . . . 50
2.4.5 Confidence on Concentration and Homogeneity . . . 51
2.5 Fluid Bed Coating . . . 52

3 Materials and Devices 53
3.1 Spectrometers . . . 53
3.2 Optical Devices . . . 55
3.2.1 Near-Infrared Probes . . . 56
3.3 Powder Handling . . . 57
3.4 Analytic Devices . . . 59
3.5 Software . . . 59
3.6 Materials . . . 60

4 Determination of Equivalency for Multipoint Measurements 63
4.1 Equivalency of Measurements . . . 63
4.2 Concept of A Multipoint Spectrometer . . . 63
4.2.1 Hardware and Software Aspects . . . 64
4.2.2 Calculation of Absorbance . . . 66
4.3 Performance of The Instrument . . . 66
4.3.1 Single Channel Performance . . . 67
4.3.2 Port Comparison . . . 75
4.3.3 Short and Long Term Stability . . . 80
4.3.4 Effect of Integration Time . . . 84
4.3.5 Binning . . . 84
4.3.6 Comparison of Different Probes . . . 86
4.3.7 Conclusion . . . 87

4.4 Test of Equivalency with Multivariate Methods 88
4.4.1 Expanded Factor Set 88
4.4.2 The Ideal Test Case 89
4.4.3 The Non-Ideal Case 90
4.5 Example Applications 93
4.5.1 Self Correction and Calibration 93

5 Experiments and Results **97**
5.1 Calibration On The Rotating Disk 97
5.1.1 Accurate Estimation of The Particle Volume 97
5.1.2 Determination of Sample Volume 100
5.1.3 Conclusion 107
5.2 Penetration Depth 108
5.3 Continuous Dosing 111
5.3.1 Introduction 111
5.3.2 Experimental Set-Up and Spectral Interpretation Techniques 111
5.3.3 Monitoring Impurities 114
5.3.4 Monitoring Powder Flow 115
5.3.5 Depth of Scrutiny 117
5.3.6 Conclusion 120
5.4 Batch Blending Process 121
5.4.1 Introduction 121
5.4.2 Experimental Set-Up 121
5.4.3 Establishment of The Chemometric Model 122
5.4.4 Sampling Considerations with NIRS in the Blending Vessel 124
5.4.5 Time-Evolution of Blending: Concentration Levels 126
5.4.6 Time-Evolution of Blending: Homo- and Heterogeneity . . 130
5.4.7 Improvement of The Chemometric Model 133
5.4.8 Different Blending Conditions 139
5.4.9 Conclusions 147
5.5 Continuous Blending Process 150
5.5.1 Introduction 150
5.5.2 Preparation Steps 150
5.5.3 Experiments at The Blender 151
5.5.4 Conclusion and Remarks 154
5.6 Window Fouling in A Coating Process 156
5.6.1 Introduction 156
5.6.2 Experimental Setup 157
5.6.3 Spectral Interpretation 158

5.6.4 Process Examples 170
5.6.5 Results 173

6 Summary and Conclusion 175

Danksagung (Acknowledgments) 179

List of Figures 181

List of Tables 185

Bibliography 187

Motivation

Talking about light, most people think of the optical region naturally. This is a limitation of our eye. Light in the infrared range can be perceived with our skin by the sensation of heat, but this does not allow us the reconstruction of an image of the surroundings. Quite interestingly, while several animals have a much broader range of perception and can detect ultraviolet light, the detection of near-infrared light is rather rare, as as a prerequisite, the detecting element must be cooler than the surroundings.

The detection of light, to asses the surroundings, is useful over a large range of scales (from sub-millimeter up to several kilometers). Indeed the ability to "see", by cameras and optical sensors, is harnessed in a variety of applications. The pharmaceutical industry which is in need to guarantee high quality standards, is now adopting near-infrared measurement systems for that purpose.

Preferring near-infrared over the more familiar optical range is dictated by a simple fact: *Most pharmaceutical powders are white.* This is caused by their particle size leading to intense scattering. Hence the perceived optical image of a heap of powder is isotropic at all wavelengths, and appears white. At larger wavelengths, as in the near infrared region, absorption becomes more dominant over scattering, hence powdered substances are "colored" again, allowing to distinguish them. An example of this effect is shown in Figure 0.1. In the mid-infrared region, this effect is even more enhanced. Unfortunately, absorbance is then so excessive that sample preparation is necessary, and the sample to be analyzed cannot be penetrated as deep as it would seem necessary.

Thus, near-infrared spectroscopy is the tool of choice, to monitor remotely, but efficiently, a plethora of different processes and to ensure product quality.

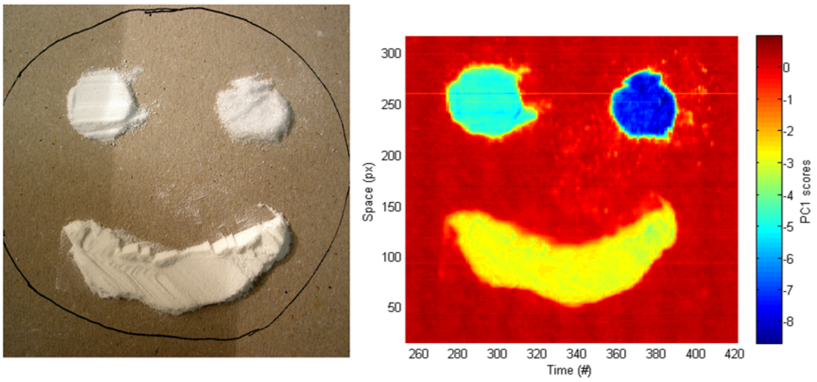

Figure 0.1: Although for the naked eye, most powders look white and similar (as shown left), they can be distinguished in the near-infrared region (as shown on the right; the color encodes the score of the first principle component of the obtained NIR spectra).

Outline

Near Infrared (NIR) spectroscopy is a versatile tool for assessing process states and quality. In the first chapter (Chapter 1) the reasons for the favorite role of NIR are explained, and the state of the art regarding NIR applications in the pharmaceutical industry is given. Hyperspectral imaging will be explained, and the reasons, why sometimes it is beneficial to use a probe setup instead of an imaging one (or vice versa).

In the second chapter (Chapter 2) the physical background of absorption spectroscopy will be explained shortly. Furthermore, the case of diffuse reflectance spectroscopy is described and discussed. Also, a mathematical description of the chemometric methods used, especially principal component analysis (PCA), projection to latent space (PLS), and alternatives are explained. Types of spectral pretreatments and their effects are introduced.

Complementary, the pharmaceutically relevant process step of blending is discussed. The linkage of multipoint/multiprobe setups, theory of sampling and depth of scrutiny of the given applications is established.

After providing the necessary scientific context, the instrumentation which was used is presented. The experimental devices are described in Chapter 3, with a special focus on the spectrometers, and the different set-ups enabling spectroscopic monitoring at several distinct positions in a process at the same time.

The next chapter (Chapter 4) deals with the concept of measuring at several positions, and the avoidance of problems with calibration transfer.

Subsequently (Chapter 5), the results of the experiments (i.e. blending of powder and coating of substrate particles), are presented and discussed. The focus is herein on the consequences of the multipoint set-up. The value adding of monitoring several positions with different blending dynamics, the possibilities of cross checks by multiple sensors, and so on, is discussed. Furthermore, the often occurring problem of window fouling is discussed and a possible solution presented.

The final chapter (Chapter 6) is highlighting the application of multipoint set-ups, and the more stringent interpretations enabled by said set-ups, compared to single probes. It is shown that a multipoint setup is beneficial in terms of process understanding, while the needed effort is just slightly larger, although data handling of such set-ups can be fatiguing.

An appendix discussing practical aspects in data handling is enclosed (not in all printed versions). It contains excerpts of created source code files to illustrate data treatment.

Published Work

Parts of this thesis have already been published in scientific journals:

O. Scheibelhofer, D. M. Koller, P. Kerschhaggl, J.G. Khinast; "Continuous Powder Flow Monitoring via Near-Infrared Hyperspectral Imaging" In: IEEE International Instrumentation and Measurement Technology Conference (I2MTC) Proceedings. 2012, pp. 748–753.

> The experimental part and the writing of this paper was done by myself. Helpful ideas and supervision, as well as organizational work was done by D. Koller. I want to thank P. Kerschhaggl for providing the spectrometer and software. The necessary infrastructure was provided by the RCPE under the scientific lead of J. Khinast.

O. Scheibelhofer, N. Balak, D. M. Koller, J.G. Khinast; "Spatially Resolved Monitoring of Powder Mixing Processes via Multiple NIR-Probes" In: Powder Technology 243 (2013) pp. 161–170.

> The experimental work mentioned in the text was done by myself. However, important preliminary work, regarding the integration time of the spectra, the first application of the turntable for the acquisition of calibration spectra, the modification of the turntable, and the first trial runs were done by N. Balak. The basic idea and the construction of the blending vessel originates from D. Koller. The published text was written by myself. The necessary infrastructure was provided by the RCPE under the scientific lead of J. Khinast.

O. Scheibelhofer, N. Balak, P. R. Wahl, D. M. Koller, B. J. Glasser, J.G. Khinast; "Monitoring Blending of Pharmaceutical Powders with Multipoint NIR Spectroscopy" In: AAPS PharmSciTech 14.1 (2013), pp. 234–44.

> The experimental work, and consecutive data analysis, was done by myself. Important preliminary work, as the first trial runs with this set-up, were done together with N. Balak. P. Wahl was responsible for some Matlab scripts used in this work. The basic idea and the construction of the blending vessel originates from D. Koller. B. Glasser provided relevant input regarding the behavior and flow pattern of powders. The necessary infrastructure was provided by the RCPE under the scientific lead of J. Khinast.

O. Scheibelhofer, R. Hohl, S. Salar-Behzadi, D. Haack, K. Koch, P. Kerschhaggl, S. Sacher, J. C. Menezes, J. G. Khinast; "Automatic Correction for Window Fouling of NIR Probes in Fluidized Systems" In: Journal of Near Infrared Spectroscopy, Special Issue: Pharmaceutical Applications (2014), (in press).

> The experimental work was done by R. Hohl. The data analysis and the composition of the published text was done by myself. S. Salar-Behzadi provided theoretical input about the fluidized bed process. I want to take the chance and thank D. Haack for providing the material, K. Koch for providing the fluidized bed apparatus and P. Kerschhaggl for providing the spectrometer. The work was done under the supervision of S. Sacher. J. Menezes provided valuable theoretical input about measurement issues with near-infrared probes. The necessary infrastructure was provided by the RCPE under the scientific lead of J. Khinast.

1 Introduction

1.1 Near-Infrared Spectroscopy for Process Monitoring

Near infrared spectroscopy (NIRS) has a wide field of applications, and has gained a lot of attention in the recent years. Hence, an overview of the state-of-art, with focus on the pharmaceutical industry, will be given first.

1.1.1 Process Analytical Technology

In the past, good manufacturing procedures (GMP) and numerous sequential quality checks were introduced to guarantee the safety of products. However, new monitoring and process-control methods are increasingly required by the U.S. Food and Drug Administration (FDA) via the Process Analytical Technology (PAT) initiative [1] and the International Conference on Harmonization of Technical Requirements for Registration of Pharmaceuticals for Human Use (ICH) via the Quality-by-Design (QbD) guidelines [2–4].

The term Process Analytical Technology (PAT) was coined to describe "*a system for designing, analyzing, and controlling manufacturing through timely measurements (i.e., during process) of critical quality and performance attributes of raw and in-process materials and processes, with the goal of ensuring final prodcut quality*" [1]. The aim of these initiatives is to gain deeper insight in pharmaceutical manufacturing processes, replacing empirical approaches by knowledge-based procedures. A detailed understanding of a process, such as powder blending, and its impact on the product quality allows companies to "build in quality" instead of "testing it into the final product".

Simply put, understanding the process allows for timely correction measures, hence enabling quality even with varying raw products. Even more, fault production, leading to material and money waste, should not happen if a process is fully understood.

As such near-infrared spectroscopy is one of the most used analytical tools for PAT. Due to a variety of applications, it has gained a solid foothold in the industry.

1.2 Near Infrared Spectroscopy as PAT-Tool

In the last years, near-infrared (NIR) spectroscopy has become a routinely used tool for process analysis, especially in the pharmaceutical industry. A large amount of literature is available and comprehensive reviews give a good overview on the topic and state of the art [5–15]. Currently, even the majority of PAT applications is based on the utilization of NIR spectroscopy [16].

The following discussions are restricted to spectroscopy on solid materials, powders, granular materials and similar materials and completely neglect the huge field of NIR spectroscopy for, and inside, liquids and gases.

Although spectroscopy on powders and solids, with the aim of process monitoring, started already some decades ago [17], NIR spectroscopy flourished with the appearance of computer power, necessary to perform Fourier transformations, and allow statistical assessment, of a large number of spectra [18].

Because of the amount of variables involved, the high correlation between spectral variables, and the often subtle changes of the spectra, statistics need to be used to evaluate spectra and create models for prediction and interpretation [18]. However, experience and mathematical understanding is needed to avoid common pitfalls [13].

Often enough it is possible to create a good correlation between acquired spectra and the property to be investigated. However, only careful consideration and background knowledge can assure that indeed the correct correlation is modeled. Otherwise, correlations exist with a third (unknown) variable or just spurious correlations are modeled which will lead to failure in prediction over the long term. The proper testing of independent samples can, but must not, expose such issues. Having physical understanding of the effects involved, during sample preparation and presentation, as well as in the actual creation of the spectra, is a key element for building reliable, robust and precise models.

1.2.1 Applications of NIR Spectroscopy in the Pharmaceutical Industries

Due to the high sensitivity of NIR to water, the determination of the progress in drying operations was one of the first applications in the pharmaceutical environment, and is still important today [19, 20].

A second large area, where NIR spectroscopy is applied, is the determination of concentration of pharmaceutically active ingredients. This is especially useful for the characterization of mixtures, and assessing the homogeneity of blends [21–23]. For the analysis of blended granular samples the representativeness is a critical issue, and work was invested connecting the "theory of sampling" and NIR-measurements [24, 25].

As the penetration depth of NIR is very small, just small volumes are sampled during a single measurement. For analytical approaches, integrating spheres can be used, to gain the benefit of a diffusely illuminated and detected sample [26, 27]. For in-process measurements, this is not applicable straightforward; nonetheless nowadays a variety of probes is available, offering different illumination and detection geometries.

During transportation processes via pneumatic pipes or conveyer belts, and during storage, segregation of powders might occur. NIR can detect segregation by the change in spectra, on a pure qualitative basis, and without a provided qualification model. Hence NIR was used to study powder streams inside the dosing units of tablet presses [28].

The next possibility is right after compaction, not on powder anymore, but on solid tablets [29]. The determination of API content in tablets, although a traditional field for laboratory analysis, can be achieved by NIR. Even more, it can be done without destroying any tablets, and not just on drawn samples (off-line), but on all tablets leaving the press (in-line). Depending on the question one wants to ask, the spatial resolution of the obtained spectra can be chosen, either to determine the content uniformity of whole tablets, or to investigate the API distribution across a tablet core [29–33]. Subsequently, in the same manner, the coating of tablets can be analyzed [34, 35]. Even the dissolution behavior, affected by API, density, etc. can be estimated by NIR which can take the role of a soft sensor in this case [36, 37].

The mentioned examples above are just a few of all the ongoing work. With the paradigm shift of the pharmaceutical industry to new, preferably continuous processes, and the strife for real-time-release, also the application of NIR for these processes is coevolving [38, 39].

1.2.2 Regulatory Requirements for NIR in the Pharmaceutical Environment

There are two important documents dealing with the qualification of NIR-spectrometers. One is chapter <1119> in the U.S. Pharmacopeia 29, the other one is the European equivalent, chapter 2.2.40 in the European Pharmacopeia 5.0.

However, the European Medical Agency (EMA) is concurrently drafting a new "Guideline on the use of Near Infrared Spectroscopy (NIRS) by the pharmaceutical industry and the data requirements for new submissions and variations".

1.2.3 Trends in NIR

It is impossible to give a detailed overview of all the recent work and trends to come, regarding the development and future of near infrared spectroscopy. However, some examples shall be mentioned that might become important, or even predominant in the next years.

A first issue is the availability of robust, small and handheld NIR spectrometers. This actually is a corollary of in-situ field studies in the agricultural area, e.g. the determination of fruit maturity, while those are still growing. However, the ubiquitous availability of mobile and handheld NIR instruments, will lead to their prevalence in the pharmaceutical environment, and produce large spectral libraries, e.g. enabling the complete scanning of raw products and more.

Recent efforts of distinguishing between scattering and absorption of near-infrared spectra must be mentioned. This offers the huge advantage that physical and chemical information of measured samples can be distinguished, which is just approximately done until now by various spectral pretreatments. Different possibilities to do this exist. Here the usage of different simultaneous illumination and detection set-ups have to be mentioned [40, 41], but also photon time of flight resolved spectroscopy [42].

Near infrared spectroscopy is already dominating process analytical technology. New advancements, ranging from technical aspects as new probe designs, up to new possibilities of spectral interpretation via diverse mathematical methods, will also henceforth strengthen the utilization of near-infrared spectroscopy. Currently the jump from idealistic lab-scale processes to more harsh environments of manufacturing plants is going on. Herein, near-infrared spectroscopy is one of many applied sensors, and the combination of NIR with traditional sensor data will show for sure some synergies.

For many processes simply taking a sample is not enough, but regular sampling at different places and at different times is necessary to develop process understanding and to enable control loops. Again spectroscopy offers a swift method for supervision of processes and in combination with multivariate data analysis methods the power to make decisions within seconds.

1.3 The Application of Hyperspectral Imaging

Chemical imaging (also termed hyperspectral imaging), i.e. spatially resolved spectral images (like displayed in Figure 1.1), has to be mentioned in this context [43]. This computer-power demanding field has grown in the recent years, and a variety of applications has emerged. The ability to localize chemical components, or show distributions of chemical species has initiated interest in the pharmaceutical, agricultural and food processing industry [44, 45].

Hyperspectral imaging (HSI) is a development, combining the advantages of machine vision and spectroscopy. Whereas spectroscopy exhibits chemical information, composition and pollution of materials; machine vision gives information about spatial distribution, texture, and shape [45–47].

HSI in the NIR region is already used for process and quality monitoring in the pharmaceutical industry [43], for example for determining API distributions in tablets [35], as well as in the food processing industry [47], e. g. for determining meat quality [45], classifying fruits [48], and further in the waste management industry for sorting plastics [49].

Examples of this method in the pharmaceutical industry are the supervision of the goodness of powder blends [50, 51], the distribution of the active pharmaceutical ingredient (API) in tablets [52] and identity control. As a special ability, the availability of a spectrum for every spatial pixel allows dynamically changing the sample size by summing up several pixels [50, 51, 53, 54].

However, in the pharmaceutical industry problems arise, because a large enough looking window or the open presentation of samples is often not possible due to safety and hygiene considerations.

1.4 The Application of Multipoint Near-Infrared Spectroscopy

An emerging field is the utilization of multiprobe systems. On the one hand, this is very cost efficient, on the other hand, it allows the investigation of several positions inside a process, or consecutive processes, without having to deal with the problematic calibration transfer [55–57].

For simultaneous sampling with near-infrared spectroscopy (NIRS) different strategies are possible:

- The contemporaneous operation of several spectrometers. This has the disadvantage of high costs and the problematic comparison between different spectrometers.
- The use of a traditional spectrometer and an optical switch to access several probes consecutively. This has the disadvantage of signal intensity loss due to the switch and idle time during the switch operation. A successful instrument with this set-up is the Matrix-F by Bruker. A similar setup was used for several experiments in this work, and will be described in more detail in section 5.4.2.
- Sampling at several, although adjacent, positions, is done by the already mentioned imaging systems. A huge advantage of such systems is the high throughput.

It is therefore beneficial to combine push-broom based systems with traditional spectroscopic probing. This offers the following advantages:

- Synchronous measurements at multiple positions;
- Fast spectral acquisition;
- Versatile probes to fit the required process that can be docked into the system due to standardized SMA 905 ports;
- Continuous self surveillance or simultaneous measured standards;

Such a combined device was used and will be introduced in section 3.1 in more detail. Comparable systems to the one presented in here, are:

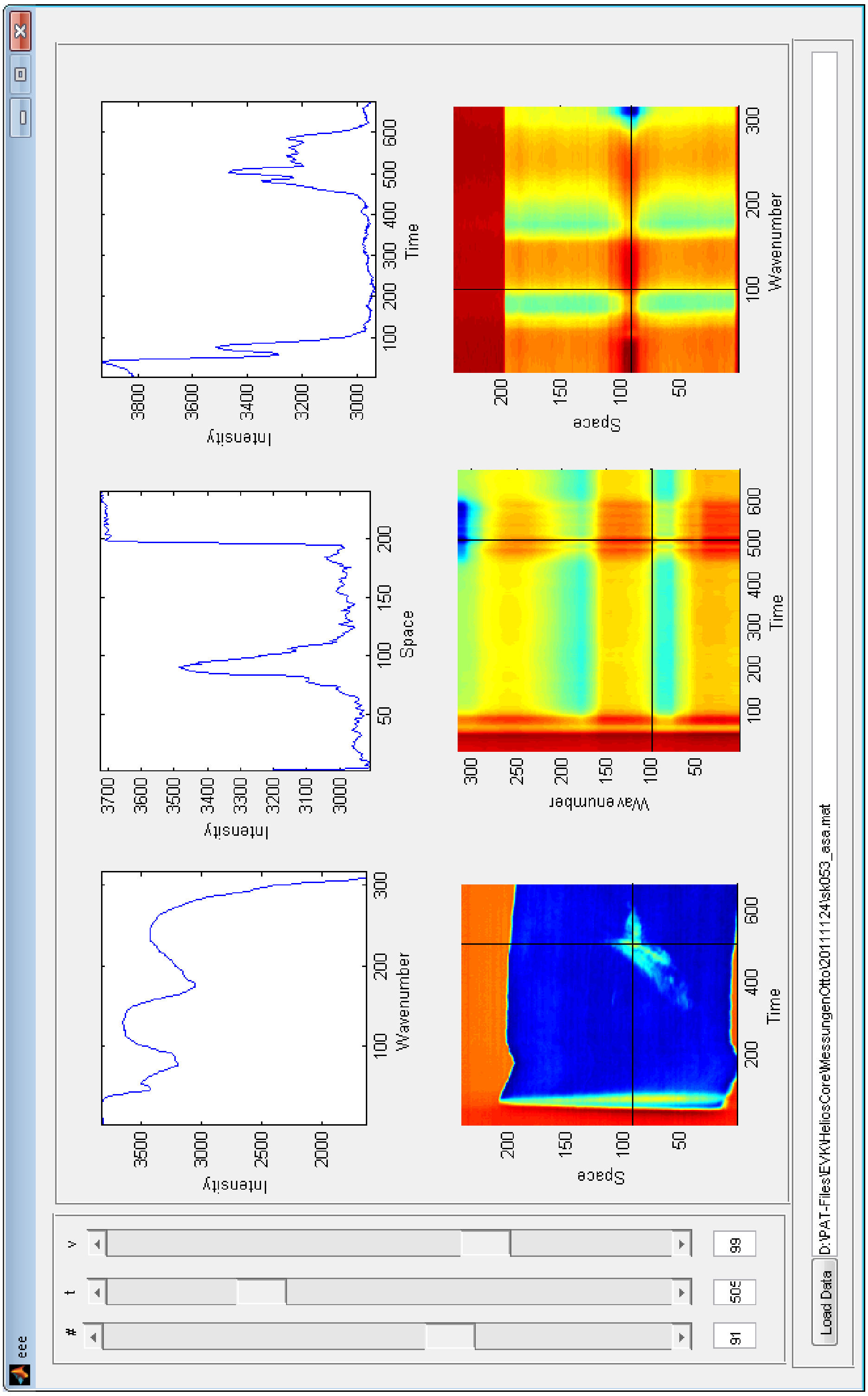

91

t 505

v 99

D:\PAT-Files\EVK\HeliosCore\MessungenOtto\20111124\sk053_asa.mat

Figure 1.1: An example for chemical imaging. The obtained data forms a hypercube with the axis of space, time, wavelength and intensity. Hence several different possibilities to visualize the data are possible, as depicted here. The subject investigated was a cellulose sheet, with a heap of acetylic salicylic acid powder on it. The upper-left image shows the intensity for several wavelengths (labeled wavenumber, although just the pixel number is shown), at the intersection of the black lines at the bottom image (hence at space pixel 91, and timestep 505), etc.

- Bruker offers for their CCD-based camera SureSpectrum adapters to connect optical fibers with SMA-ports to their system. They offer attachments with 1 up to 19 fibers for the VIS and NIR spectral region.
- Specim offers for their NIR-Camera and SWIR-Camera optical attachments, to focus 4 up to 110 fibers on their camera chip. The system was extensively evaluated by the VTT Technical Research Centre of Finland [58].

Without regarding their kind of technical realization some applications of multi-probe systems shall be mentioned:

- Monitoring of a powder blending process [59].
- Monitoring of a fluidized bed process; A multiplexer allows the simultaneous measurement of on-line and off-line samples [60].
- Identity control of tablets. Tablets were mapped on a spectrometer via an optical fiber. The fiber itself was aimed at interesting positions by use of mirror optics. [30].
- The supervision of a dissolution test with six optical probes, coupled via a multiplexer with a spectrometer. The probes differed in their optical pathlength, therefore it was possible to monitor a larger concentration range [61].
- The supervision of several bio-reactors at the same time, again with an optical multiplexer [57].

1.5 Controlled Blending Processes via NIR

Blending processes are key steps in pharmaceutical manufacturing as guaranteeing blend uniformity is crucial to ensure low dosage variability and high product quality.

Clearly, the content of the active pharmaceutical ingredients (API) in the final solid dosage form is particularly important. Tablets out of specifications lead to expensive rework or even recalls, and even more important, dosage forms not compliant with the therapeutic window may cause harm to patients. Another crucial feature affected by powder homogeneity is downstream processability (i.e., compaction of tablets may lead to problems, if certain components are distributed unevenly, e.g., during lubrication with magnesium stearate) [62, 63].

Thus, methods to monitor the various processing steps, especially focusing on blending uniformity, agglomeration and segregation, are critical for maintaining high product quality and eliminating the risk of producing out-of-specification products.

Despite numerous studies, the outcome of a blending process is hard to predict, since it involves the highly complex interactions of many billions of individual particles, each one with its own size, shape, surface characteristics and other properties. In short, blending often depends on a variety of parameters [23, 64–67], including

- operating conditions (fill level, loading order, blending time, etc.)
- material properties (particle size and shape, cohesivity, tendencies for segregation or agglomeration, etc.)
- environmental conditions (humidity, temperature, etc.)
- equipment (blender type, shear rate, etc.)

Moreover, the dynamics of blending processes have been studied theoretically [68, 69] and experimentally. This was done using model substances [70] and pharmaceutically relevant powders [23]. However, using a single probe at a fixed position usually does not provide a reliable assessment of the blending process [21, 71]. In order to fully control and understand the process, temporally and spatially resolved monitoring of blending processes is required.

Traditionally, manual thief sampling is performed to test blend uniformity, with samples taken from different positions in the blender, as prescribed by standard operational procedures. However, sampling may be a source of disturbance for the powder bed, and may bias the results. What is more, to satisfy the requirements of statistics a lot of samples need to be taken [72, 73].

In contrast, NIR probes make non-destructive and continuous monitoring possible. This is a very active field of research [21, 74, 75].

Many pharmaceutical processes are relatively easily accessible using NIR in combination with fiber optics [76–78]. They can be monitored without changing the process setup and barely require manual effort [5, 8].

For example, the monitoring of a components’ concentration on a quantitative basis during blending has been successfully performed [79–81]. Overcoming the problems associated with differences between calibration and measurement has been discussed in the literature [71]. Various aspects of the monitoring of powder blending processes have been addressed in the literature, e.g., problems arising specifically when dealing with powders [82], the determination of a blending end-point [22] and in-line monitoring of a blending process [80].

Furthermore, blending performance parameters, such as homogeneity, depend on the sample size [73]. Some publications describe the use of multiple positions for assessing the blending process and the different strategies to achieve multiple sampling positions. For example, the axis and the side of a bin blender have been investigated using two spectrometers [83]. Different blending kinetics in those two positions have been reported; therefore, NIR monitoring in more than one position has strongly been recommended. El-Hagrasy et al. introduced a V-blender with a set of windows [21]. The blending process was halted, and a NIR fiber-optical probe was positioned against each window for multipoint monitoring.

In the optimized case, to compare different positions, the same probe and spectrometer should be used in different positions without stopping the blending process, as will be presented in this work. Interruptions may change the observed effects and are not feasible in an industrial environment.

Chemical imaging is another method of obtaining more than one sample position. It has been described in the literature [21] and adapted to analyze the distribution of blend components [51, 84].

2 Theoretical Background

2.1 Near-Infrared Light and Matter Interaction

2.1.1 Properties of Light

Electromagnetic radiation can be described, either as waves, or as particles. Which description is chosen depends on the effect one wants to investigate. Basically, the wave-nature of light is essential to describe interference, whereas light-matter interactions are more conveniently described with the particle model.

Hence a photon can be described by the equation series

$$E = \hbar\omega = hf = \frac{hc}{\lambda} = \hbar c\frac{2\pi}{\lambda} = \hbar ck = pc, \tag{2.1}$$

wherein E describes the energy, and p the momentum contained by a photon. The wavelength λ, and the frequency f, respectively the angular frequency ω, are interrelated by the constant speed of light $c = 299792458\,\mathrm{m/s}$. Finally, $k = \frac{2\pi}{\lambda}$ is the so called wavevector.

Hence, a spectrum spanning a certain range of wavelengths, is at the same time a description for a certain energy range. Wavelengths and wavenumbers ν, which are the inverse wavelength, given in cm^{-1}, are equally often used to describe spectra in the near-infrared region. Figure 2.1 gives a comparison of both and the corresponding energy range. The near infrared region spans the wavelengths 770-2500 nm.

2.1.2 Interaction of Light and Matter

When light is passing through a media, its intensity will be attenuated. This is due to reflection, diffraction, scattering, and absorption. The overall attenuation

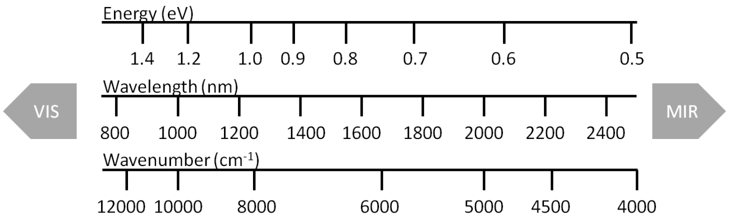

Figure 2.1: Comparison of energy, wavelength and wavenumber for the near-infrared range. For shorter wavelengths the visible region (VIS) borders, whereas for longer wavelengths the mid-infrared (MIR) region commences.

is called extinction [85], and is described by

$$\kappa = \alpha + \sigma \tag{2.2}$$

with κ denoting the extinction, α the absorption and σ the scattering part. It is also possible to describe scattering and absorption by the probability that a photon scatters μ_s or absorbs μ_a inside a media, i.e. the inverse of the free path length [9].

The basis of near-infrared spectroscopy is the analysis of light which has interacted with a sample, thus both parts are important here.

2.1.3 Absorption

A photon can interact with matter; it can be annihilated and the energy is transformed into an excited state (e.g. electron excitation, vibrational excitation or rotational excitation).

Whereas visible light is in the range of electron excitations, near-infrared mostly covers the range of molecular vibrations [11]. It is therefore helpful to recapitulate the vibrational modes of molecules.

A simple approximation of a (diatomic) molecule is the quantum-mechanical harmonic oscillator. The energy levels in the quantum-mechanically described oscillator are quantified, and can be described by

$$E_v = hf\left(v + \frac{1}{2}\right) \tag{2.3}$$

with h being Planck's constant, v the vibrational quantum number and f the vibrational frequency. However, real molecules do not exhibit a quadratic potential, but a more complex behavior. A common approximation is the Morse-potential which reflects the following attributes:

- At the dissociation energy, the molecule is destroyed. Hence, when more energy is put into the molecule it dissolves.
- Energy levels are closer to each other, when approaching the dissociation energy.

The energy levels can then be described with

$$E_v = hf_v\left(\left(v+\frac{1}{2}\right)+\chi\left(v+\frac{1}{2}\right)^2\right) \tag{2.4}$$

where f_v is the fundamental frequency and v is the vibrational quantum number (0,1,2,...); χ describes the anharmonicity.

A transition is only IR-active, if the dipole moment can be modulated by the vibration, hence

$$\frac{\partial\mu}{\partial q} \neq 0, \tag{2.5}$$

with μ being the dipole moment and q the vibrational coordinate.

For the strictly harmonic oscillator only transitions with $\Delta v \pm 1$ would be allowed, interacting with a photon of the energy

$$\Delta E = E_{v+1} - E_v = hf. \tag{2.6}$$

However for the anharmonic oscillator this rule is relaxed, and overtones ($|\Delta v| > 1$) are allowed. Due to anharmonicity however, the frequency of an overtone is not a plain multiple of the fundamental frequency, but less. The observed frequencies for a transition from $v = i$ to $v = j$; $n = j - i$ can be approximated by

$$f_{i,j} = \frac{f_i n - f_i \chi n(n-1)}{1-2\chi}. \tag{2.7}$$

For polyatomic molecules, transitions involving two vibrational modes ($\Delta v_m = 1$, $\Delta v_n = 1, \ldots$), so called combination bands, are possible [11].

Overtones and combinations as found in the NIR region are not as probable as fundamental transitions, and hence absorption is less intense than in the mid-infrared region. Furthermore, they have a broader peak profile than the corresponding fundamental peaks.

The most probable, and hence intense, overtones are found in the most extreme anharmonic molecules. Hence functional groups including hydrogen, as e.g. C–H, N–H, and O–H are the most intense features found in NIR-spectra [86]. In combination with these, combination bands with C–C and C–O can be found.

Summed up, functional groups are prominent in near-infrared spectra and can lead to fingerprint spectra, enabling to perform a chemical classification of the samples analyzed, although the direct assigning of peaks and bonds is often very complicated in the NIR-region, as peaks are broad and overlapping [87].

2.1.4 Scattering

A photon can interact with matter, in a way that its direction changes, but the contained energy is still conserved. For describing scattering the wave picture is more suitable than the particle picture. A simple effect of scattering on powder is illustrated in Figure 2.2.

Figure 2.2: Different amounts of acetylic salicylic acid crystals. Isolated crystals, as on the left hand side, are mostly transparent, and show a glossy behavior. In contrast, a legion of crystals, as on the right hand side, has a lot of scattering possibilities, and hence looks uniform and white in all directions.

Light Scattering on A Single Particle

The scattering on single particles is described by the Mie-equations which are basically an exact solution of the Maxwell equations for the case of a sphere with a certain diffraction index. Although it holds for all size of spheres, it is just valid for isolated spheres [85].

Some of the consequences of the Mie-theory are [88]

- For small particles (compared to the wavelength of light), the forward scattered part is equal to the backscattered part which is described by Rayleigh scattering.
- For large particles, the forward scattered amount is much larger.

Hence, the relative sizes of wavelength λ and encountered sphere are important. In the Mie regime the wavelength dependence of scattering, described by the scattering coefficient μ_s, can be assumed to be of the form

$$\mu_s \propto a\lambda^{-b} \tag{2.8}$$

with a and b being constants. When being scattered, the probability for scattering directions, described by the deflection angle θ (and isotropic for the azimuthal angle ψ), are often approximated by the Henyey-Greenstein phase function

$$p(\cos(\theta)) = \frac{1-g^2}{2(1+g^2-2g\cos(\theta))^{\frac{3}{2}}} \tag{2.9}$$

with the anisotropy factor g. A value of $g = 0$ describes isotropic scattering, whereas $g = 1$ means totally forward scattering and $g = -1$ total backwards scattering.

For larger particles, the light entering the sphere is absorbed. Further, for a bulk of particles observed with NIR, scattering happens multiple times. This leads again to an isotropic behavior in scattering for the whole sample [9] as shown in Figure 2.2. Hence a theory describing densely packed particles is of advantage.

2.1.5 Description of Diffuse Reflection

Diffuse reflection appears if light penetrates into a powdered sample and reemerges from the surface [17]. Effects of diffraction, refraction, absorption, elastic and inelastic scattering are taking part in this process. Hence interfaces in a sample play an important role. This is put to the extreme, for powder samples which consists of small fragments, often with irregular surface, in contact with each other, but also separated by (air-filled) voids.

The fractions of transmitted light $T = \frac{I_T}{I_0}$, reflected light $R = \frac{I_R}{I_0}$ and absorbed light A has to sum up again

$$A(d) + T(d) + R(d) = 1. \tag{2.10}$$

The individual fractions however, are dependent on the sample thickness d.

A well known equation describing the diffuse reflection is the Kubelka-Munk function

$$F = \frac{(1 - R_\infty)^2}{2R_\infty} = \frac{K}{S} \propto \frac{\alpha}{\sigma} \tag{2.11}$$

which relates the measured reflected light for an infinitely thick sample R_∞, to the ratio of scattering and absorption. The obtained absorption coefficient K and scattering coefficient S however are "apparent" and only proportional to the fraction $\frac{\alpha}{\sigma}$ describing scattering and absorption on the particle level. Moreover, as K is proportional to the volume, but S proportional to the surface, the approximate relationship $F \propto c$ is often used for the determination of concentration levels c.

In practice the condition of an "infinitely thick" sample can already be achieved with a powder layer of several millimeter thickness, where practically no transmission occurs anymore. The second condition is the complete diffuse illumination and detection of light which can be achieved with Ulbricht spheres [9, 41, 89].

2.1.6 Modes of Measurements

A sample is directly illuminated if the incoming light is coming from just one defined direction. There are now several possibilities how light that has interacted (i.e. scattered at) with the sample, can be collected again [9].

- *Transmission*: The light is collected on the opposite side of the sample.
- *Reflection*: The light is collected on the same side than the light source is.
    - *Specular reflection*: The angle of incidence is the angle of detection.
    - *Diffuse reflection*: At all other angles, light is called diffusely reflected.

For samples not glossy, the diffuse reflection is of higher intensity than the specular reflection. Hence spectroscopy on these samples is called "Diffuse Reflection Spectroscopy" [9]. Examples of photon behavior, in a scattering medium, are seen in Figures[1] 2.3 and 2.4.

---

[1] These images were created during the university course "Biooptics" at the Technical University Graz.

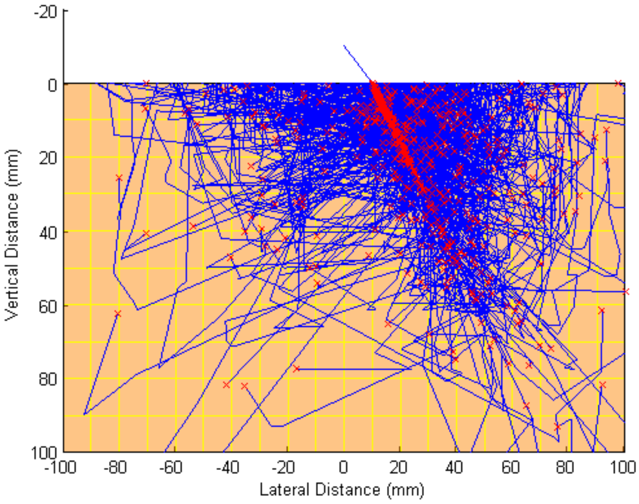

Figure 2.3: Monte-Carlo Simulation for photons in a media with $g = 0.7$, $\mu_a = 0.1\,\mathrm{cm}^{-1}$, $\mu_s = 0.5\,\mathrm{cm}^{-1}$. The positions of absorption are marked with a red x. Although the entry point and direction of the ray are always the same, due to scattering, photon paths are divergent.

For powders, especially reflection at the interfaces between particles and air lead to the isotropic distribution of light. This causes the perception of powders as white, the same effect can be observed with snow. Only very strong absorption can overcome this effect in the visible range, leading to absorption already at the surface, and hence suppressing other effects. Then powders can be colored, as is observed for some metal powders, coal powders, etc. In the near-infrared region, scattering effects are much smaller, and hence absorption can be used for analytical purposes. Nonetheless, the mentioned effects lead to a background intensity across all wavelengths [90, 91].

2.2 Near-Infrared-Spectroscopy

2.2.1 Spectrometer Instrumentation

Naturally, for the detection of NIR spectra, one needs a light source in the respective wavelength region (usually a tungsten-lamp) and a detector (usually a

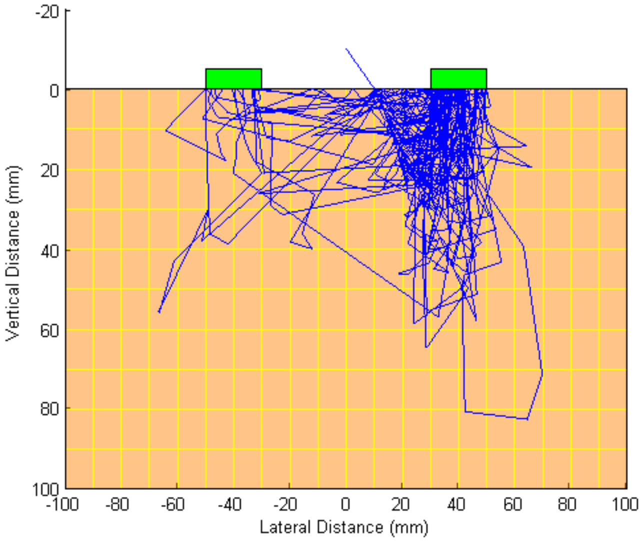

Figure 2.4: Monte-Carlo Simulation for photons in a media with $g = 0.7$, $\mu_a = 0.1\,\mathrm{cm}^{-1}$, $\mu_s = 0.5\,\mathrm{cm}^{-1}$. Just photons which reach the detector (green) are shown. Evidently, the shape of the sampled volume is not described easily.

semiconductor device). The most crucial part, however, is to separate different wavelengths. Hence, two principle set-ups can be imagined. Either a dispersive element is put into the beam path, and detection already happens at different wavelengths, or the beam is sent through an interferometer, and the signal for different wavelengths is obtained by Fourier-transformation.

Fourier-Transformation Based Spectrometers

The beam is sent through an interferometer device, and the interfered signal is collected at a detector. By changing the pathlength of different beam arms, the interference pattern is changed. Hence, by Fourier-transformation, it is possible to obtain the intensity for every wavelength separately.

The advantage of Fourier based spectrometers is the very good signal-to-noise ratio, and high wavelength resolution. However, as moving mechanical elements are involved, those spectrometers are rather slow, and sensitive to harsh conditions (i.e. vibrations in the surroundings). As such, FT-spectrometers are usually used in laboratories, although certain types with a robust interferometer are suited for plant environments [92].

Spectrometers with Dispersive Elements

In such devices, dispersive elements are used to define at which wavelength is measured. Such dispersive elements can be prisms and gratings, or a combination of both, as well as interference based devices again, such as acoustical-optical tunable filters.

The advantage of such devices is their robustness against environmental disturbances, and their high-speed which makes them suitable for a production environment. However, they do not reach the same wavelength resolution and signal-to-noise ratio, as their FT-counterparts.

Imaging Methods

Methods for gaining spectral images are divided into three different classes, according to the number of dimensions monitored at a time step [45].

- *Whisker-Broom* systems are working like traditional spectrometers. They create an image by rastering an area. They produce high quality spectra at the cost of low speed.
- *Push-Broom* systems project a spatial line through a dispersing element on a detecting chip. Hence, on the chip one dimension is used for the spatial, the other for the wavelength separation. Such systems can be very fast, as no moving mechanical element is involved. Images can be created, when a sample is moving perpendicular to the detection line.
- *Staring-Imager* systems indeed map a 2-dimensional area, however only at one wavelength at a time, e.g. with the use of a filter wheel. Therefore, those systems can be extremely fast, but the number of different wavelengths is limited.

A push broom system is available from EVK and applied for the quality control of paper [93], blueberries, potatoes and for waste management [49]. It was used in this work for pharmaceutical purposes, as will be described in section 5.3.

2.2.2 Near-Infrared Probes

Concerning the measurement of granular material, it has to be considered that

- NIR radiation has a very low penetration depth into powder. Hence to sample a representative amount, a rather large area has to be illuminated and detected.
- Measurements of powder is based on diffuse reflection. Hence, the occurrence of specular reflections should be minimized. Possibilities are the use of optical diffusers or polarization filters, an arbitrary angle between illumination and detection, and preferably several illumination and detection spots.
- When measuring cohesive powders, it is very likely that window fouling occurs. To avoid this the probe can be positioned remotely to the samples, however this limits the detected volume to the surface of a passing material stream. If the probe should be immersed into the powder bed, it can either be cleaned by the good itself, if abrasive enough, or a cleaning mechanism, e.g. a rotary valve, should be installed.

An example for a probe with several illumination fibers, the Hellma NIR diffuse reflectance probe (Hellma Analytics, Müllheim, Germany), is shown in Figure 2.5.

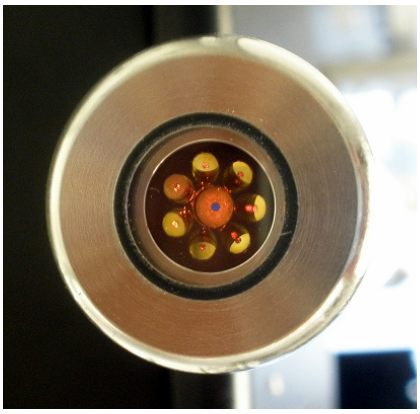

Figure 2.5: Picture of the probe head of the Hellma NIR diffuse reflectance probe. The detection fiber in the center is surrounded by tilted illumination fibers.

2.2.3 Quantitative Spectral Interpretation

Since the light source, and all optical elements in the beam path have their own characteristics, a reference spectrum is needed to cancel out those influences always.

For transmission mode, the reference spectra are usually recorded without any sample in the beam path, or with an empty cuvette, etc. In diffuse reflection mode, a highly reflective standard material is used. The material should be diffuse reflective, and have the same reflectivity over the concerned wavelength region. Most commonly used is Spectralon® (Labsphere, North Sutton, United States), which is a derivative of Teflon. However, this exhibits the problem that the geometry (especially the distance of the reference material to the probe) has a strong influence on the spectra. Therefore, when the geometry is changed, spectra are usually not directly comparable on an absolute scale.

Besides the identification of peaks which, if possible, can give information about the chemical composition of a sample, quantification of materials is of interest. This is based on the Beer-Lambert law

$$A = -\log\left(\frac{I}{I_0}\right) = \sum_i \varepsilon_i c_i d \tag{2.12}$$

hence the Absorbance A is the sum of the absorbance for every material i, which can be calculated as the product of the specific absorption ε_i times the concentration c_i and the sample thickness d. At the same time this is the negative decade logarithm of the fraction of the gained intensity I to the reference intensity I_0. Furthermore this is true for every wavelength independently, but $\varepsilon_i(\lambda)$ is wavelength dependent [9].

However, the Beer-Lambert law is strictly true for transmittance and total reflectance spectra only. Also, scattering is neglected. Therefore, for diffuse reflectance measurements (which are based on scattering, otherwise no light would be detected) the Beer-Lambert law is actually not true. However, from a practical point of view, the proportionality is often still retained over small concentration changes, and hence the law is widely used, even for the interpretation of diffuse scattering spectra [9].

Nonetheless, different effects have to be included in the spectral interpretation, e.g. non-linearity of spectral absorbance, matrix effects, changing penetration depths, and so on. Prominent are difficult scattering characteristics, and hence different spectra, due to changing physical sample attributes, like particle size and shape [94]. Hence, multivariate data analysis can be a useful tool for interpreting spectra, especially as one has to deal with a large number of different wavelengths, and a large number of spectra, at the same time.

2.3 Multivariate Data Analysis for The Interpretation of Spectra

When dealing with a large amount of spectra, each consisting of a large number of wavelengths, it is not feasible to just use the intensity at a single wavelength, as this would lead to an unnecessary loss of information. Hence multivariate data analysis is used, and will be presented in the next chapter.

2.3.1 Spectral Transformations

First of all, one seeks to have the spectra in a way that the spectral pattern is proportional to the investigated concentration. So the measured spectrum, reflection and transmission spectra, are converted to absorbance spectra, as in equation 2.12, or via the Kubelka-Munk function, as in equation 2.11 [95]. This does not eradicate all other (unwanted) influences on the spectra, besides the change in concentration, though. Hence spectral transformations are commonly used to eradicate physical influences on the spectra, and promote chemical ones.

Different transformations are discussed in the following. Which transformation to chose is often an important question, and is strongly dependent on the experimental set-up and the sample investigated. Assuming N spectra, where every spectrum, consists of M different wavelengths. Hence, $a_{\lambda,i}$ denotes the absorbance at wavelength λ of spectrum i. Some raw spectra, with different concentrations of citric acid, lactose monohydrate and cellulose, are displayed in Figure 2.6. Looking at the spectra, it becomes clear that just taking the intensity of a certain peak, would not lead to a correct estimation of the concentration, because of the baseline shift.

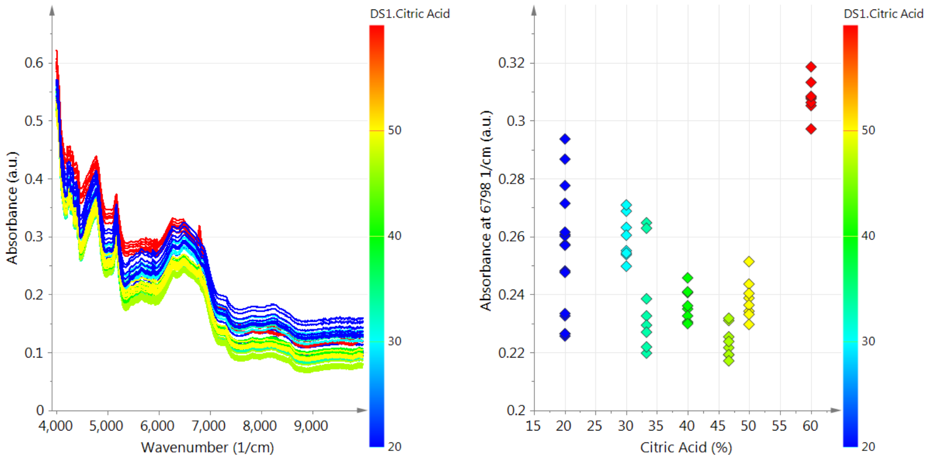

Figure 2.6: Left: Raw spectra, with different concentrations of citric acid. Right: Absorbance at $6798\,cm^{-1}$, where citric acid has a prominent spectral feature. On the raw spectra, the correlation between spectral peak height and concentration is not evident.

Baseline Subtraction

Differences in baseline are often caused by different particle sizes, leading to a different scattering behavior. [86] Also the distance of the probe to the sample, and hence the possibility of light escaping the sampling volume undetected, leads to an increase of "pseudoabsorbance" over all wavelengths.

There are different possibilities to remove the baseline

- The minimum value, or the mean of the whole spectrum, is removed.
- A polynomial is fit through the spectrum and removed.
- A spectral region, where no change should occur is chosen. A fit through this region then determines a reference baseline which is removed from the whole spectrum.

Standard Normal Variate (SNV)

This method is used to normalize the spectra, if the peak intensities changed, because the amount of absorbing material in front of the probe, or its density has changed.

This is done by subtracting the mean of a spectrum $\boldsymbol{a}_i$, and dividing by its standard deviation, as according to [95]

$$\boldsymbol{a}_{i,SNV} = \frac{\boldsymbol{a}_i - \bar{a}_i}{\sigma_{a_i}}, \tag{2.13}$$

where $\bar{a}_i$ denotes the mean over all wavelengths of spectrum $\boldsymbol{a}_i$ and σ_{a_i} the standard deviation over all wavelengths of spectrum $\boldsymbol{a}_i$.

The SNV-transformed spectra are shown Figure 2.7. Now, as indicated by the coloring, certain spectral regions are aligned according to the concentration change.

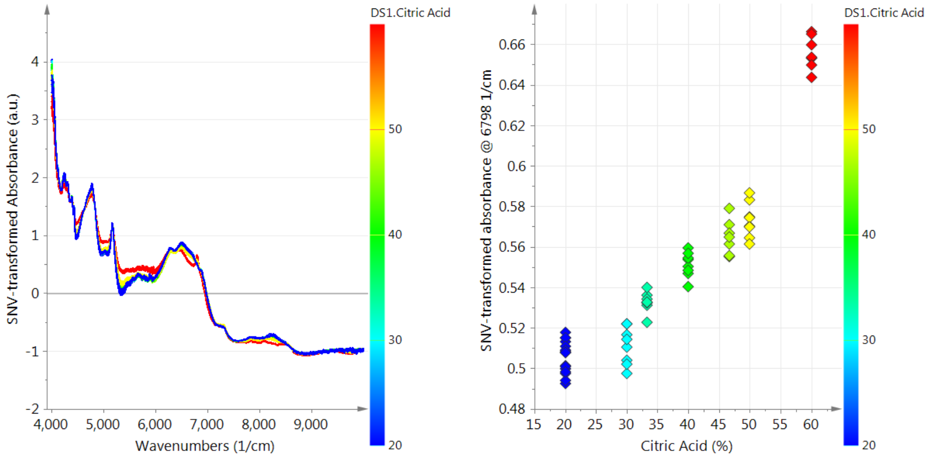

Figure 2.7: SNV-transformed spectra with different levels of citric acid. The absorbance at 6798 cm^{-1} now reflects the concentration, although the relationship is not completely linear.

Smoothing

Different smoothing algorithms can be used on spectral data.

- Low pass filtering. This reduces the noise level, but at the same time leads to a broadening of spectral features.
- Spline fitting share the same effects.
- A Moving Median Filter is insensitive to single outliers, e.g. spikes in the spectra caused by fault pixels of a CCD-detector. However, this method leads to steps in the spectra.

- Savitzky-Golay Smoothing is a type of Wiener-filter, and will be discussed separately.

Savitzky Golay Smoothing and Derivative

The basic principle of Savitzky-Golay Filtering is to fit a moving window, containing f data points of with a polynomial of order p. By changing the filter coefficients, also derivatives of a discrete number series can be gained [96]. To a number of $\frac{f-1}{2}$ points at the beginning and at the end of the series, the method can not be applied, and thus those are neglected further.

Hence for SG-smoothing and derivative certain parameters, namely the size of the moving window f and the degree of the polynomial p change the outcome. By using the first derivative, constant baseline offsets are removed intrinsically.

An example for smoothed spectra and derivates of spectra are shown in Figures 2.8 and 2.9. In the 1^{st} derivative, a former peak maximum is now placed at the zero-crossing, hence the information of the peak shape is found in the adjoint wavelengths.

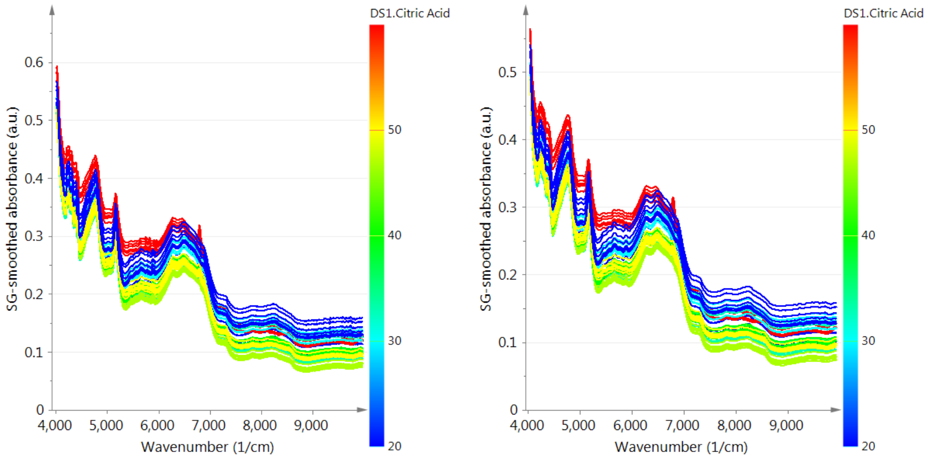

Figure 2.8: Spectra smoothed with different Savitzky-Golay kernels; Left: quadratic, 15pt, Right: quadratic, 45pt

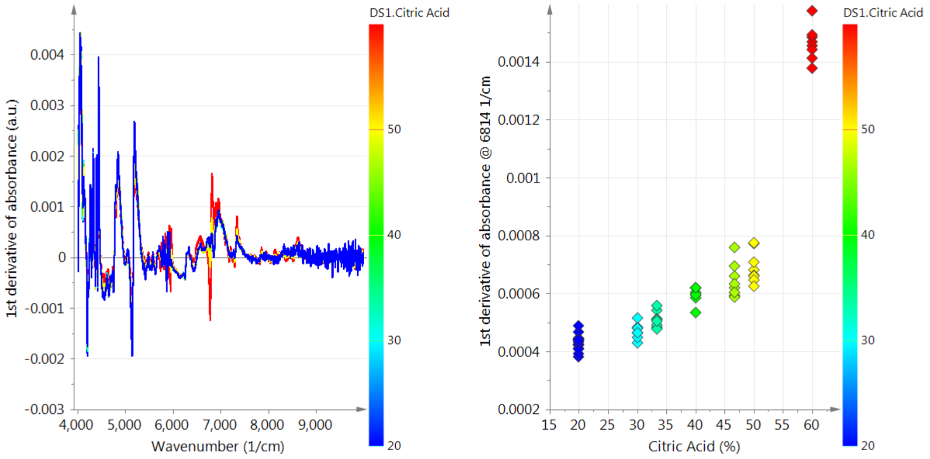

Figure 2.9: 1^{st} derivative of spectra with Savitzky-Golay (quadratic, 15pt). The derived absorbance at 6814 cm^{-1} shows a correlation to the content of citric acid, but the data points are scattered widely.

Multiplicative Scatter Correction

This method is also known as Multiplicative Signal Correction. Diffuse reflectance spectra often show differences due to different scatter effects, caused by different pathlengths of the scatter photons, often caused by different particle sizes [95].

The motivation for this method is that small effects, and hence deviations of the "usual" spectra, are linear. Hence a mean spectra $\bar{\boldsymbol{a}}$, of all the i available spectra $\boldsymbol{a}_i$, eg. during a process, is created. Each spectra is then fit to the mean spectra using least-squares regression, [97]

$$\boldsymbol{a}_i = \alpha_i + \beta_i \bar{\boldsymbol{a}} + \boldsymbol{e}_i \tag{2.14}$$

and the gained coefficients α_n, β_n are used to create the MSC-corrected spectra

$$a_{\lambda,i,\text{MSC}} = \frac{a_{\lambda,i} - \alpha_i}{\beta_i}. \tag{2.15}$$

Transformed spectra are shown in Figure 2.10.

Extended Multiplicative Scatter Correction (EMSC) includes further terms into these calculations. Reference spectra $\boldsymbol{a}_{\text{ref}}$ typical for the process (e.g. spectra of

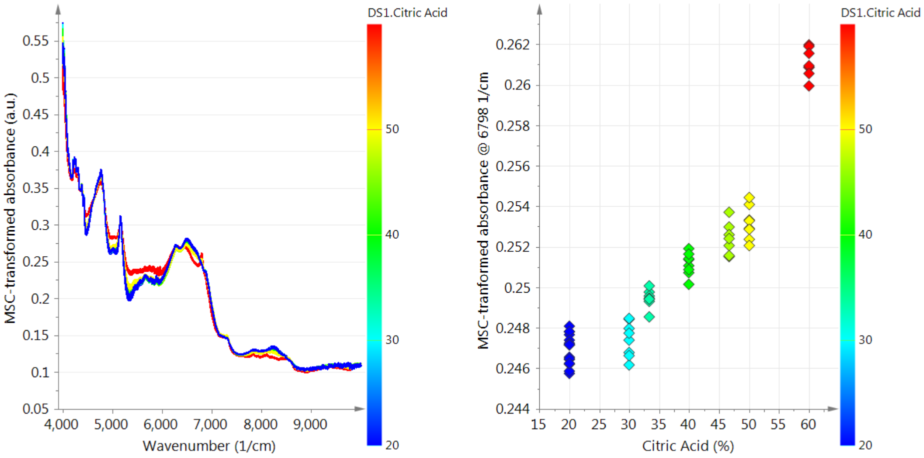

Figure 2.10: MSC transformed spectra, and the intensity at a wavenumber representative for the citric acid level. In the present case MSC transformation leads to a good correlation between spectra and citric acid content.

pure components, or the difference of spectra from start and end of a process) can be included. Furthermore, wavelength dependent effects are included by a term $\boldsymbol{\lambda}$ linear with wavlength, and $\boldsymbol{\lambda}^2$ quadratic with wavelength [98].

The formula to be regressed then looks like

$$\boldsymbol{a}_{i,\mathrm{EMSC}} = \alpha_i + \beta_i \bar{\boldsymbol{a}} + h\boldsymbol{a}_{ref} + \delta_i \boldsymbol{\lambda} + \varepsilon_i \boldsymbol{\lambda}^2. \tag{2.16}$$

Either the corrected spectra, as well as the coefficients can contain valuable information.

Further notes

It is common to use several pretreatments consecutively, then the order is of importance. Apart from MSC, where the whole dataset is used, the spectral transformations are individual to every spectra, hence the addition or exclusion of spectra into the dataset does not change already transformed spectra.

What must be considered additionally is to chose a proper wavelength region. On the one hand, having a broader region is beneficial, as the noise measured at a single wavelength cannot contribute that much to the final interpretation. On the other hand, if spectral regions are included, where noise is dominating the signal, the interpretation will become worse.

2.3.2 Variable Scaling

In the following the mostly used chemometric tools, i.e. principal component analysis (PCA) and projection to latent space (PLS), (also termed partial least squares regression) will be explained. The terminology of spectroscopy will be used, although multivariate data analysis is of course much more diverse and can be used to practically any area (where more than one variable occurs).

Assuming a number of N collected spectra, consisting of M different wavelengths; in the notation of multivariate data analysis (MVDA), one speaks of N observations and M variables. Hence x_{ij} is variable j of observation i, or at the same time absorbance at wavelength λ_j of spectrum i [95].

Variables undergoing multivariate data analysis are usually scaled. This is especially useful, if variables have to be compared that do not have the same source and hence different units and scale range (e.g. temperature in K and pressure in $mbar$).

For spectra however, different absorbances for different wavelengths are related, and their absolute values can be compared. Hence, often just mean-centering is applied. Scaling can be described the following way [95]

$$x_{ij,\text{scaled}} = \frac{x_{ij} - \overline{x}_j}{w_j} \tag{2.17}$$

where $\overline{x}_j$ is the mean of variable j over all observations i. The weight w_j determines the scaling. If

- $w_j = 1$, the variables are just mean-centered.
- $w_j = \sigma_j$, with σ_j being the standard deviation of variable j over all observations, the scaling is called unit-variance (UV) scaling.
- $w_j = \sqrt{\sigma_j}$ is called Pareto scaling.
- $w_j = \frac{1}{2}\left(\max_i(x_{ij}) - \min_i(x_{ij})\right)$ is called orthogonal scaling.

For clarification, the first SNV-transformed, then mean-centered and UV-scaled spectra are shown in Figure 2.11. It can be seen that UV-scaling leads to an amplification of the regions, carrying no signal, in the spectrum.

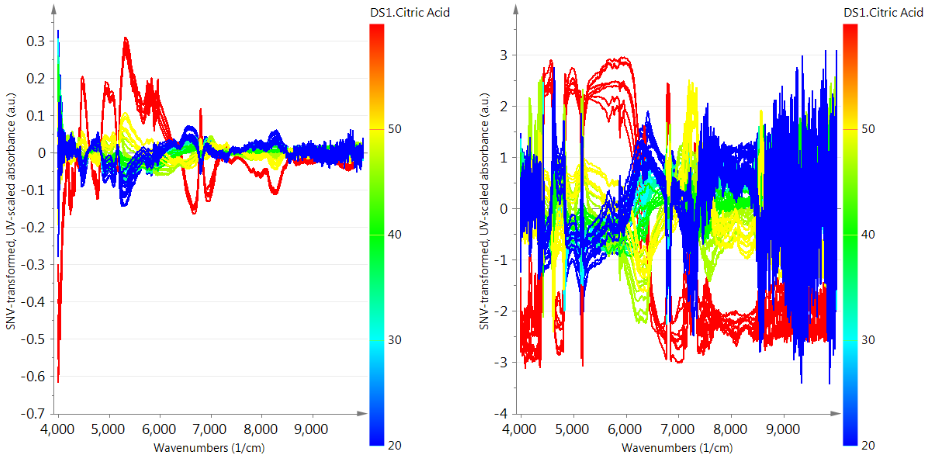

Figure 2.11: Left: SNV-transformed and mean centered spectra, Right: SNV-transfomred and unit variance scaled spectra. Notably, unit variance scaling overemphasizes the noisy region above 8500 cm^{-1}.

2.3.3 Principal Component Analysis (PCA)

Principal Component Analysis is a projection method, whose motivation is to describe the same information with less amount of data.

The N observations consisting of M variables form a data matrix X with dimensions $N \times M$. Hence, an observation can be thought to form a point in a M-dimensional space; All observations will build up a cloud of points in this space, as is indicated in Figure 2.12. Now, a new coordinate system is built, whose basis vectors are linear combinations of the original basis. These are called loadings or principal components, and chosen in such a way that the first principal component spans the largest variance of the data, the second is orthogonal and describes the largest fraction of variance still remaining, and so on. The so-called score values are the projections of the data points onto the principal components. As indicated in Figure 2.12, when knowing the scores on, and the direction of, the first principal component, this is already a good indication of the real position of a data point. When using all principal components, the original position can be restored again.

Especially for spectra which have a large number of correlated variables (e.g. intensities of neighboring wavelengths) this method can reduce the number of variables needed drastically.

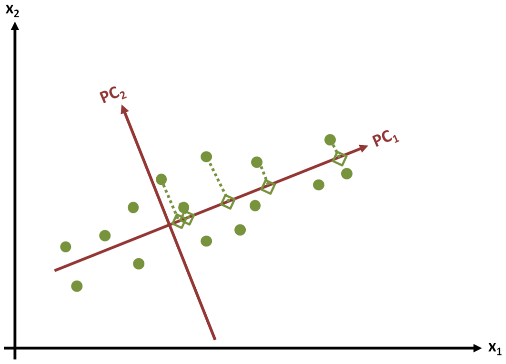

Figure 2.12: Two-dimensional illustration of the basics of principle component analysis. The projection of the data points onto the principal component is called score (indicated with diamonds). The observations (points) can be described either in their original variables (x_1, x_2) or via their scores (t_1, t_2) on the principal components (PC1,PC2). The orientation of the principal components in the original coordinate system is described by the loadings.

Mathematically speaking, the basis for PCA can be expressed as

$$X = TP' + E_A \tag{2.18}$$

with T the so-called scores and P' the loadings matrix. The loading matrix P has a dimension of $A \times M$, with every line representing a principal component. Those are sorted according to explained variance until the last used principal component A is reached. The score matrix T has a dimension of $N \times A$ and every line gives the coordinates of observation i on the A principal components. The matrix E finally describes the difference between the modeled data and the original data. The more principal components are used, the less this difference becomes, and finally for the possible maximum number of principal components $A = M$, then $E = 0$, as no data reduction is done anymore.

In Figures 2.13 and 2.14 the loadings and scores plot of the SNV-transformed spectra which were shown in the previous section, are displayed. When looking at the first principal component, it is evident that it resembles the spectrum of a chemical component, as shown in Figure 2.13. This confirms that the main reason for differences in the observed spectra are because of composition changes. The scores plot shows several things:

- Spectra measured consecutively form clusters, as those are most similar.
- Although the concentration level was not included in the data, the observations are roughly aligned accordingly. The concentration of citric acid decreases along the first principal component.
- Deviations along the second principal component reflect changes in the samples, other then concentration of citric acid.

Hence, combining the loadings and scores: an observation having a large score on the first principal component, can be expressed by deviating from the mean spectrum of all samples, in the same kind as the loadings of the first PC. The first PC was similar to the citric acid spectrum, but negative. Hence a large score reflects a lack of citric acid. Indeed the concentration level of citric acid was lower in those samples (knowledge which was not included into the analysis until now).

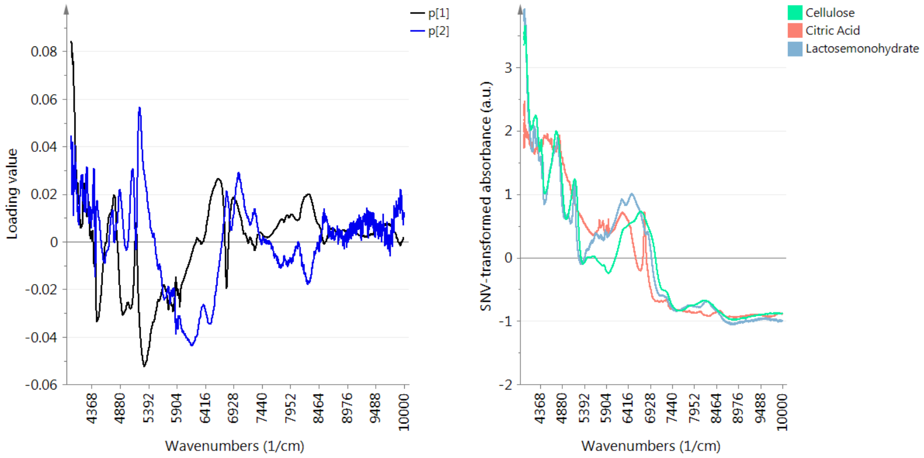

Figure 2.13: Left: Loading plot of the SNV-transformed spectra. The loadings are normalized such that $\sum_j p_{aj}^2 = 1$; Right: For comparison the pure spectra of the involved substances are plotted. The loadings reflect the pure spectra, although the sign of the first principal component is inverse to the spectrum.

On the individual data point level PCA looks like

$$x_{ij} = \overline{x}_j + \sum_{a=1}^{A} t_{ia} p_{aj} + e_{ij}(A) \tag{2.19}$$

with $\overline{x}_j$ being the mean value of x_{ij} over all observations i, sometimes called the 0^{th} component. If the data is centered, $\overline{x}_j$ is 0. p_{aj} represents the loading value for

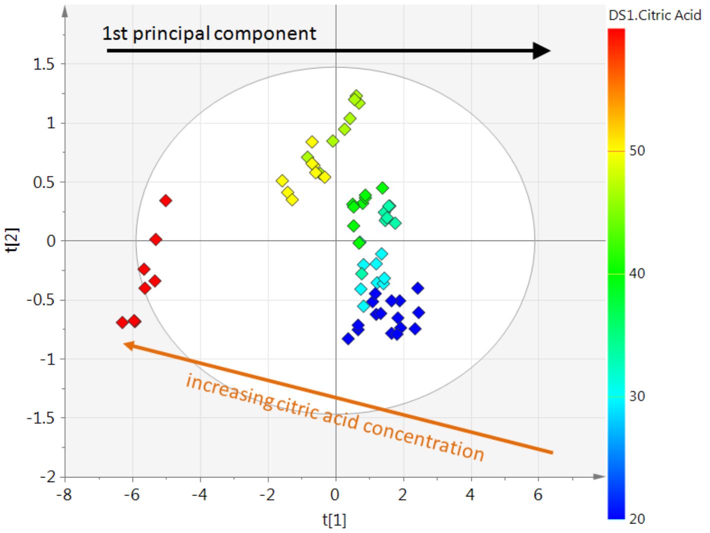

Figure 2.14: PCA - Score plot of the SNV-transformed spectra. The concentration of citric acid decreases along the first principal component.

variable j and principal component a; whereas t_{ia} represents the score value of observation i on principal component a.

Hence, when using only A principal components, x_{ij} can be estimated by

$$\hat{x}_{ij}(A) = \overline{x}_j + \sum_{a=1}^{A} t_{ia} p_{aj}, \tag{2.20}$$

and the difference between the real value x_{ij} and the estimated value $\hat{x}_{ij}$ is given by e_{ij} as

$$x_{ij} = \hat{x}_{ij}(A) + e_{ij}(A). \tag{2.21}$$

Every principle component explains some part of the variation, therefore an increasing number of principal components lowers the residual (unexplained variance). Often just a few principle components contain the important information one strifes for and are necessary to model the relevant data. Consecutive principal components may describe insignificant properties or measurement errors and lead to overfitting of the data. Chosing the right number of components is therefore a critical task [95]. However, to do that it is necessary to know, how much of the variance is described by a principal component.

The total variance is given by [95]

$$s^2 = \frac{1}{NM} \sum_{i=1}^{N} \sum_{j=1}^{M} (x_{ij}(A) - \overline{x}_{\text{total}})^2, \tag{2.22}$$

with $\overline{x}_{\text{total}}$ being the total mean of all samples and variables. The contribution of every principle component to an individual variable is given by

$$\hat{x}_{ij}(a) = t_{ia} p_{aj}, \tag{2.23}$$

so the explained variance of principle component a can be calculated by

$$s^2_{\text{PCA},a} = s^2 - \frac{1}{N} \frac{1}{M} \sum_{i=1}^{N} \sum_{j=1}^{M} (\hat{x}_{ij}(a) - x_{ij})^2, \tag{2.24}$$

and the explained relative variance for component a is then

$$r_a^2 = 1 - \frac{s^2_{\text{PCA},a}}{s^2}. \tag{2.25}$$

Often the overall explained variance

$$R^2 = \sum_{a=0}^{A} r_a^2 \tag{2.26}$$

is given and called the *coefficient of determination*. As a counterpart, the unexplained variance can be calculated using the residual matrix E, containing the elements e_{ij} [95, 97].

For the example above, the explained variance is given in Table 2.1. It can be seen that with increasing number of principal components the explained variance increases, and that 3 components (of 63 possible) already explain nearly 99% of the variance contained in the data (R^2 for $a = 3$).

Model and Data Quality Testing

To test the model for robustness, usually cross validation is used. For this method the data is split into groups. Then a model is built without that group, and consecutively the data of this group is projected into the model (i.e. their score values are calculated with the principal components already set-up), and the

a	r^2	R^2	q^2	Q^2
0	Cent.			
1	0.918	0.918	0.859	0.859
2	0.0572	0.976	0.662	0.953
3	0.0103	*0.986*	0.319	0.968

Table 2.1: Explained variance with increasing principal components. Column r^2 gives the explained variance per component a, and R^2 is the cumulative sum. q^2 and Q^2 is the corresponding cross validated explained variance. With only three components nearly 99% of the variance, contained in the data set can be explained.

modeled and actual values are compared. This is repeated until every group has been left out exactly once [97].

Naturally, great care has to be taken, when selecting how to group the data, as this strongly influences the quality of cross validation. It has become common that the number of groups should be around 7. When dealing with data of different concentration levels, all measurements belonging to a certain level should be in the same group. Otherwise predictions inside the group would be too easy, and the evaluation of the model incorrectly well.

The difference between modeled and actual values is noted as PRESS, the "prediction error sum of squares" given by

$$\text{PRESS} = \sum_{i=1}^{N} \sum_{j=1}^{M} \left(x_{ij} - \hat{x}_{ij,\text{CV}}(a) \right) \tag{2.27}$$

with $\hat{x}_{ij,\text{CV}}(a)$ denoting the modeled part according to equation 2.23 when the observation i was in the group omitted for model building. Equivalently to R^2 a term

$$Q^2 = \left(1 - \frac{\text{PRESS}}{s^2} \right) \tag{2.28}$$

can be constructed. Whereas R^2 indicates how good the model can describe the data, Q^2 is an indication how robust the model is against disturbances.

On the level of individual data points, statistical numbers, to asses the quality of single data points can be calculated. Most commonly are the Hotelling's T^2 value which gives the distance of a data point to the origin of the model, in the model plane, and is calculated for observation i by

$$T_i^2 = \sum_a \frac{\left(t_{ia} - t_{avg}\right)^2}{s_{ta}^2} \tag{2.29}$$

with t_{avg} being the average score (which is 0 for centered data), and s_{ta}^2 being the variance of the scores of component a in the model. Complementary, DModX gives the distance of an observation i to the model plane, and is basically

$$\mathrm{DModX}_i = \sqrt{\frac{1}{N-1} \sum_j e_{ij}^2} \tag{2.30}$$

[97].

2.3.4 Multiple Linear Regression (MLR)

Now for every observation i, there exists a dependent variable y_i usually called the response or target value. A possibility to create a statistical model, to further estimate the target variable y by independent variables x is multiple linear regression.

This method assumes a first order relationship between x and y

$$y_i = \sum_{j=1}^{M} b_j x_{ij} + g_i, \tag{2.31}$$

respectively in matrix form

$$\boldsymbol{y} = X\boldsymbol{b} + \boldsymbol{g}. \tag{2.32}$$

For the usual case $M < N$, i.e. more observations than variables, there is no exact solution, but the strategy is to minimize the length of the residual vector $\boldsymbol{g}$. This is usually done with the *least-squares method*, where the parameters are estimated by the inverse relationship

$$\boldsymbol{b} = (X'X)^{-1}X'\boldsymbol{y} \tag{2.33}$$

[99]. By using ANOVA (analysis of variance) confidence intervals for the gained coefficients can be estimated [100, 101].

However MLR fails if there are collinearities in the X-data, and noise might make it unstable.

2.3.5 Projection to Latent Space (PLS)

A connection between an independent variable matrix X, and a matrix Y of K dependent variables, or target variables, shall now be established [102].

The PLS estimates latent variables $\boldsymbol{p}_a$ as linear combinations of the original x-variables, similar to loadings in PCA. The X-matrix is reduced to an A-dimensional plane, and the data points are represented by scores t_{ia}. In a similar way the Y-matrix is reduced, giving the scores u_{ia}, representing the target variables y_{ik}. Concurrently, the $\boldsymbol{p}_a$, are chosen in such a way that the so-called "inner relationship" between the scores t_{ia} and u_{ia} enables to predict Y by X. A PLS can be performed on one or many dependent variables. However, if the responses are not correlated, a separate PLS for every response is preferred [95].

To sum up, the same outer relations, as for the PCA (see equation 2.18), are now used for both matrices, the independent variables X and dependent variables Y [99]:

$$X = TP' + E \tag{2.34}$$

$$Y = UQ' + F^*. \tag{2.35}$$

When not using the full number of possible PLS components, a residual remains for the independent and dependent variables (E and F^* respectively). At the same time the inner relationship connects both equations via

$$\hat{\boldsymbol{u}}_a = b_h \boldsymbol{t}_a, \tag{2.36}$$

with

$$b_h = \frac{\hat{\boldsymbol{u}}'_a \boldsymbol{t}_a}{\boldsymbol{t}'_a \boldsymbol{t}_a}. \tag{2.37}$$

In Figure 2.15 the inner relationship of the measured spectra (giving the scores t and the concentration giving the scores u is shown. This leads to the mixed relationship

$$Y = TBQ' + F, \tag{2.38}$$

where $||F||$ is to be minimized.

Weights $\boldsymbol{w}^*$ are introduced which can be interpreted the same way as loadings before,

$$T = XW^* \tag{2.39}$$

$$W^* = W(P'W)^{-1} \tag{2.40}$$

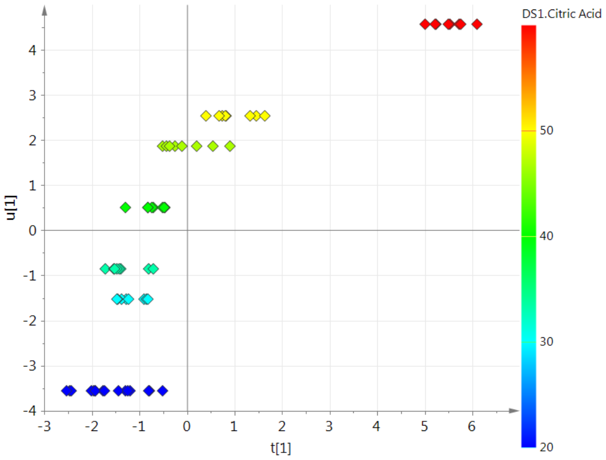

Figure 2.15: Inner Relation of the PLS. This connects the scores t, which stem from the spectral data, and u from the target variables, respectively. Here, they show a non-linear relationship.

[102]. The scores and loadings for the current PLS-model are displayed in 2.16 and 2.17. Obviously, those are very similar to the PCA results. However, the first PLS component has changed direction, as is reflected in the scores and loading plots.

The difference between PCA and PLS is that the first describes the *variance* inside the data X, whereas the latter describes the *covariance* between the independent X and dependent Y variables.

For estimating y-values by measured x-values, the calculated scores and loadings of the calibration are used and combined to a regression vector $\boldsymbol{b}_k$, forming the columns of matrix B,

$$B = W^* Q' \tag{2.41}$$

and a constant term $\overline{y_k}$, the mean over all i of y_{ik}; hence predictions of the target variables are gained by

$$\hat{y}_{ik} = \overline{y_k} + \boldsymbol{x_i}'\boldsymbol{b}_k \tag{2.42}$$

[95, 97]. Such a regression vector can be seen in Figure 2.18.

When the maximum number of PLS-components $A = M$ is used, the PLS and multiple linear regression give the same coefficients. However the advantage of the PLS is that collinearities and missing values can be handled.

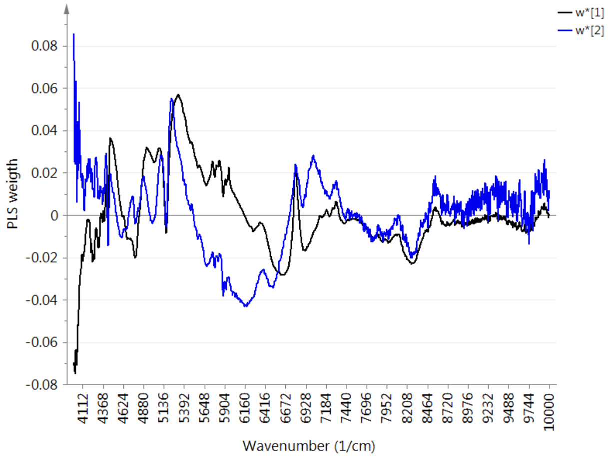

Figure 2.16: Loading weight plot of the SNV-transformed spectra. The loadings are similar to the PCA loadings, but the first PLS component is now aligned positively. The values are normalized, so that $\sum_j w_j(a) = 1$.

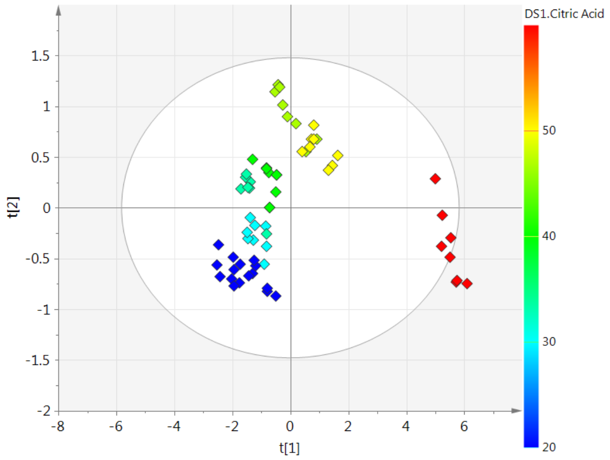

Figure 2.17: Score plot of the SNV-transformed spectra. The concentration level of acidic acid increases along the first PLS-component.

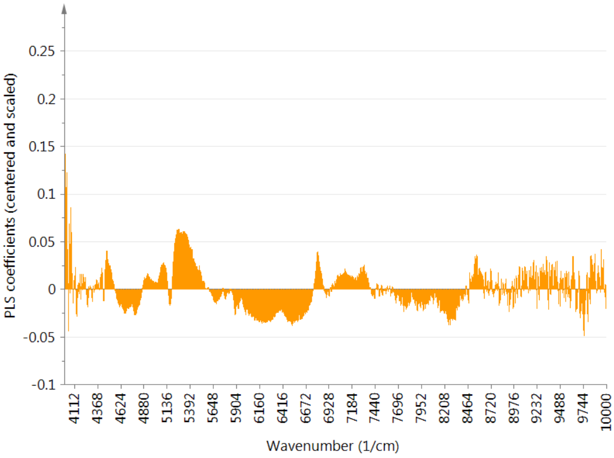

Figure 2.18: Regression coefficients for a PLS model. Especially for high wavenumbers, strong noise can be seen. This is caused by this region not being specific for the change in composition. Removing this region would lead to a better model.

Model and Data Quality Testing

The same quality variables as with PCA can now be calculated. However, instead of only comparing $\hat{x}_{ij}$ to x_{ij}, also the predictions $\hat{y}_i$ can be compared to reference values y_i. Therefore, again R^2 and Q^2 can be calculated, and furthermore

$$\mathrm{DModY}_i = \sqrt{\frac{1}{N-1}\sum_j f_{ij}^2} \tag{2.43}$$

For PLS-models naturally R^2 increases with the number of PLS-components used. On the other hand Q^2 increases, and then declines again, when overfitting takes over. Hence a for $\max_a(Q^2(a))$ is the maximum number of useful components. Again, chosing the number of components is dependent on experience, and might involve the shape of the loadings, the percentage of variance explained, the physical reasoning behind the useful number of components, and so on.

An important number describing the quality of the model is the root mean square error (RMSE) given by

$$\mathrm{RMSE} = \sqrt{\frac{\sum_{i=1}^{N}\left(\hat{y}_i - y_i\right)^2}{N}}. \tag{2.44}$$

If the reference values y_i are already included in the model, with which the predictions $\hat{y}_i$ are calculated, one speaks of the root mean square error of calibration (RMSEC). A more useful error is obtained, if cross validation is used, hence the model calculating $\hat{y}_i$ did not include y_i; then this is called the root mean square error of cross validation (RMSECV). As a rule of thumb, the uncertainty of a predicted value is $\pm 2 \cdot \text{RMSECV}$ [20, 103]. If a completely independent test set is used, this is called the root mean square error of prediction (RMSEP).

A graphical intuitive way of estimating the quality of a model is the observed vs. predicted plot which shows the reference values, vs. the values obtained by the model, as can be seen in Figure 2.19. This gives a good hint on the quality and uncertainty of predictions, as well as an indication of a possible non-linearity in the data.

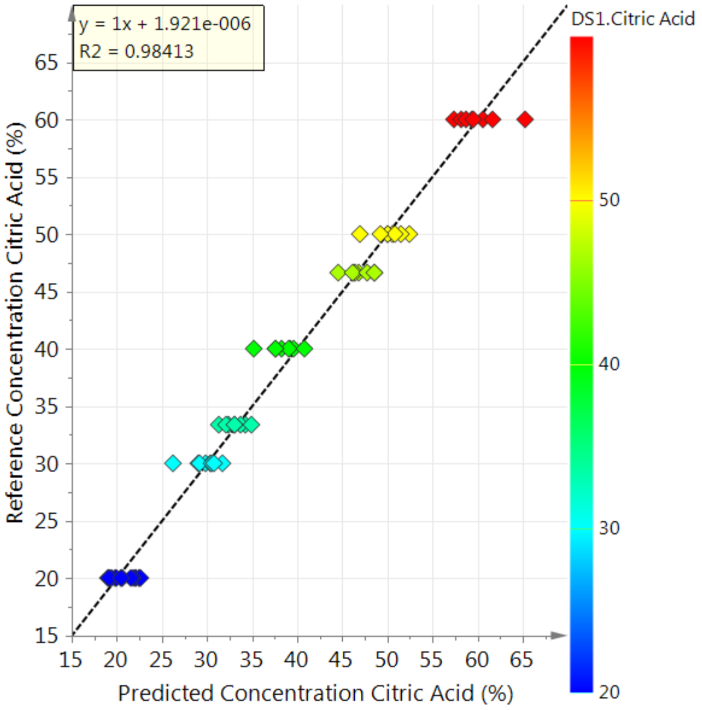

Figure 2.19: Reference (or observed) values are plotted against their predictions. In the ideal case, this would give a straight line. This so-called “observed vs. predicted plot” can provide information about the quality and scattering of the predictions, non-linearity of the model, outliers, etc.

An uncertainty for predictions can also be gained using the leverage effect. This is based on a fact that samples having a larger score, tend to be more influential in determining the principal components, or PLS-components. Therefore, a confidence interval for coefficients and predictions can be gained, of the form

$$I_i = t_{\frac{\alpha}{2},N-\mathrm{df}} \cdot s_i \tag{2.45}$$

with $t_{\frac{\alpha}{2},N-\mathrm{df}}$ being a student-t factor, dependent on the number of calibration samples N and the used degrees of freedom df, and a standard deviation of the prediction error s. Several possibilities to calculate s exist, as explained in [104, 105]. Different ones are implemented in different software, but they all share the common important property that the error increases, if the observation is far from the model plane (DModX is large).

Further, a point to stress is that the most extreme measured points of a model, are also its borders of validity, and extrapolation is strictly not possible. Even more so, it is recommended that observations of interest should be well *inside* the model and not at the borders. Additionally, PLS is based on a linear relationship which might not be true, if the region investigated (e.g. concentration range) is too large; in such a case finer models, just covering a smaller subrange should be introduced.

2.3.6 Alternative Methods for Quantitative Spectral Interpretation

PLS is clearly the most popular method for relating NIR-spectra to a target variable. Nonetheless it is worth to take a look at competing methods.

First of all, PLS has spawned several more modern methods, most prominently *Orthogonal PLS* (OPLS) [97], which has the advantage of separating variation in X into a part related to Y and a part orthogonal to Y (and hence describing variation in the data which is not related to the target variable) [106].

Multivariate Curve Resolution is based on PCA, but has the advantage that knowledge, like pure component spectra, and other boundary conditions, like closure can be included. This method further extracts feasible physical spectra from the data, if the concentration levels are known [107].

Science Based Calibration is a regression based method which allows to include models of the raw spectra and the measurement noise, and hence needs less calibration samples than the other methods [108, 109].

A completely different ansatz is brought forward by *Indirect Hard Modeling*, which splits the spectra into individual peaks. Spectra of mixtures can than be constructed from the peaks of individual components and hence allow the estimation of concentration levels [110, 111].

2.4 Mixing of Solids

2.4.1 Mechanisms of Mixing and Segregation

Mixing is based on two different mechanisms. The first one is *convective blending*, which is the transport of large volumes of the blend, forced by the blender. Hence, convective blending is largely influenced by the geometry of the blender, the direction of mixing is aligned with the direction of the particle movement, and happens rather fast. Such, convective blending forms homogeneity on a large scale [68, 112].

The second mechanism is *diffusive blending*. This is a result of the individual particle movement with respect to the particle collective, and perpendicular to the particle flow. Diffusive blending is based on the different mobility of particles which is caused by different particle properties. Hence, the particle size and shape, density, cohesion, and other factors affect diffusive blending. Diffusive blending is slower than convective blending, and leads to homogeneity on a small scale [112, 113].

A competitive mechanism to blending is segregation. This is the demixing and spatial separation of mixture components [113] and is imminent if particles do not have identical properties. Segregation occurs for several reasons, such as differences in density, size, shape, surface properties, friction coefficients and other physical parameters [59]. A well-known example is the "Brazil nut effect", caused by size differences of the particles. Movement of the powder particles leads to an enlargement of the voids in the powder bed. Gravitational force acting on the powder, allows smaller particles to pass downwards into voids. This leads to a net upward motion of larger particles which accumulate at the top of a blend, e.g. Brazil nuts in a muesli [112, 114].

Small difference in particle properties can already lead to segregation, but are hard to quantify and predict, due to the many influential parameters. The final state of a blend is a equilibrium between blending and segregation. Segregation can therefore alter blending times or even prohibit the formation of a sufficiently homogenous blend [73, 112, 115]. Hence, whenever there is movement induced in the powder bed, e.g. by vibration, the chance for segregation exists, making the detection of segregation a vital task in an industrial environment.

2.4.2 Mixture Homogeneity

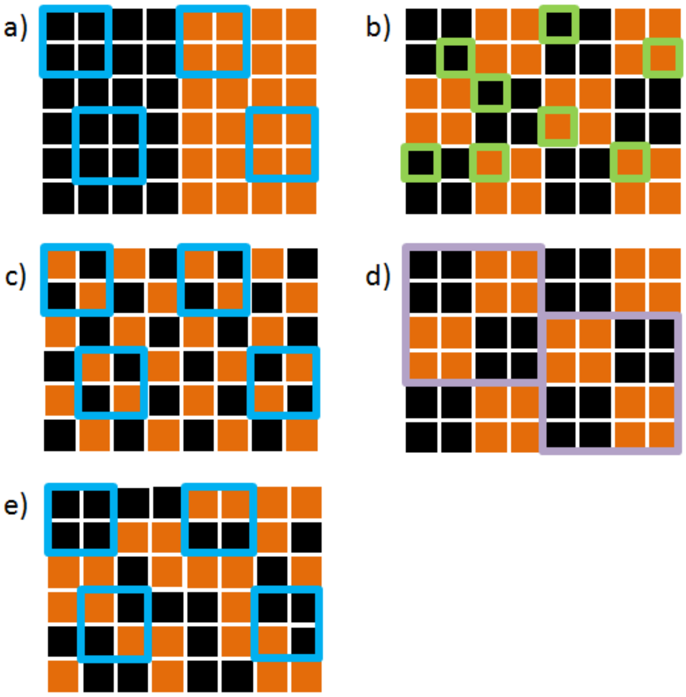

Figure 2.20: Examples for different homogeneity levels. The black and orange squares represent blend fragments of different species, the colored frames represent samples taken. Sketches a) and b) show completely separated mixtures; c) and d) show homogeneous mixtures. Note that the degree of mixedness is the same in b) and d), but the sample size, and hence the depth of scrutiny, at which homogeneity is tested, has changed. Image e) represents a stochastic mixture, however due to the finite fragment size, only discrete concentration levels of $c = 0, 25, 50, 75, 100\,\%$ can be sampled.

Different possibilities to express the homogeneity of a mixture exist. However, most of them are based on the variance in between different samples drawn from the mixture [113].

As the nominal concentration c is known, the empirical variance would be the result of

$$s^2 = \sum_N \frac{1}{N}(c_{\text{sampled}} - c)^2. \tag{2.46}$$

If a two component mixture is assumed, where one component is present in concentration c, and the second component in concentration $1 - c$, the border cases for the achieved variance can be constructed easily. A pictorial expression of this procedure is shown in Figure 2.20.

- For a completely separated mixture, with a probability of c, a sample containing only the first component (hence $c_{\text{sampled}} = 1$) is drawn, and with probability $c - 1$ a sample containing only the second component ($c_{\text{sampled}} = 0$) is drawn, giving the overall variance

$$\sigma_0^2 = c \cdot \sum_N \frac{1}{N}(1-c)^2 + (c-1) \cdot \sum_N \frac{1}{N}(0-c)^2 = c\,(1-c) \tag{2.47}$$

- For a completely homogeneous mixture, every sample taken should have the concentration c and hence the variance be

$$\sigma_h^2 = \sum_N \frac{1}{N}(c-c)^2 = 0; \tag{2.48}$$

- As mixing is a random process, a completely homogeneous mixture can not be achieved. Thus, the aim is the stochastic homogenous mixture. In such a mixture, the possibility to find a particle of the first component, is proportional to its concentration, and independent of the surroundings. Hence, when sampling a volume of V_S, it should contain $c \cdot \frac{V_A}{V_S}$ particles with volume V_A of the first component. This leads to the variance of the stochastic homogenous mixture to be

$$\sigma_z^2 = c\,(1-c)\,\frac{V_A}{V_S} \tag{2.49}$$

  However, for this to be true, the particles should not be spherically hindered. Hence V_A actually is the effective particle volume (also including the surrounding voids in the bulk) [116].

Hence, concentration of a granular media is slightly more complex than the concentration of a liquid. This is based on the fact of the existence of finitely large fragments which can not be parted any more. A sample taken, therefore, consists of a certain number of fragments.

The resulting measured variance therefore is the combination of

- Variance due to compositional heterogeneity (i.e. caused by finite particle size)
- Variance due to distributional heterogeneity (i.e. a not well mixed blend)
- Variance due to measurement and model (e.g. detector noise, etc.)

As indicated in equation 2.49, the variances when measuring just a single component therefore allow an estimation of the size of variance due to measurement and model.

2.4.3 Concept of Depth of Scrutiny

Equation 2.49 shows that the measured homogeneity is determined by the size of the sample [113]. Therefore, to determine homogeneity, one has to define the scale, at which to look for it [67].

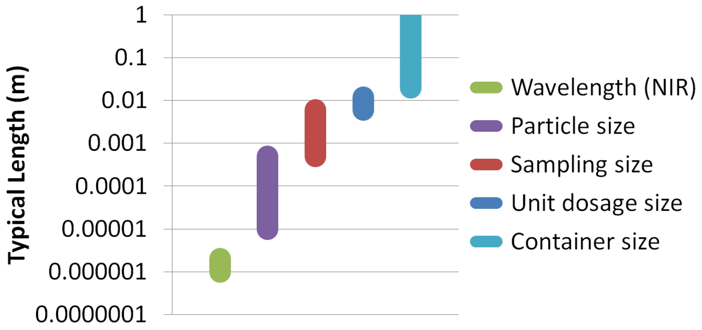

Figure 2.21: Typical length scales for the processes and measurement techniques in this work.

The obvious limit is the particle size at the lower end of scale (at which a blend is necessarily inhomogeneous) and the whole container (e.g. blending vessel) at the upper end of scale, at which homogeneity is given for sure (see Figure 2.20). A proper sample should therefore be large enough, to avoid the effect of individual particles, but much smaller than the overall mixture. At the end, the relevant sample size is dependent on consecutive operations, and their demand on homogeneity.

Moreover, in the pharmaceutical industry, there is an overall relevant size: the so-called "unit-dosage form". This is the amount of material which is finally administered to the patient at a time (in most cases, a tablet). Naturally, the potency of the unit-dosage form has to be strictly defined and confirmed, and homogeneity has to be assured at exactly this size level. As a drawback, the final dosage form is at the end of the production process, hence for intermediate products, the relevant size has to be estimated.

Unfortunately, the relevant size for downstream process steps, the size of single samples sampled, and the overall batch size of the material can span several orders of magnitude, as is depicted in Figure 2.21. Therefore, it is necessary to determine the volume that is sampled by NIR. This can be done by geometrical reasoning, and determining the penetration depth of NIR into the powder bed. Methods to determine the penetration depth are described in [27], and quite some literature deals with the determination of the effective sample volume, either experimentally [117–119] or theoretically [120, 121].

To goal for supervising blending is [11]

1. to garantuee the homogeneity of the blend.
2. to determine the time, at which sufficient blending is reached, as to stop the process timely.

2.4.4 Determining Homogeneity In-Process

Often homogeneity is determined by manually drawing samples at several positions inside the blender [73, 122]. With near-infrared spectroscopy, manual sampling (and hence interruption of the process) is not necessary anymore, but can happen during the running process through a probe window.

Different strategies can be used to monitor the blending process with NIR-spectroscopy. A possibility is to directly look at the spectra, and the changes of spectra. A common concept is *Moving Block Standard Deviation (MBSD)*. In this procedure, the standard deviation for a certain wavelength, over a block of spectra recorded consecutively, is calculated. Then the oldest spectra in the block is removed, and a new one added, the calculation then redone, and this procedure repeated as long as the process lasts. When the moving block standard deviation drops below a certain value, one can assume that the mixture is not changing any more. This method does indicate, when a stationary state is reached, where further blending does not influence the quality of blend anymore. However, it does not give information on the actual concentration level, and hence the actual homogeneity [22, 123].

Consequently, a chemometric model has to be applied, to give information on the concentration measured with NIR [83]. If already the concentration is estimated by the spectra, then the variance can be calculated based on the concentration levels. In this case however, different samples have to be drawn, either at different time steps, or at different positions. Naturally, measuring simultaneously at several positions is an advantage here.

2.4.5 Confidence on Concentration and Homogeneity

As particle size and sample volume are now defined properly, the relationship

$$\frac{V_A}{V_S} = \left(\frac{z\,(1-\alpha)}{\Delta c} \right) (1-c)\,c \tag{2.50}$$

can be used [113]. The important property is the number of fragments $\frac{V_A}{V_S}$, which can be placed in the sampled volume. This is connected to the confidence interval Δc of the obtained concentration, just caused by the finite particle size. The factor $z(1-\alpha)$ originates from a student-t factor and relates to the level of confidence (for a 95% ($\alpha = 0.95$) confidence interval $z(1-\alpha) = 1.65$).

Now that the fundamental error in prediction is known, the error of homogeneity can be assessed. When calculating the variance across several samples, the number of samples determines the accuracy of the experimental variance. Experimental variance s^2 and theoretical variance σ^2 are related in the following way

$$\frac{\sigma^2}{s^2} = \frac{f}{\chi^2_{1-\alpha}(f)} \tag{2.51}$$

where f denotes the degrees of freedom and $\chi^2_{1-\alpha}(f)$ is the χ^2-distribution for a confidence level α and f degrees of freedom which is in the empirical case the number of samples $n-1$. Hence an upper limit b^2 of the true variance σ^2 can be given by

$$b^2 = \frac{f}{\chi^2_{1-\alpha}(f)} s^2 > \sigma^2. \tag{2.52}$$

2.5 Fluid Bed Coating

Fluidized beds are widely used in the pharmaceutical industry. Offering a large particle-to-air contact surface, good mixing and excellent mass/heat transfer characteristics, they often are the method of choice for drying and coating of granular materials, as well as for granulation [124, 125]. In the latter two unit operations, a liquid spray is introduced that adds the coating or granulation liquid. Different set-ups, including bottom and top spray systems, Wurster designs (intended to induce a toroidal recirculation pattern of particles) or designs inducing a radial flow component have been introduced over the last years. Even continuous fluidized beds have been introduced.

Nonetheless, the efficiency of fluid beds often depends on the experience of operators, since beds are sensitive to subtle changes that can significantly affect the flow pattern or compromise the pneumatic transport enabled by a fluidized bed process. Moreover, scale-up and scale-down are not trivial and no general rules exist for a broad range of applications and materials. Nevertheless, significant fundamental research (e.g., the work of Roy Jackson [126] and others) has been performed and an extensive body of literature exists [127, 128]. Recently, fluidized systems have been studied extensively via advanced simulation methods (e.g., the coupling of computational fluid dynamics and discrete particle methods) and research is still ongoing [129, 130].

In addition to modeling and simulation which are prerequisites for the design, optimization and implementation of advanced control strategies; real-time process monitoring is another critical tool for making control strategies work. However, placing sensors into a fluid-bed environment is challenging, in terms of the quality and information content of the acquired data (e.g., spectra). Numerous problems exist, window fouling being one of them.

Near-infrared spectroscopy (NIRS) is a proven monitoring technology that has been used in fluidized beds [60, 131]. Due to the sensitivity of NIRS to water, several applications involving end-point determination in fluidized bed dryers and tablet coating have been reported [132, 133].

3 Materials and Devices

3.1 Spectrometers

Three different spectrometers, with different working principles, have been used in the course of this work.

Perkin Elmer Spectrum 400

The Perkin Elmer Spectrum 400 FT-IR/FT-NIR Spectrometer is a benchtop instrument. For the current work, it was only used in its NIR configuration.

Spectra can be collected in the range of 15000 to 1250 cm^{-1}. A deuterated triglycine sulphate (DTGS) detector is used. Usually an external trigger probe, connected via an optical fiber to the instrument was used. Hence the interesting wavelength reagion was cut to 12000 to 4100 cm^{-1} due to absorptions in the optical fiber [134].

When starting the instrument, and in regular intervals, a self-check is applied, verifying the proper working of the instrument.

EVK Helios Starter Kit

The EVK Helios Starter Kit is a push-broom system for the NIR-region. Two tungsten-halogen lamps provide the illumination of the sample. A line focus determines the detection area. The beam path is then led through a disperse element (in this case a prism-grating-prism system) and projected onto a focal plane array.

This allows the determination of an individual spectrum for every pixels on the detection line. The used system provided 256 spatial pixels, each offering a spectrum in the range of 1000 - 1600 nm, distributed on 316 pixels.

By moving a sample perpendicular to the detection line, an area can be scanned. An image of the system is provided in Figure 3.1.

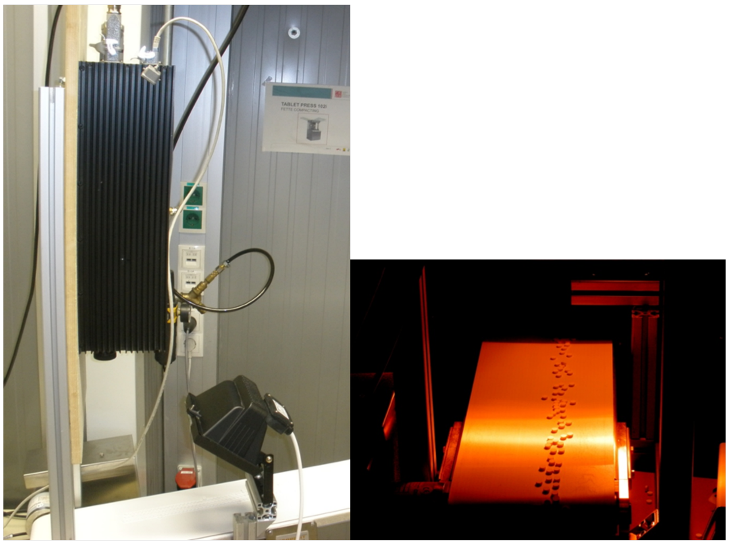

Figure 3.1: Experimental set-up with the EVK Helios Starter-Kit over a conveyer belt is shown on the left. On the right the illuminated area can be seen, giving an idea about the line of detection (orthogonal to the conveying direction).

EVK Helios EyeC Multiprobe System

The last system was considered a prototype during the time of this work. It actually is a modification of the previously mentioned Helios Starter Kit, with the following differences

- An optical adaption unit was added to the system. This allowed the docking of typical NIR-probes (with SMA-905 connector) to the system. Up to 25 probes can be connected, and their signal is projected to the entrance slit of the system. Hence, the imaging device has turned into a multiprobe system. This can be seen in Figure 3.2.
- A more expensive MCT-FPA (mercury cadmium telluride - focal plane array) was used, stretching the detectable wavelength range to 1000 - 2300 nm. This range is split into 256 pixels.

- An independent light source further enhances the flexibility of the system. Here a transportable light source from Polytec SAS (Chatillon, France), with a special adapter to plunge fiber optics was used.

As this system was a new development, it was thoroughly tested for its applicability which is the topic of chapter 4.

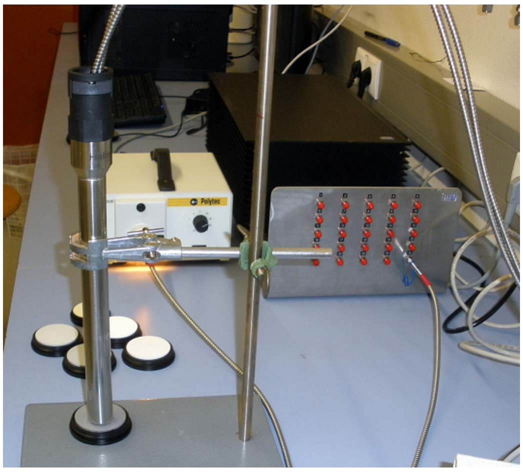

Figure 3.2: Image of the laboratory workbench. On the right side the spectrometer with the 25 docking ports can be seen. On the left side, at the background the light source is located; at the front an NIR probe and several reflection standards are pictured.

3.2 Optical Devices

Optical Switch

A fiberswitch (FSM2 (1x6) piezosystem jena GmbH, Jena, Germany) was used in combination with the Perkin Elmer Spectrometer. Using the switch, any of the six connected fiber pairs could be activated and connected to an additional incoming pair that led to the ports of the spectrometer used for an external NIR-probe.

With this setup, not only one probe but any of the probes attached to the vessel delivered information regarding the process status. In practice, an automated program consecutively switched the channels, one after another, for short intervals of time. However, only one position could be monitored at a time. A drawback of this system is that due the fiber switch and additional optical interfaces, some light intensity is lost, deteriorating the signal-to-noise ratio. Moreover, spectra acquired during the actual switching between channels must be discarded.

Optical Fibers

The used optical fibers were purchased from Ocean Optics (Ostfildern, Germany). Fibers with a steel jacket and 600 μm core diameter were chosen. All fibers can be connected to the spectrometer, and to each other by SMA905 gauges.

The fibers have a minimal bending radius of 15 cm which has to be adhered to strictly, in order to avoid not only damage of the fiber, but also spectral artifacts.

3.2.1 Near-Infrared Probes

Cupped Bifurcated Fibers

A very simple NIR-probe set-up is the utilization of bifurcated fibers. Every probe consisted of a sapphire window with a stainless steel frame and a bifurcated fiber in direct contact with the window. The bifurcated fibers consisted of two optical fibers each: one for illuminating the detection spot and the other one for collecting the diffusely reflected light. The resulting detection spot was determined by the fiber core diameter of 600 μm and the aperture angle at the fiber cutoff.

Hellma Diffuse Reflectance Probe

Such a probe offers more illumination spots, surrounding the detection spot, and hence gives a more representative spectrum of the sample material, than the above mentioned cupped fibers. More information on this probe can be acquired by the manufacturer Hellma Analytics (Hellma GmbH & Co KG, Müllheim, Germany); The whole probe is seen in Figure 3.2, and a close-up of the head in Figure 2.5.

3.3 Powder Handling

Tumbler Blender

A tumbler blender (Turbula T2F, Willy A. Bachofen AG Maschinenfabrik) was used to prepare preblends of pharmaceutical powders. Because of its working principle, i.e. rotation along several axis of a drum, the tumbler blender is suitable for blending small amounts of powders rather well, without inducing a large amount of stress on the material.

Electric Turntable

A typical laboratory turntable with tunable speed (Sensor Turn, WLD-TEC GmbH, Göttingen, Germany), was used to simulate powder movement. A series resistor was placed in the turntable, to further reduce its rotating speed.

Customized Blending Vessel

In our work we used a stainless steel blending vessel with an inner diameter of 10 cm (see Figure 3.3), and a four-bladed stirrer. To monitor different positions, the vessel is equipped with seven ports for NIR-probes that were distributed evenly along the side wall of the vessel. Additionally, three ports were positioned at the base plate of the vessel, at different distances from the axis. The outermost location was in the corner of the vessel - a critical position for the blending process. The four-bladed stirrer was made from stainless steel and connected to a gear motor (Heidolph RZR 2101, Heidolph Instruments, Schwabach, Germany). Its diameter allowed gaps of 1 mm between the wall of the vessel and the stirrer as well as between the bottom and the stirrer.

This set-up is a simplified model system for agitated industrial blenders and may be seen as a scaled-down version of high-shear mixers or filter-bed dryers.

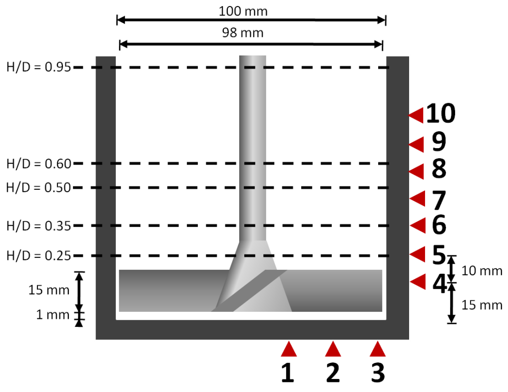

Figure 3.3: Schematic illustration of the blending vessel. Arrows mark the positions of ports for NIR measurements, and the dashed lines indicate different filling levels.[1]

Continuous Feeding

A Gericke feeder (Gericke DIW-KE-GLD87-15-VR, Gericke AG, Regensdorf, Switzerland), with a spiral as conveying element, was used for the continuous feeding of powder.

Continuous Blending

For continuous blending, the Hosokawa Micron BV (Hosokawa Micron Powders GmbH, Köln, Germany) was used. This is a single axis paddle blender with variable (but fixed in our case) paddle angle.

Hot Melt Coating Device

The coating apparatus was an Innojet® Laboratory System Ventilus® V-2.5/1 with an Innojet®Hot-Melt-Device IHD-1, manufactured by Innojet Herbert Hüttlin

---

[1] With kind permission from Springer Science+Business Media: AAPSPharmSciTech, Monitoring Blending of Pharmaceutical Powders with Multipoint NIR Spectroscopy, 14, 2004, 234-44, Scheibelhofer et al., Figure 2.

(Steinen, Germany). The device is a multi-purpose system for granulation, coating, and hot-melt coating which provides good up-scaling characteristics from laboratory to production scale.

3.4 Analytic Devices

Particle Size Analysis

Particle size analysis was done with a system from Sympatec (System-Partikel-Technik GmbH, Clausthal-Zellerfeld, Germany). The subunit VIBRI/L, a vibrating chute, feeds the powder to a dry-dispersion unit (RODOS/L). The dispersed particles are then analyzed, by acquiring two-dimensional images of the falling particles, illuminated with a stroboscopic light and captured with a high speed camera, in the QICPIC unit. The size of particles is then determined using the method of EQPC (equivalent projected circle) diameter [135].

3.5 Software

Several different software products were used in this work.

Two programs are dedicated to multivariate data analysis. Hence, chemometric data analysis, spectral transformations and model building was done with those.

- TheUnscrambler (Camo Software AS, Oslo, Norway) was used in the versions 9.8, 10.0, 10.1, and 10.2 .
- SIMCA (Umetrics, Umeå, Sweden) was used in the versions 12.0, 13.0, 13.0.3 .

For establishing experimental designs, and testing factors for significance, Modde (Umetrics, Umeå, Sweden) in Version 9.0, 9.1 and 10.0 was used.

For large amounts of data, as delievered with the imaging system, but also for data handling, consolidation, and conversion Matlab (MathWork, Natick, Massachusetts, USA) was used in Version 2011b. Chemometric applications, like PCA etc, are included in the *Matlab Statistical Toolbox*.

For certain calculations and the creation of illustrations Microsoft Office Excel 2007 (Microsoft, Redmond, US) was used.

3.6 Materials

Materials for Dosing and Blending

Binary blends were produced from two model substances. The first one was acetylsalicylic acid (ASA) from Rhodine by Rhodia group (La Défense, France), which is a well-known active pharmaceutical ingredient (API). The second substance was Tablettose 80 from Meggle GmbH (Wasserburg, Germany) that consists of α-lactose monohydrate (LM) but is granulated and has a well-defined size distribution.

To illustrate the particle properties of the two materials, images were taken with a reflective-light microscope (Wild Heerbrugg), as shown in Figure 3.4. Their properties are summarized in Table 3.1.

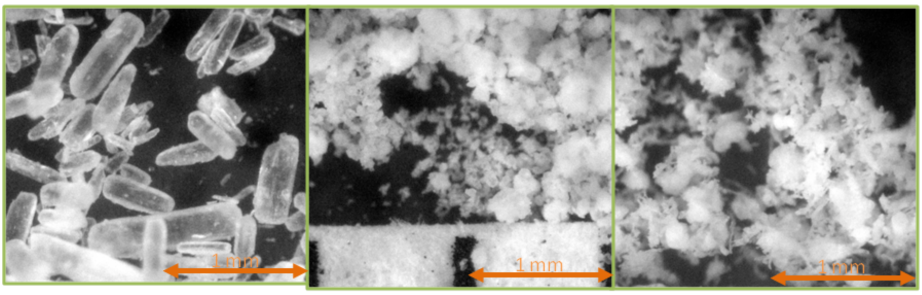

Figure 3.4: Images of the particles used. Left: Acetylics salicylic acid, Center: Lactose mono-hydrate, Right: Microcrystalline cellulose

Both substances are significantly different in shape and size. The smaller component, LM, forms spherical granules, with a mean particle size of 184 μm. The q3-distribution (Figure 3.5) shows a rather broad distribution. The prominent shoulders indicate that particle breaking and agglomeration have occurred. Moreover, LM exhibits a larger porosity than ASA. The second material, ASA, forms needle-shaped crystals. This non-spherical shape leads to a non-isotropic particle orientation and different particle mobility.

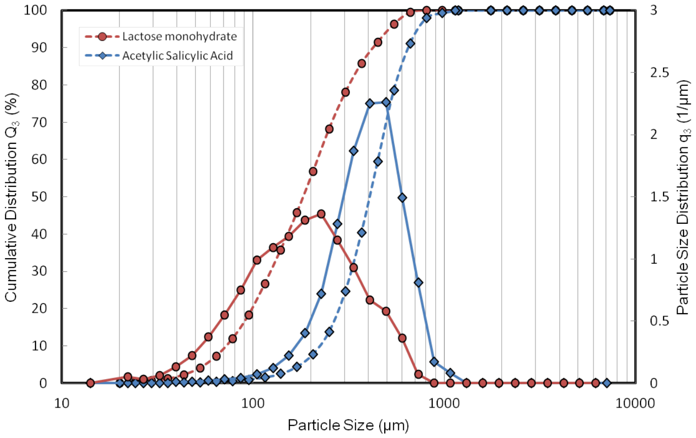

Figure 3.5: Size distributions of the materials obtained via a dispersion and imaging system (Rhodos and QicPic-System by Sympatec GmbH), using the method of equivalent circle projection diameter (EQPC). Blue diamonds: ASA (x_{50} = 409 μm, b = 1.04). Red circles: LM (x_{50} = 184 μm, b = 1.93). The full lines represent the particle size distribution, the dashed lines represent the cumulative distribution.

Powder	ASA	LM	MCC
Bulk Density (kg/m^3)	760 ± 20	640 ± 10	380 ± 20
True Density (kg/m^3)	1400	1550	1500
Porosity	0.46 ± 0.01	0.59 ± 0.01	0.75 ± 0.01
d_{10} (μm)	252 ± 4	75 ± 1	63 ± 1
d_{50} (μm)	434 ± 9	192 ± 3	136 ± 1
d_{90} (μm)	706 ± 25	422 ± 6	260 ± 2

Table 3.1: True and bulk density of the materials. True density was taken from literature, bulk density was measured with the FT4 Powder Rhoemeter (Freeman Technology, Tewkesbury, United Kingdom). Porosity was calculated by those two values. The particle sizes refer to a q_3-distribution, obtained with QICPIC. The mean and standard deviation of 3 measurements are given.

Differences in particle density and mobility induce segregation. Nonetheless, difference in particle size is the main cause for segregation [116] due to several mechanisms, namely different trajectories of the particles, sifting segregation, the percolation of fines, and the rise of coarse particles in a moving powder bed [136]. Great care has therefore been taken to avoid segregation during the regular handling of the blends.

The third used substance in the dosing experiments was micro-crystalline cellulose, of the form Avicel 102 (FMC Biopolymer, Philadelphia, USA). Cellulose forms spiky spheres, as shown in Figure 3.4. A summary of the particle properties can be found in Table 3.1.

Materials for Coating

The substrate material was a crystalline material. To ensure a specific size range it was sieved before the application. The substrate crystals were provided by Hermes Arzneimittel GmbH.

The coating material was the lipid Compritol ATO 888 (Gattefossé, Nanterre Cedex, France). The recrystallization temperature of molten Compritol ATO 888 is between 69-74° C. To have an idea about the behavior of this certain lipid, butter is a fine model substance, as it exhibits the same low melting point, and the same greasy behavior in its solid form.

4 Determination of Equivalency for Multipoint Measurements

4.1 Equivalency of Measurements

The crucial point for multipoint measurements is, naturally, to gain comparable measurements. Differences in the acquired spectra can either stem from the measurement set-up and probes, or the samples. However, as the difference in samples is the property of interest, deviations caused by other sources have to be eliminated. The equivalency of measurements has to be guaranteed.

Referring back to possible multipoint measurement set-ups, when using exactly the same spectrometer, but for different probe positions consecutively, this is already an issue. Even more so, this is true if the beam path is not the same. The next sections deal with the validation of the new multipoint-spectrometer prototype, and give some insight which is important for the following experimental work.

4.2 Concept of A Multipoint Spectrometer

For the already described multiprobe system, it is necessary to prove the comparability between spectra measured with identical probes, but at different ports of the same spectrometer. Two different methods have been used to ensure the transportability of chemometric models between the different ports of the spectrometer.

An obvious method is the direct comparison of the different ports. This is done by measuring reference materials; here a reference set of gray standards for the NIR region (FSS-08.-02c, Avian Technologies LLC, Sunapee, New Hampshire, USA) was used. The ports were compared regarding:

1. Measured intensity
2. Wavelength mapping
3. Signal to noise ratio and dynamic range

For all these points consideration has to be taken into account if it is necessary to perform correction steps and in which way to do this. The following correction methods are thinkable:

1. As the reflected intensity is transformed into pseudo absorbance, a different intensity measured under the same circumstances for different channels does not have any direct effect on comparability. The reason is that this should be circumvented by the reference measurement of the white reflection standard. However, different gained intensities will be reflected in the signal to noise ratio and the dynamic range of the regarding ports.
2. As usual regression-based chemometric models rely on a proper multiplication of wavelength and regression vector, a shift in wavelengths will lead to drastic effects. When the wavelength mapping function (i.e. the function connecting pixel position and corresponding wavelength) is known for each port, it is possible to establish a mapping model in between ports. However, care has to be taken to choose the right way for determining interpolated regression values.
3. Signal to noise ratio and dynamic range may not lead to a wrong predicted value, but rather influence the performance of the model. A direct corrective action (apart from hardware changes) is not apparent. However a very practical approach is to assign probes, where the highest sensitivity is needed (e.g. determining accurate concentration levels) to the most sensitive ports.

By determining if the above mentioned correction methods are necessary transportability of the chemometric model between ports should be guaranteed.

4.2.1 Hardware and Software Aspects

The system is based on the previously successful push broom spectrometer series “Helios” by EVK DI Kerschhaggl GmbH. The detector is a new CCD-based semiconductor detector with HgCdTe elements to span a larger wavelength region. The detector chip consists of 256 x 320 pixels. The 320 pixels are grouped to serve as targeting region for the respective 25 ports, as seen in figure 4.1. However, only one pixel line congruent with the maximum intensity given by that port is reported. Nonetheless, for bad pixel correction neighboring lines are considered. Along the 256 pixels the wavelengths are split up. The splitting is achieved with a prism-grating-prism (PGP)-system.

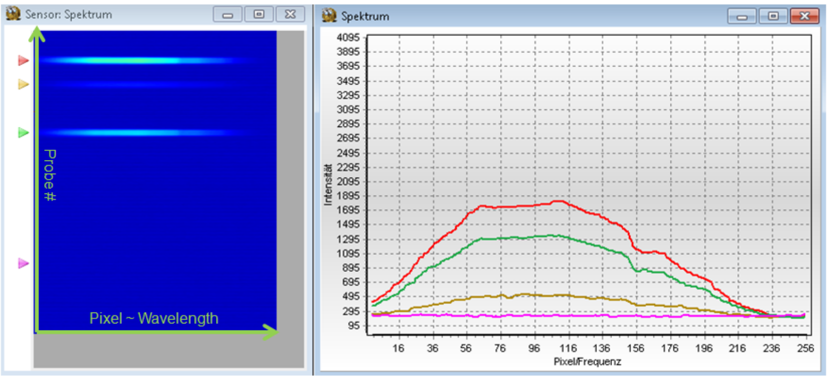

Figure 4.1: Screenshot of the HeliosViewer. The image on the left represent the counts on the chip. On one axis the different ports are mapped, the other axis the wavelenghts differ. On the right side four spectra, currently on the chip, are displayed.

A new adoption is the dark current adjustment. To achieve this, a shutter closes the light path on a regular basis and the dark current is detected. An algorithm then adjusts the dark current correction.

The software used to command the spectrometer, was the HeliosViewer (Version 1.29.2012.1), also provided by EVK. This program allows some data pretreatment steps:

- *Region of Interest*: That actually is the selection of the pixel lines representing the ports. This can be deactivated to see the intensity distribution on the whole chip. This was turned off sometimes for testing purposes. Usually this was activated to reduce the amount of data that needed to be saved.
- *Bad Pixel Replacement*: For the characterization of the instrument this was turned off. For the actual measurements this was turned on.
- *Noise Suppression*: This is an implementation of a low-band-pass-filter. This was usually not used as it smoothed the spectra in a too large extent.
- *Intensity Normalization*: When a dark and a white reference picture have been recorded, the program can calculate the normalized intensity which is easily convertible into absorbance. This function was not used on a regular basis.

The spectra were exported as Matlab-Files and further processing steps happened in Matlab mostly. For establishing multivariate models Matlab was used again, or the data was parsed into the correct format to use it in SIMCA.

4.2.2 Calculation of Absorbance

The conversion of intensity on the chip to the absorbance values has been performed by

$$A_{\text{measured}} = -\log_{10}\left(\frac{I_{\text{measured}} - I_{\text{dark}}}{I_{\text{white}} - I_{\text{dark}}}\right). \tag{4.1}$$

So for the measured absorbance A_{measured} one needs the intensity on the chip I_{measured} and a reference measurement of the white background I_{white} as well as of the dark current of the chip I_{dark}.

To ensure that the errors of the actual measurement are homogeneously distributed around the mean, it is recommended to take the mean over several spectra (e.g. 1000) for the white and dark reference.

4.3 Performance of The Instrument

In the following, the spectrometer prototype was tested extensively to assure its correct functionality and extract its operating figures. The main point beside basic functionality was to assure the comparability in between the different ports of the instrument.

For testing the instrument, the Hellma Transflexion Probe was used, so the following tests also partially include the behavior of that probe. During all tests the frequency of the spectrometer was fixed at 105 Hz.

For testing purposes standard samples were used, namely a gray standard calibration kit (Avian Technologies LLC, FSS-08-02c) also including a wavelength standard (WC-PP-1920a-02c).

4.3.1 Single Channel Performance

The following tests were performed for all of the 25 channels, however, here just one channel shall be shown in detail. The other 25 channels showed equal behavior. The differences between different ports are discussed later.

White and Dark Reference

In the following Figure 4.2 intensity on chip is displayed for white background and the dark reference. The given intensity was gained by integrating the signal for 1500 μs for each spectrum. The mean of a number of 101 spectra was calculated.

The intensity of the white background depends on wavelength due to several reasons:

- The efficiency and sensitivity of the HgCdTe-detector depends on wavelength.
- Several different optical gratings are used which have their own efficiency.
- Damping of the signal inside the optical fibers.
- Fiber connections, entrance and exit slits always lead to refraction and diffraction and therefore lead to signal loss.
- The intensity curve of the light source.

The dark reference is gained with the optical path closed at the spectrometer exit and is the sum of several sources:

- *System Readout Noise*: This is caused by the electronics and should be independent of exposure time. Furthermore the largest portion is caused by signal amplification and therefore uniformly distributed over all pixels.
- *Shot Noise*: This is statistical variation of photon incidence and occurs in both, the dark signal and the white signal. The shot noise scales with the square root of the signal.
- *Dark Current*: This is a result of thermally generated electrons in the CCD-structure and is therefore highly dependent on device temperature.

However, the types of noise are not correlated and are therefore summed up as independent disturbances.

The difference between white and dark reference is now the actual valuable signal. Therefore, dynamic range and signal-to-noise ratio reflect the wavelength dependency of this signal. What has not been considered here is the occurrence of stray light. External stray light can be avoided by proper probing and illumination. Additionally back-scattering occurs at the optical components inside the spectrometer and adds an additional term to noise.

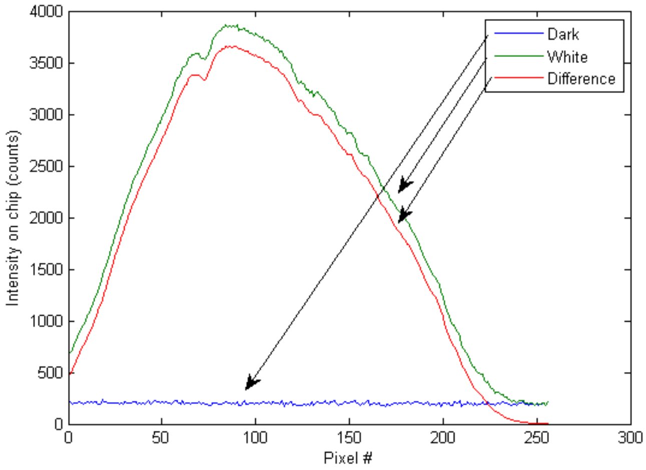

Figure 4.2: Intensity on chip for dark and white reference measurements. The valuable signal is the difference, i.e. the subtraction of the dark reference from the white reference.

For the characterization experiments the distance between probe and sample was adjusted in order to nearly reach the saturation level of the chip (which is set at 4096 counts), when measuring the white reference background to get the optimal dynamic range and signal to noise ratio.

Wavelength Mapping

For determining the wavelength mapping, the wavelength standard was measured. The reference peaks were then found in the spectra by doing a derivation (according to Savitzky-Golay with 5 points and 2nd order polynomial and finding the roots. This gives a more accurate description than just using the peak intensity directly, because by modeling the spline, peaks can also be situated at non-integer pixel numbers). Subsequently a regression was done in between the pixel number and the peaks' wavelengths. Example spectra of the wavelength standard and its derivative can be found in Figures 4.3 and 4.4.

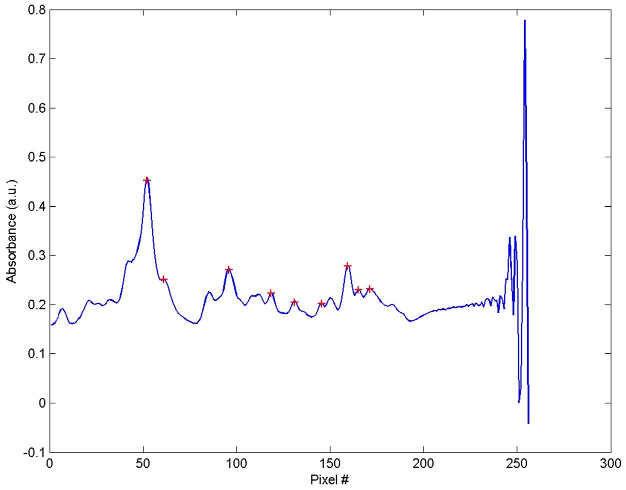

Figure 4.3: Measurement of the wavelength standard sample. The reference peaks are indicated by red crosses.

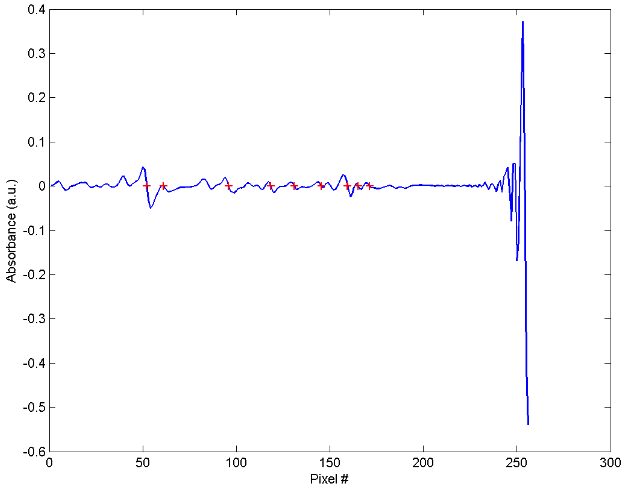

Figure 4.4: First derivative according to Savitzky-Golay of the measurement of the wavelength standard. The positions of the reference peaks (now roots in the first derivative) are indicated by red crosses.

A linear regression and a quadratic regression were tested, and the results for different ports can be seen in Table 4.2. However the quadratic term was always lower than $10^{-3}\,\mathrm{nm}/\mathrm{pixel}^2$, so this would result in difference of $10^{-3} \cdot \frac{256}{2}^2 = 16\,\mathrm{nm}$. As the maximum spectral region covered ranges roughly from 940 to 2540 nm, the difference from one pixel to the next is $\frac{1600}{256} = 6.25\,\mathrm{nm}$. Hence, the first order model differs from the second order by a maximum of 1.5 pixels, thus a first order model is satisfying. The regression lines can be seen in Figure 4.5.

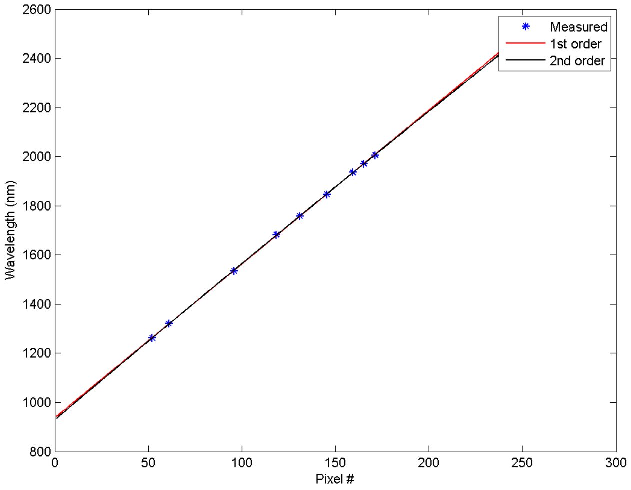

Figure 4.5: Linear and quadratic regression between wavelength and pixel position.

Furthermore the reproducibility of the wavelength mapping has to be ensured. For this purpose independent records of the wavelength standard along a time span of three weeks have been performed. Comparing the positions of the peaks one can see that the standard deviation of the peaks appearance is below 0.03 pixel in the central part of the spectral region and below 0.05 pixel in outer parts (i.e. below 1500 and above 2000 nm) of the spectral region. Hence the standard deviation for the wavelengths is in the range of 0.3 nm. As a result a once established regression for mapping wavelengths to pixel positions stays valid.

This further allows us to compare the nominal wavelength with the wavelength established by the regression model as can be seen in Table 4.1. The deviations from the nominal wavelengths are larger than the error due to reproducibility.

Additionally there is no pattern in the deviations that would be visible, if the mapping follows indeed a quadratic or an angular function. The seemingly random deviations are consistent over all tests which indicates that the wavelength mapping has different sections as a result of the different grid elements.

Nominal λ (nm)	Pixel (#)	λ by Regression (nm)	Deviation (nm)
1261.08	52.15	1263.22	-2.14
1320.40	61.07	1319.17	1.23
1535.14	95.71	1536.38	-1.24
1681.70	118.42	1678.83	2.87
1757.80	130.78	1756.37	1.43
1847.11	145.23	1846.95	0.16
1935.83	159.32	1935.36	0.47
1970.94	165.13	1971.78	-0.84
2006.53	170.98	2008.47	-1.94

Table 4.1: Nominal and reconstructed wavelengths and their difference.

To extend the investigated region beyond the region defined by the used wavelength standard an additional standard consisting of polystyrene was used. A recording of the standard with the EVK prototype system and an FT-spectrometer can be seen in Figure 4.6. Unfortunately, the peak resolution was not sharp enough to determine the exact peak positions. However, a simultaneous plotting of the polystyrene record on the scale based on the regular wavelength standard together with a reference measurement done on an FT-spectrometer shows that the peaks are at the same (and correct) position.

Optical Resolution and Instrumental Bandpass

The previous section showed that one pixel differs from the next by $\approx 6.26\,\text{nm}$, which is equivalent to the optical resolution. The second important property is the instrumental bandpass, i.e. how broad appears a peak that is infinitely small, when measured with the instrument. The broadness of the peaks depends on the used optical elements. Here we estimated this value by taking a look at all the collected spectra and see, whether two peaks next to each other could be resolved separately or not. Hence, by comparing with the natural line-width, we can give an estimation of the bandpass of 40 nm.

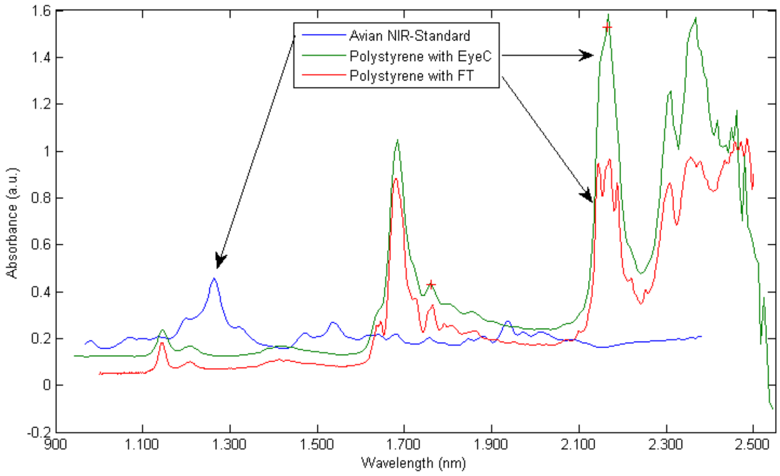

Figure 4.6: Spectra of the regular wavelength standard and the polystyrene standard recorded with the EyeC. For comparison the polystyrene standard was also recorded with an FT-spectrometer (Perkin Elmer).

Dynamic Range and Signal-to-Noise Ratio

The dynamic range of a system is the full scale signal divided by the minimum resolvable signal. As a result this gives an indication on the minimum detectable signal, and the intensity accuracy for measurements.

The dynamic range was calculated according to

$$DR = \frac{I_{\text{reference}} - I_{\text{dark}}}{s(I_{\text{dark}})}, \tag{4.2}$$

where $I_{\text{reference}}$ is either referring to the intensity, when measuring the 99 %, respectively 10 % reflectance sample, to gain the dynamic range at a low and high gain level. The s indicates the empirical standard deviation. In a similar way the signal to noise (S/N)-ratio is given by

$$S/N = \frac{I_{\text{reference}} - I_{\text{dark}}}{s(I_{\text{reference}})} \tag{4.3}$$

[45, 137, 138]. The resulting figures can be seen in Figure 4.7 and 4.8. Those were determined by taking 101 consecutive spectra with an integration time of 1500 μs into account.

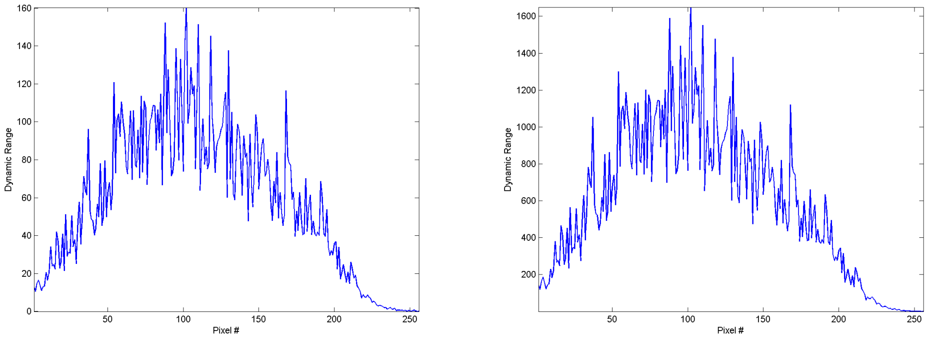

Figure 4.7: Dynamic ranges for low gain (left) and high gain (right) for 101 spectra.

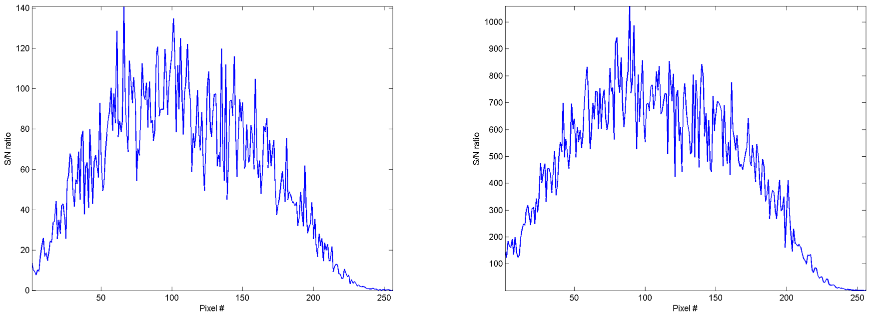

Figure 4.8: Signal to noise ratio for low gain (left) and high gain (right) for 101 spectra.

The signal to noise ratio indicates how precisely the system can measure a certain light level. It is comparable to the dynamic range, but also includes shot noise. Here the S/N ratio is given for the whole wavelength range and close to the saturation limit of the chip. Usually just the maximum value is given. By stating that the S/N ratio should be at least 100 (=20 dB), which is a commonly chosen level, the region above 2250 nm does not fulfill this criteria anymore.

Another possibility in quantifying the noise level is the Root-Mean-Square-Noise as defined by

$$RMSN = \sqrt{\frac{1}{N}\sum_{i}^{N}\left(A_i - \tilde{A}\right)^2}, \tag{4.4}$$

with N being the number of points in a spectral segment, A_i the absorbance at a point and $\tilde{A}$ the mean absorbance of a segment. A single segment covers a spectral range of 100 nm [139].

The signal to noise ratio depends on the number of spectra integrated. As the shot noise is the dominating factor, the signal to noise ratio increases with the square root of the number of integrated spectra. For testing purposes the number of integrated spectra was varied as can be seen in Figure 4.9.

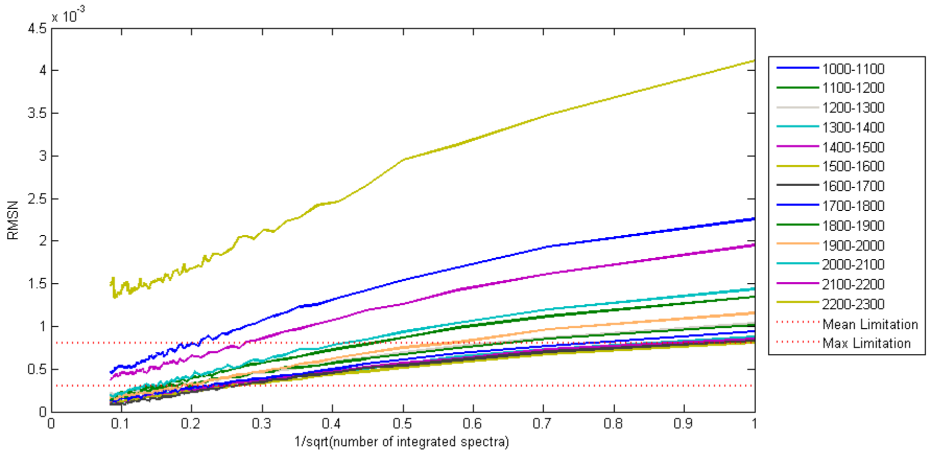

Figure 4.9: RMSN noise estimation for different spectral blocks, and for different number of spectra integrated. The noise follows roughly the expected $\propto \frac{1}{\sqrt{N}}$ behavior. The dashed lines mark recommended limits.

Linearity

The chip response should be linear, i.e. the reflectivity of a material should be proportional to the number of counts on the chip. To test this, reference specimen with different reflectivity have been measured as can be seen in Figure 4.10.

When converted to absorbance they can be compared to their nominal absorbance on an absolute scale. The measured absorbance levels are displayed in Figure 4.11 and a comparison to the nominal values is found in Figure 4.12. The expected performance is within specification. The specimen are designed to have the same reflectivity over nearly the whole range of observed wavelengths which is also reflected in the graphs. It can be seen that the measured absorbances are subject

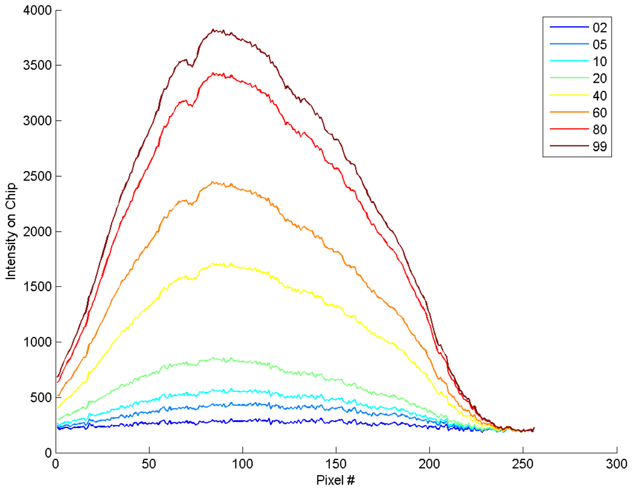

Figure 4.10: Intensity measured on chip for specimen with different reflectivity (given in %).

to change from one measurement to another which might be caused by not identical distances and surface inhomogeneity.

4.3.2 Port Comparison

First of all we compare the direct intensity that is mapped onto the chip as can be seen in Figure 4.13. The channels are well comparable. However, it is notable that the center of the chip receives a slightly better illumination than the wings. Remarkable also is the very low intensity gained by port number 21. Nevertheless, the intensity is no primary concern when comparing channels as this should be corrected by applying a white standard reference measurement anyway. In contrast the intensity on the chip gives an indication, if the dynamic range (and therefore the precision in quantifying) is effected by the position on the chip.

A second concern is the wavelength mapping. In general the mapping is well comparable between channels. In Figure 4.14 the deviation of wavelength at a certain position compared to the mean at that position is shown in a contour plot. There is a slight distortion at the edge of the chip assigned to the longer wavelengths. At a wavelength of 2250 nm there is a difference of 2 nm in the

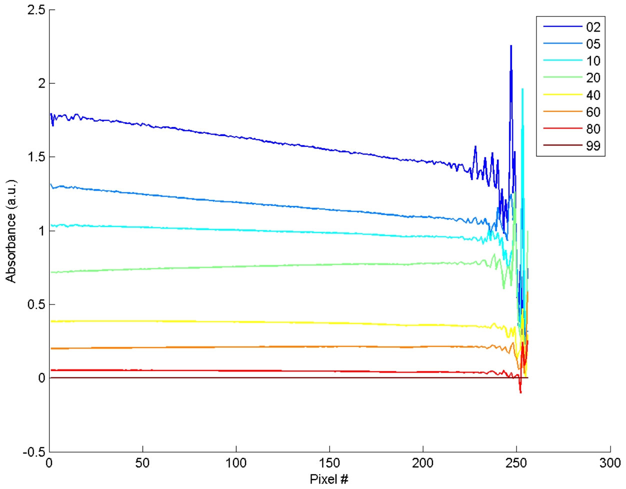

Figure 4.11: Absorbance measured, for specimen with different reflectivity (given in %). It can be seen that the samples are prepared to give the same absorbance for a large spectral region.

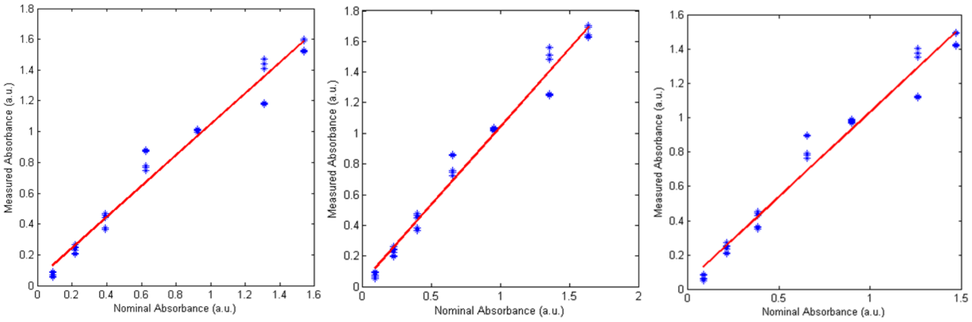

Figure 4.12: Comparison of expected and observed absorbance at three different wavelengths. Left: 1200 nm fit:$1.018x + 0.029$, Center: 1600 nm fit:$1.004x + 0.044$, Right: 2000 nm fit:$0.9927x + 0.044$.

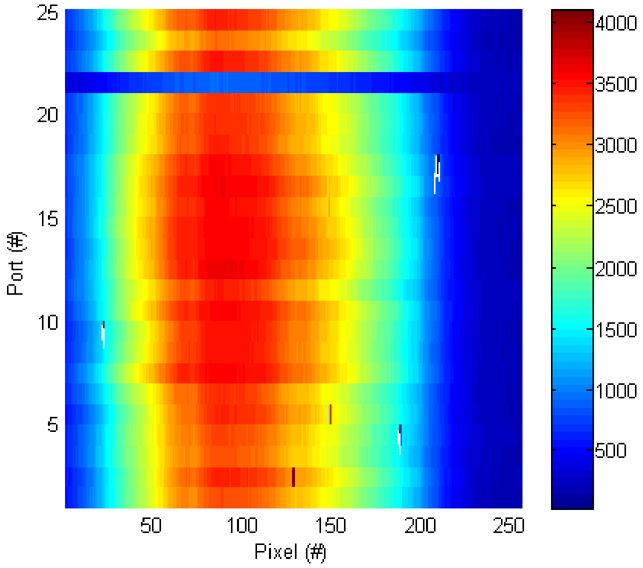

Figure 4.13: Intensity on chip measurements for the same specimen for all channels and wavelengths. The color represents the number of counts. The white artefacts are undefined values due to bad pixels.

assignment of wavelengths between ports at the edge and ports at the center of the chip. The mapping functions for all channels are summarized in Table 4.2.

Cross Influence

When using one of the ports, there is a slight influence on neighboring ports. In Figure 4.15, a pattern of different reflectance intensities was detected by a port. The port next to it shows the same, albeit very much weaker pattern. Roughly $1/300$ of the intensity of the primary port reaches the neighboring port. For the next nearest neighbor, the pattern was not detectable any more.

The intensity profile for illuminated ports, across the chip can be seen in Figure 4.16. Here the ports 3, 5, and 6 were measuring the white reference standard. The intensity represents the optical imaging of the exit slit, and therefore roughly follows a sinc-function. It can be seen that the peak trails are overlapping.

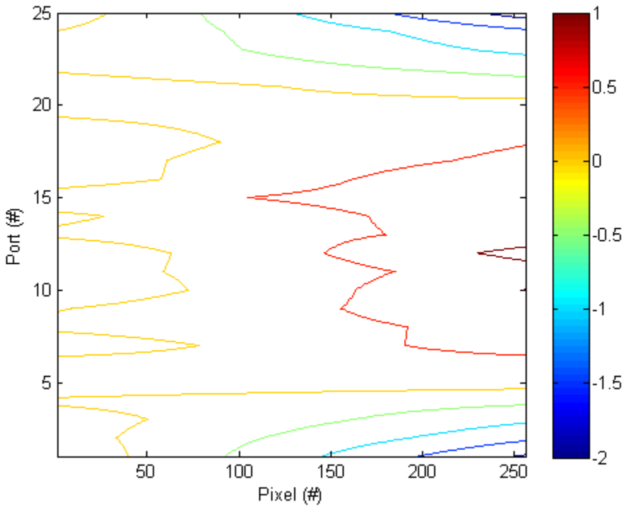

Figure 4.14: Comparison of the wavelength mapping along the chip. Shown in the graph is the deviation of mapping (in nm) compared to the mean of all channels.

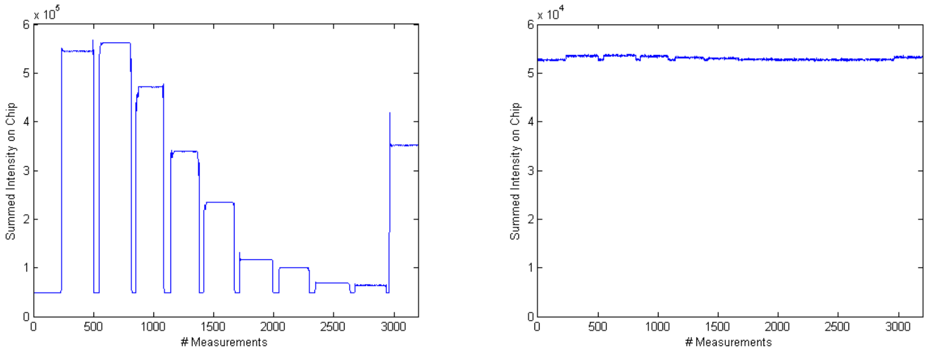

Figure 4.15: A signal pattern was detected at one port (left). The signal reproduces itself (although much weaker) on the neighbouring port (right). Note that the scale between those two pictures is a factor of 10.

Port (#)	Inclination (nm/pixel)	Interception (nm)
01	6.2604	936.6197
02	6.2637	936.4471
03	6.2655	936.4639
04	6.2687	936.1683
05	6.2695	936.5683
06	6.2700	936.4704
07	6.2744	935.8915
08	6.2719	936.3600
09	6.2733	936.2102
10	6.2754	935.8418
11	6.2739	936.0087
12	6.2759	935.8619
13	6.2723	936.3139
14	6.2734	936.1480
15	6.2721	936.5145
16	6.2747	935.9601
17	6.2731	936.0458
18	6.2728	935.9848
19	6.2714	936.1699
20	6.2701	936.3615
21	6.2678	936.5073
22	6.2676	936.1647
23	6.2659	936.1507
24	6.2644	936.2414
25	6.2600	936.5243

Table 4.2: Overview of the linear regression for mapping wavelength to pixel number, according to wavelength = interception + pixel*inclination.

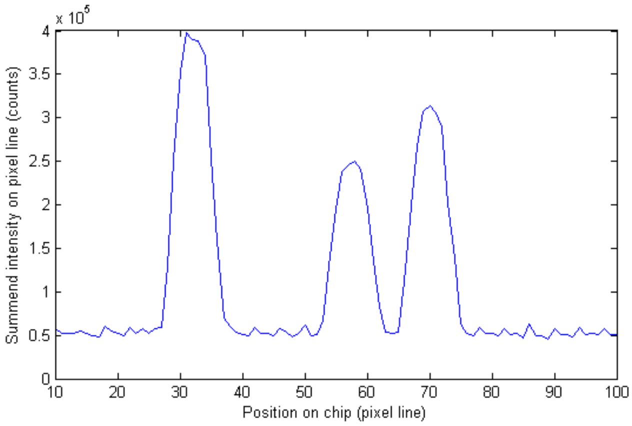

Figure 4.16: The summed intensity of the pixel lines is shown for the channels 3, 5, and 6 simultaneously. It is important to note that the signals' peak feet touch each other slightly. On a side-note: The difference in intensity here is a direct result of the different illumination intensity at the three ports of the illumination source.

4.3.3 Short and Long Term Stability

There are different time scales to consider, when talking about stability. First of all, there is the noise from one measurement to the next which was already considered in calculating the signal-to-noise-ratio. Secondly there is a drift caused by dark current. To correct for this the drift is controlled regularly. Finally the stability of the instrument has to be assured for longer time periods, namely the time a process lasts which the system is measuring. More precisely, this is from one possibility of applying a white reference to the next. Finally, recorded spectra should be valid for many years. This is assured by the non-changing wavelength mapping.

Dark Current Correction Interval

For now the correction of the dark current happens regularly at a 5 minute interval. A shutter is closed and a dark reference spectra is collected which then evokes a complex function, to keep the dark current in check.

How the drift of the dark current can look like can be seen in Figure 4.17. The interesting question is now, if the correction interval is chosen correctly.

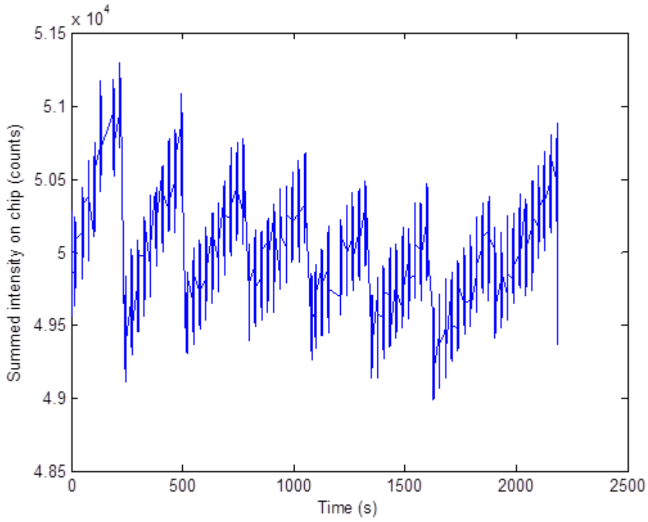

Figure 4.17: Counts for dark current (mean across all wavelengths) over time. The five minute interval of the dark correction is clearly visible as well as the changes from one spectrum to the next. The smaller gaps are due to pauses in the measurement.

To answer this question we take a look at the fluctuations which appear from one spectra to the next anyway, and at the drift of the dark current. To estimate the drift a time interval from a longer measurement series was chosen, where drift is most prominent, in order to give an estimation of the maximum drift that might appear. In Figure 4.18 the standard deviation of the first 50 and the last 50 spectra of of a correction interval is displayed. The gap in between is a result of the dark current drift.

The standard deviation between spectra is then compared to the dynamic range. The same is done within blocks of spectra at the beginning and end of a dark current correction interval as to estimate the dark current drift. The resulting figure can be seen in Figure 4.19 and gives a description which fraction of the acquired spectra is determined by the dark current.

Within the assumption that the drift of the dark current is linear (which is roughly true for the short interval in between two automatic corrections as we can see in Figure 4.17), we can estimate the ratio of the dark current for the given interval in comparison to the dynamic range. Over the whole spectral region the error induced by drift is roughly 2-3 times the minimum error one can achieve which

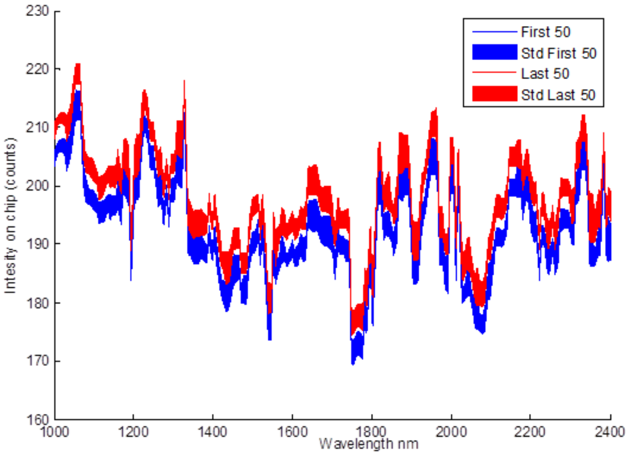

Figure 4.18: Plotting the mean and standard deviation of the first and last 50 spectra of a dark current correction interval.

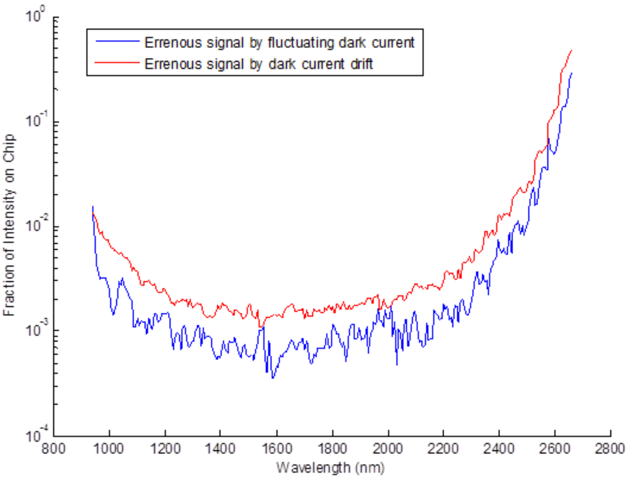

Figure 4.19: Fraction of signal caused by dark current. For relevant wavelengths the fraction is below 1%. However, this is only true for the best signal (i.e. if the full dynamic range is used).

is given by the shot noise.

Long Term Stability

A test for 100 hours has been performed for long term stability which is depicted in Figure 4.20.

Obviously there is a certain warm-up time until the instrument reaches a steady state. It is therefore strongly recommended to wait 30 min after the activation of the instrument until the instrument is stabilized before measuring references and starting the actual measurements.

After the warm-up phase the instrument is stable and does not show any systematic drift. There are smaller deviations of around 0.1 absorbance units, which can have several reasons. However, as there is no overall drift a correctly performed white reference measurement done at the beginning (and after the warm-up phase) should stay valid for the observed time period.

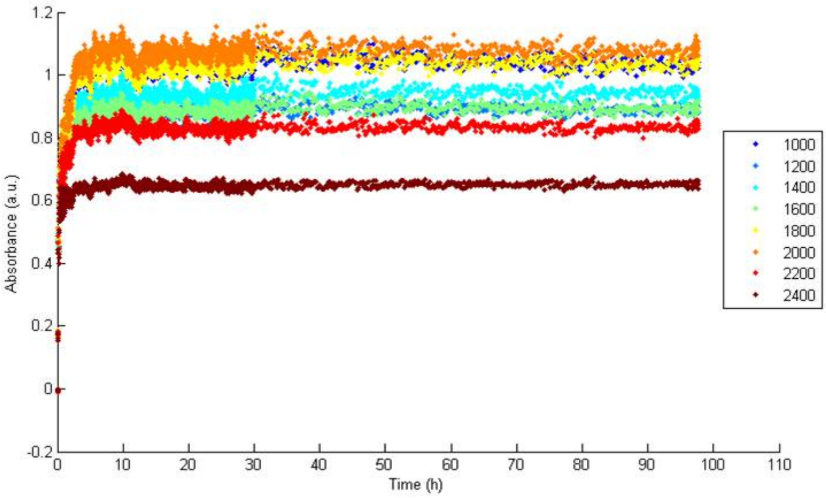

Figure 4.20: Long term drift of the baseline for several wavelenghts. There is a certain warm-up phase, but afterwards the instrument is stable. For this set-up a temperature stabilized lamp was used.

4.3.4 Effect of Integration Time

Integration time has an effect on the measured signal and on the dark current. Both values grow linearly with time as can be seen in Figure 4.21 until the saturation limit of the chip is reached.

A larger dark current itself does not effect the quality of the signal as the fluctuations in the dark current are practically still the same. One should therefore always strive for the maximum dynamic range and signal to noise ratio but avoid over-saturation even for unexpected occurrences. How both numbers change with integration time for the test setup is shown in Figure 4.22.

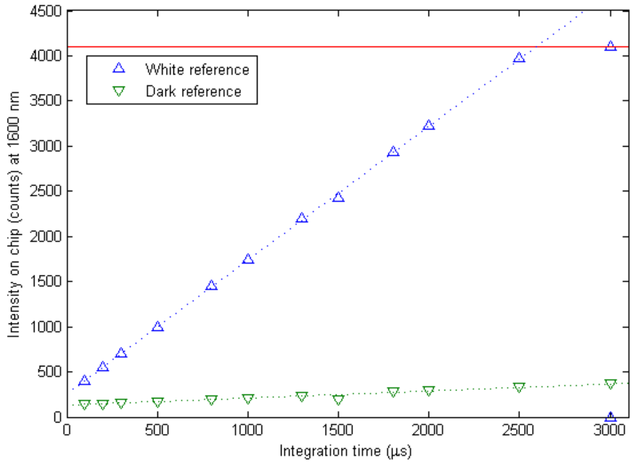

Figure 4.21: Intensity on chip when measuring dark current (green) and white background reflectance (blue). Both follow a linear relationship as indicated by the fit lines. The red line indicates the saturation level of the chip.

4.3.5 Binning

To increase the signal quality it might be possible to not just use one line, but to sum up several lines on the chip next to each other. This has been done and the resulting SNR and dynamic range can be seen in Figure 4.23. The figures are a result of 50 consecutive spectra. Obviously both values increase until the weak signal intensity (compare Figure 4.16) inverts this trend.

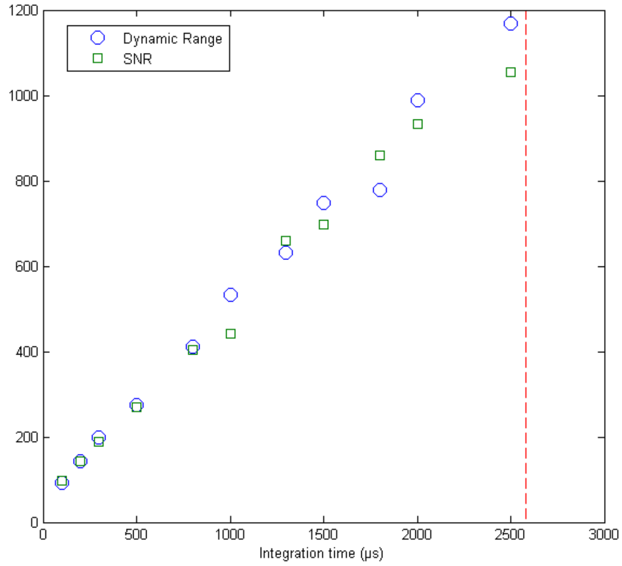

Figure 4.22: Dynamic range and signal to noise ratio in the current setup. The red line indicates the chip saturation limit. Although the integration time increases the dark current, the signal to noise ratio rises until the saturation limit.

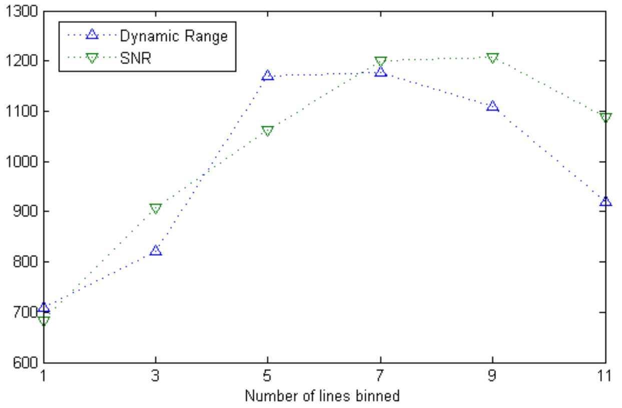

Figure 4.23: Dynamic range and signal to noise ration for a different amount of lines binned. The binning always happens symmetrically from the center line.

4.3.6 Comparison of Different Probes

Thanks to the standardized SMA905 ports a variety of probes can be attached to the spectrometer. Simple reflection probes by OceanOptics, a diffuse reflection probe by Hellma and an NIR-probing gun by Perkin Elmer have been tested in the now mentioned case. It can be seen in Figure 4.24 that the signal dependens on the probe quality. Nonetheless, the spectrometer works with every probe and the spectra are comparable, albeit not in absolute intensity.

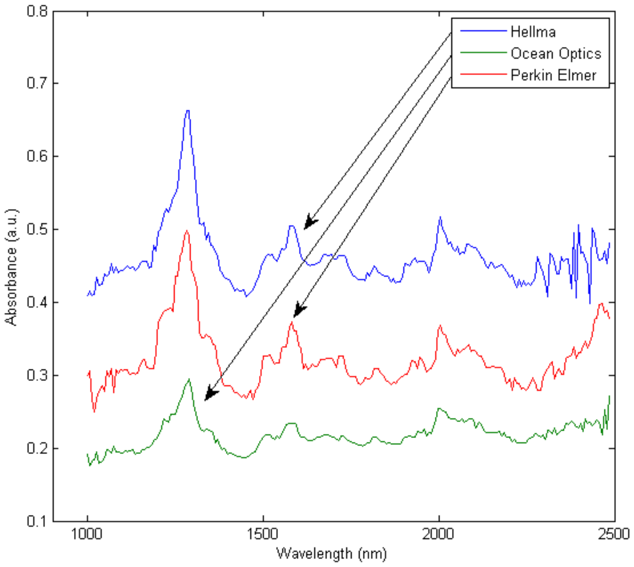

Figure 4.24: The same sample was monitored with three different probes. The different absolute intensities are a result of not identical distances and illumination of the samples.

When establishing a multivariate model the probe can be added as another qualitative variable. Hence it is possible to estimate the influence of the probe on the spectra. However, the resulting importance is based on the spectrometer port differences as well as on the probe differences, although those are nominal the same. It turns out for several cases that the correction factors for the port are negligible and chemometrical models can be carried from one port to another without consequences. Further when looking for characteristics of certain ports compared to others just random noise is found. In Figure 4.25 the coefficient plot of a partial least squares discriminate analysis classifying the different ports is shown which shows that the differences are statistical noise and concentrated at longer wavelengths (where there is a smaller signal to noise ratio). This is actually not unexpected as this just supports, what the previous characterization of the instrument has shown.

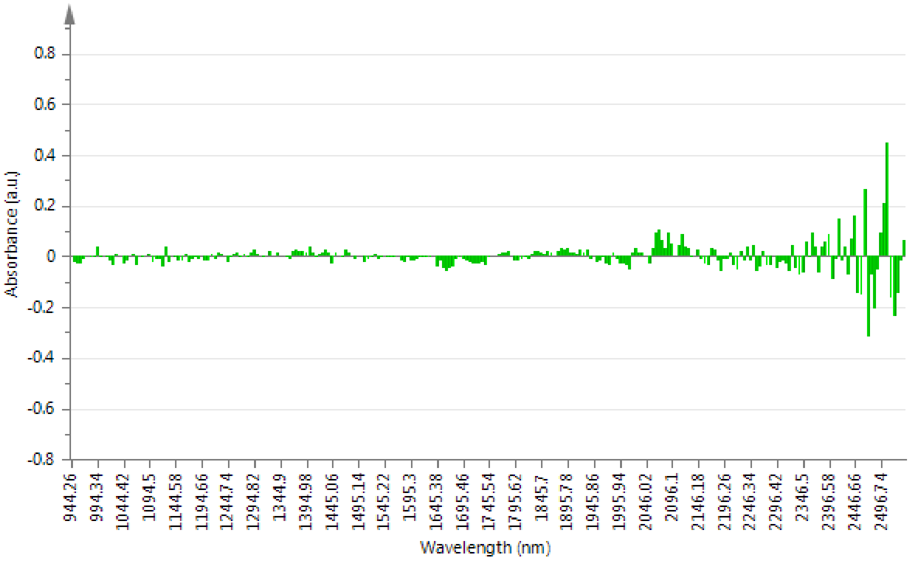

Figure 4.25: Differences for port 1 compared to the ports 2 and 3. The differences are basically statistical noise. Larger differences appear for longer wavelengths, where the signal to noise ratio is worse.

4.3.7 Conclusion

The direct comparison showed that the equivalency of different channels is given in principal. Still there are issues to consider. For example the channels differ marginally in performance and are not completely congruent in their wavelength distribution. Ports which are projected to the center of the chip show a slightly better performance (in terms of signal to noise ratio and dynamic range).

4.4 Test of Equivalency with Multivariate Methods

4.4.1 Expanded Factor Set

As described in Section 2.3, a common method for investigation of spectra and chemometric model building is principal component analysis (PCA) and projection to latent space (PLS). The latent space is created by linear combinations of the original variables (i.e. wavelengths). The regression coefficients of the PLS represent the weighted sum of the latent variables, enabling the prediction of the target variable by multiplication with a corresponding spectrum [102].

It is also possible to add qualitative variables (i.e. describing the occurrence of a property, as opposed to quantitative variables describing the value of a property), and to expand the variable space by taking interaction terms of variables into account. Such coefficients of expanded variables describe, how the effect of one variable changes with another. However, one has to keep in mind that expanding leads to an enlarged amount of coefficients, and hence even more measurements are needed to make reliable assumptions of those coefficients and avoid overfitting [140].

The mentioned possibilities of PCA and PLS were selected for testing the equivalency of measurements by building several models.

1. A classical model, establishing the correlation between measurements and a target value.
2. Incorporating the port as model term, to test for significance.
    a) Representing the port as a qualitative variable does not enlarge the computational difficulty of model building and allows estimating if a constant offset is induced by the port.
    b) However, the port influence is likely a multiplicative factor. Hence adding the interaction terms of (wavelength*port) for the analysis may reveal specifically which spectral regions are interpreted unique for every port.

Hence coefficients are gained for the base terms (as in the classical model), three base coefficients for the three ports, as well as a set of crossed coefficients for every port. Of the latter, the coefficients for just one port are shown in the Figures 4.27 and 4.29 for simplicity.

Two data sets have been used here. First, the already mentioned reference gray standards. For those tests the measurement set-up was left untouched, except switching the detection fiber between the measurement ports. This was done in a way that the equivalency of measurements was guaranteed, and only the effects of the spectrometer itself were seen.

The second data set was gained by the application of the instrument to a pilot-scale pharmaceutical process. A hot-melt-coating process was observed with three identical probes, but at different height levels inside the fluidized bed vessel. The target variable of the established chemometric model is the batch maturity which is proportional to particle size and coating thickness. The increasing coating, and hence maturity, was monitored for roughly 50 minutes. There is a large chance that deviations between different ports appear, caused by different measurement positions, sample presentation, process inhomogeneities, and much more.

4.4.2 The Ideal Test Case

First the results obtained by the gray-level standards shall be discussed. No spectral pretreatment was used. A simple PCA shows that the reflectivity of the measured materials is indeed the largest influence factor and covers 99.7% of the data. The according graphs are found in Figure 4.26. However, taking a look at the second principal component exhibits the differences of the measurement ports, explaining 0.1% of the data. Indeed it would be sufficient to build a PLS model with just one component to have a proper model estimating the reflectivity of the samples as seen in Table 4.3.

The question arises if the model can be improved by implementing the knowledge which measurement port was used. This has far-reaching consequences, as this would mean that the measurement port has an influence on the model, and that the models ought not to be the same for different measurement ports.

Hence additional PLS models were built, one including the port as a simple qualitative variable, i.e. every port is corrected for a constant. A second model then additionally includes the crossed terms of wavelength and port, hence if sensitivity is different for certain wavelengths and a multiplicative factor should be added that should be seen in the latter model.

The observed PLS coefficients, as shown in Figure 4.27 shall now be discussed. The coefficients for the wavelength show all approximately the same value. This is expected, as standards were measured that theoretically have the same reflectivity for the whole observed region and they all show the same proportional behavior. The error bars, representing a 95% confidence interval, indicate that all of them are significant. On a side note, the error bars also reflect the signal-to-noise ratio of the spectrometer which is best around 1500 nm, where the smallest error bars are found, and decreasing towards the edges of the spectrum indicated by the growing error bars.

The coefficients for the ports are nearly zero and vastly excelled by their error bars indicating the non-significance of the port, and that a simple additional term does not improve the model. Finally looking at the crossed terms, the same behavior can be seen. Therefore, equality of all ports is proven for this measurement. As the experimental conditions and samples have been carefully chosen, it can be concluded that the used spectrometer indeed has equivalent properties at each port, and that models can be transferred from one port to another.

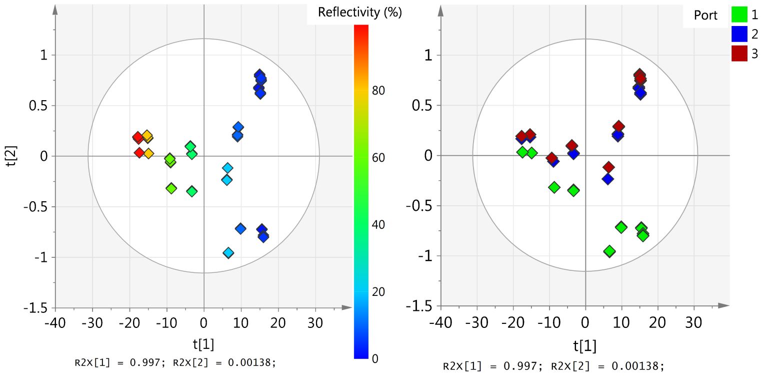

Figure 4.26: Model building on gray standard measurements. PCA scores plot of the measurements. On the left, the markers are colored according to their reflectivity; on the right the markers are colored according to the port. Both show clear distinctions with the principal components.

4.4.3 The Non-Ideal Case

In addition to the lab-scale pharmaceutical process, a process exhibiting unsteady and difficult experimental conditions was investigated. Now the same methodology than before was applied for checking the equivalency of the ports.

Due to the fact that distances to the measured particles in the fluid bed were not

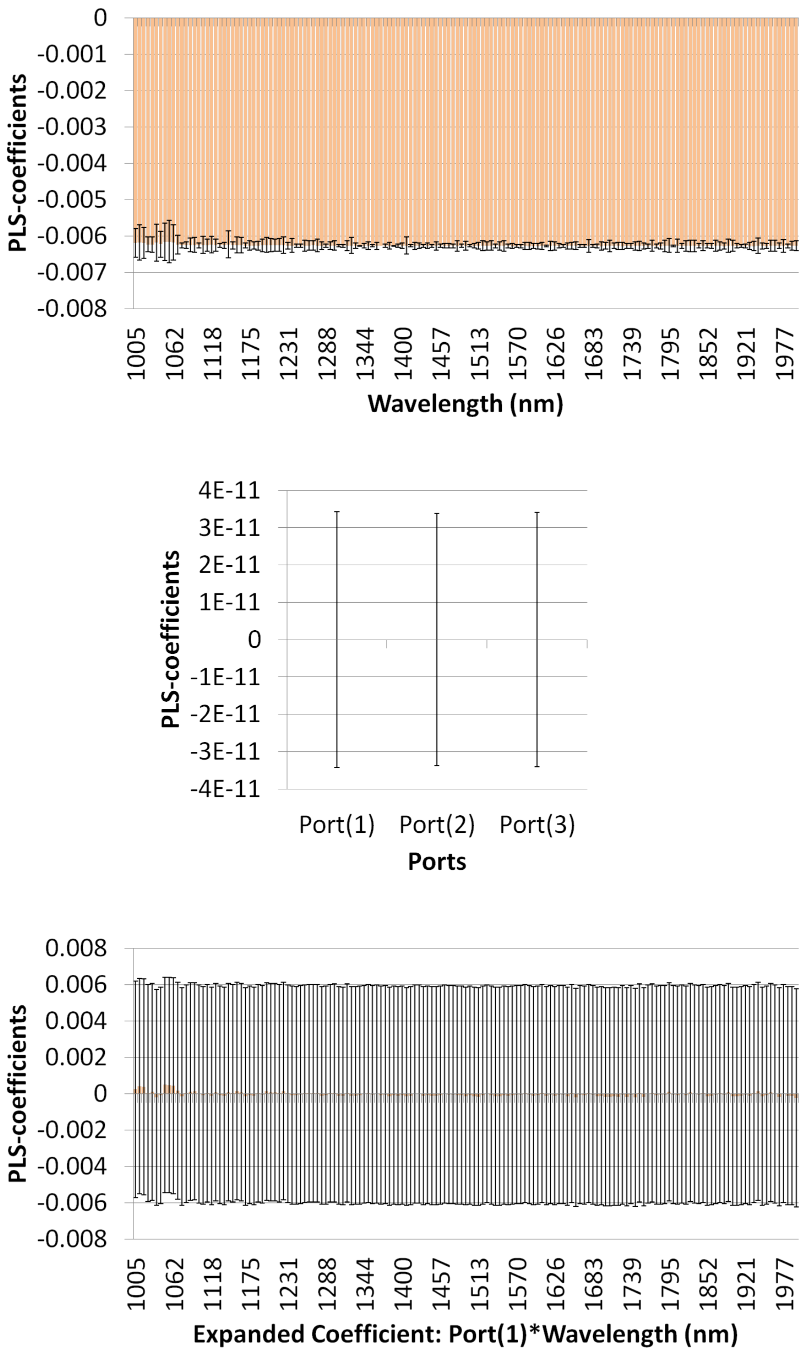

Figure 4.27: Model building on gray standard measurements. The PLS-regression coefficients are shown for the absorbance values (top), port variables (middle) and interaction variables (bottom). Only absorbance values have an significant influence on the prediction of the sample reflectivity.

No.	Description	A	R^2X	R^2Y	Q^2 (refl.)	Q^2 (port)
1	spectra → reflectivity	1	0.997	0.967	0.954	0.967
2	spectra + port → reflectivity	1	0.979	0.967	0.954	0.967
3	spectra*port → reflectivity	1	0.249	0.966	0.952	-0.1

Table 4.3: Statistics on the created PLS-models with gray standards, for 1) a usual correlation of spectra as predictor variables and reflectivity as dependent variable 2) with port as additional qualitative predictor variable 3) with the cross terms of wavelengths and port as predictor variables; The number of PLS components is given by A; R^2X and $R^2 2Y$ are the explained variance of X and Y data, respectively. The Q^2 values were gained by Cross-Validation, grouping was done according to reflectivity or port. The Q^2 of model 3 is negative, because no proper cross validation is possible, as every group represents one discrete value of the qualitative port variable.

always the same, SNV was chosen as a pre-treatment. As shown in Figure 4.28 , the PCA nicely distinguishes between maturity at the first component, explaining 58% of the data, and the different measurement positions in the second principal component, explaining 20% of the data.

The PLS coefficients regarding the wavelengths are a superposition of the substrate and coating spectra, reflecting the growth of coating and masking of the substrate particle material.

Adding coefficients representing the port, they show a difference in the mean values of maturity, but no significance is given to these coefficients as there is no valid overall offset across all the time.

Finally crossed terms of port and spectra were added. This enables the PLS model to basically represent every port independent of the others. The coefficients hence refer to the overall trend in the data (for the base terms) and the differences in between ports (for the crossed terms). Most of the crossed coefficients are not significant and represent statistical noise, as shown in Figure 4.29. Nonetheless there are some wavelengths considered significant, especially a spectral block in the region of 1450-1530 nm.

Blindly excluding this spectral block would result in a slightly better model, as is indicated in Table 4.4. However, there needs to be some physical reasoning for explaining the deviation. By comparison to offline samples, we came to the conclusion that this might likely be an excess of coating in front of the probe, and hence was not removed in the final model. Opposed to that, it is aimed for a mechanical way to overcome the deposition of coating in front of the probe.

Finally, the same model for all ports, just built on base terms, is preferred. The introduction of expanded terms easily introduces overfitting as indicated in Table 4.4 and should therefore just be used for diagnostic reasons, as presented here. A further strategy would be to choose proper pretreatments in order to overlap the different ports in the PCA scores plot.

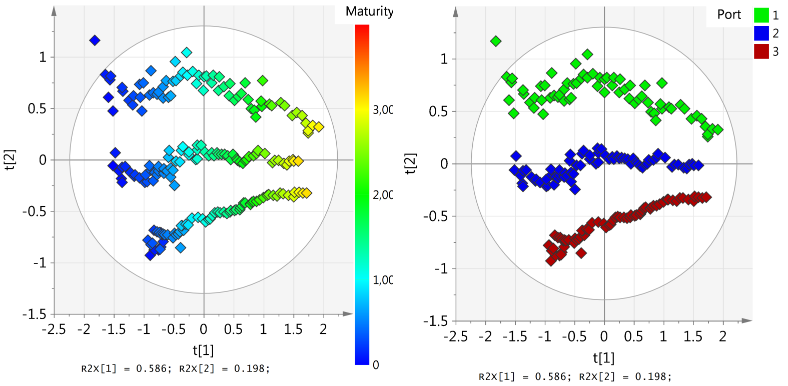

Figure 4.28: Model building on a coating process in a fluid bed. PCA scores plot of the measurements. On the left, the markers are colored according to their reflectivity; on the right the markers are colored according to maturity. Both show clear distinctions with the principal components.

4.5 Example Applications

4.5.1 Self Correction and Calibration

One advantage of a multipoint measurement system is that some of the ports can be used to either correct the measurement system itself or to be kept as a reference sample. This way, e.g. temperature drift or aging of a sample can be measured and corrected on-line.

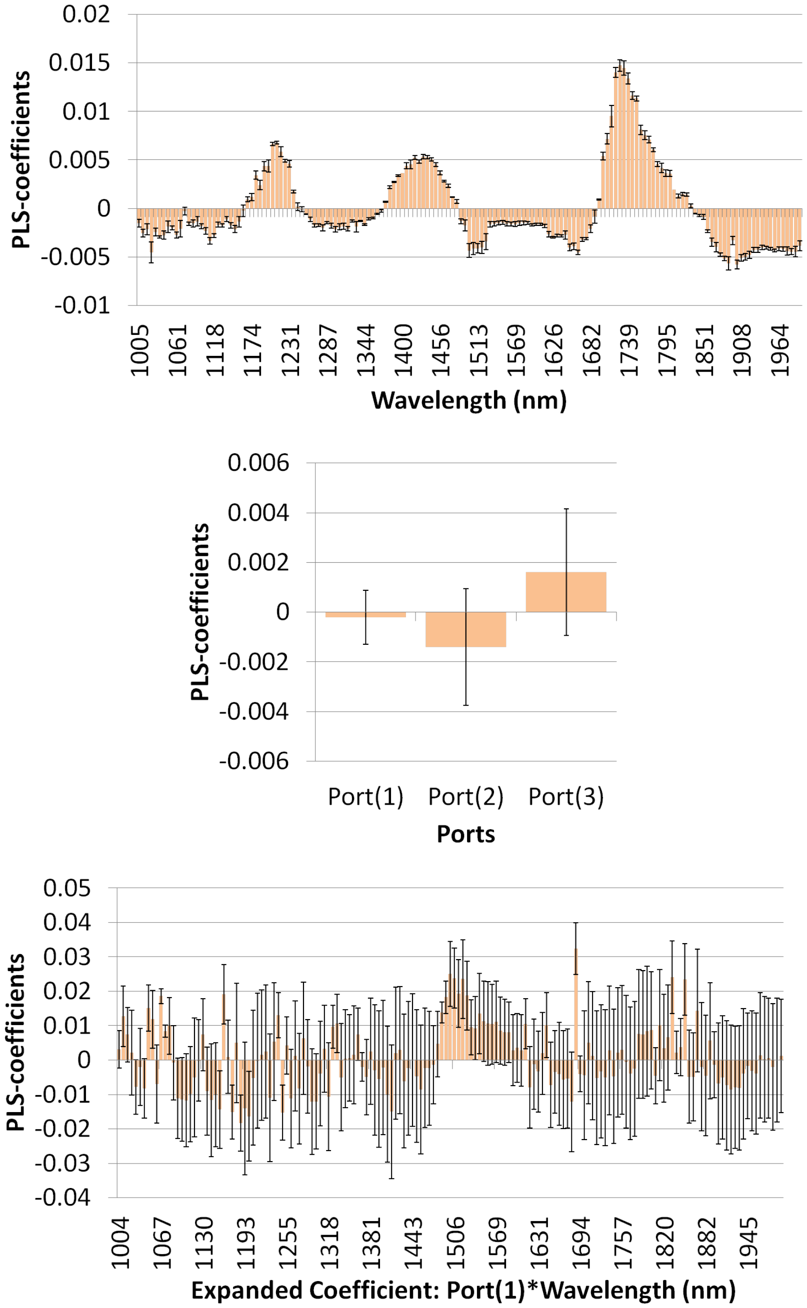

Figure 4.29: Model building on a coating process in a fluid bed. The PLS-regression coefficients are shown for the absorbance values (top), port variables (middle) and interaction variables (bottom). Note the significant region between 1450-1530 nm for the interaction variables, showing a difference between ports.

No.	Description	A	R²X	R²Y	Q² (refl.)	Q² (port)
1	spectra → maturity	2	0.755	0.983	0.971	0.967
2	spectra + port → maturity	2	0.572	0.978	0.966	0.962
3	spectra*port → maturity	2	0.327	0.806	0.706	-0.21
4	like no. 3, restricted range	2	0.341	0.813	0.708	-0.21

Table 4.4: Statistics on the created PLS-models on maturity, for 1) a usual correlation of spectra as predictor variables and maturity as dependent variable 2) with port as additional qualitative predictor variable 3) with the cross terms of wavelengths and port as predictor variables 4) with the spectral block 1450-1530 nm excluded; The number of PLS components is given by A; R^2X and R^2Y are the explained variance of X and Y data, respectively. The Q^2 values were gained by Cross-Validation, grouping was done according to reflectivity or port. The Q^2 of model 3 and 4 are negative, because no proper cross validation is possible, as every group represents one discrete value of the qualitative port variable.

Correction of Lamp Fluctuations

Here a simple set-up is used, where the illumination is constantly measured by one of the probes, and changes in the illumination of the sample are corrected for in the measured spectra.

The calculation of absorbance is shown in Equation 4.1, and the reference measurements, directed straight at the illumination source or at a reference sample, give the intensity $J(t)$. Beforehand a reference intensity $J(0)$ and the dark current of this probe J_{dark} where measured. Hence, when the illumination changes, the effective intensity measured at the sample $I_{\text{measured}}(t) - I_{\text{dark}}$ varies by a factor. This is the same factor as for the reference probe which now detects $J(t) - J_{\text{dark}}$ instead of $J(0) - J_{\text{dark}}$ before. Thus, one has to divide by this fraction to regain the the signal as it would be under constant illumination conditions and $A_{\text{corr}}(t)$ is

$$A_{\text{corr}}(t) = -\log_{10}\left(\frac{I_{\text{measured}}(t) - I_{\text{dark}}}{I_{\text{white}} - I_{\text{dark}}} \cdot \frac{J(0) - J_{\text{dark}}}{J(t) - J_{\text{dark}}}\right) = \tag{4.5}$$

$$A_{\text{corr}}(t) = A_{\text{measured}}(t) + \log_{10}\left(\frac{J(t) - J_{\text{dark}}}{J(0) - J_{\text{dark}}}\right). \tag{4.6}$$

Nonetheless, as two measurements are involved the corrected absorbance has its noise enlarged by a factor of $\sqrt{2}$. The standard deviations at individual ports σ_{port_i}

are assumed to be the same, and hence the standard deviation of the corrected values σ_{corr} can be assumed to be

$$\sigma_{\text{corr}} = \sqrt{\sigma^2_{\text{port}_i} + \sigma^2_{\text{port}_j}} \approx \sqrt{2} \cdot \sigma_{\text{port}_i}. \tag{4.7}$$

To avoid that short-time fluctuations are enlarged by this effect, it is recommended that the background of the reference and the actual measurement are taken synchronously, and that the mean over a rather long time span is used.

An example application, where the influence of a changing illumination source was corrected, can be seen in Figure 4.30.

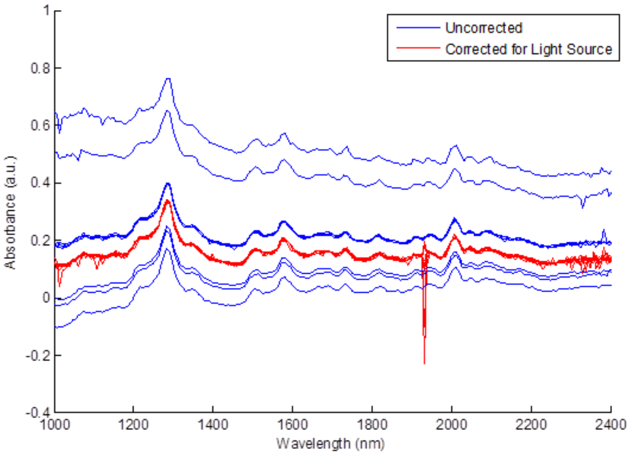

Figure 4.30: Acquired spectra are shown in blue. The lamp setting has changed and therefore the spectra have a different appearance. Spectra corrected with the reference measurement at the lamp are shown in red. The sharp spike is a result of a bad pixel in the reference spectra.

5 Experiments and Results

5.1 Calibration On The Rotating Disk

Before measurements were performed in an actual blending process, a simplified set-up, to study the emerging effects, was used.

A rotating disk was used to mimic the behavior of a moving powder bed. The probes were placed hovering roughly 1 mm above the powder bed, without touching it. This is necessary, as for a static powder bed, the sample size is too small, to extract any meaningful information. With this set-up, the geometry was well described, and the sample size could be estimated, as the detection spot, penetration depth, and speed of the turntable were known.

For model substances blends of acetylic salicylic acid (ASA) and lactose monohydrate (LM) were used, as presented in section 3.6.

The set-up allowed to study several effects. Especially the influence of the observed volume, and the effect of different spectral treatments were of interest. Focus was put on the determination of the measured homogeneity, and its relation to the mentioned factors.

First of all, for the theoretical investigation of homogeneity, the particle and sample volume has to be determined.

5.1.1 Accurate Estimation of The Particle Volume

According to the assumptions of stochastic mixing, only the larger particle species in a binary blend is of interest. As the condition, that the smaller particle species can fill up voids between particles of the larger species is fulfilled, according to $x_{50,ASA} > \sqrt{2}x_{50,LM}$, only the larger particle species (ASA) is of importance. Its size was determined by QicPic measurement, and the result can be seen in Figure 5.1.

The first crude approximation of the particle volume is given by

$$V_A = \frac{4}{3}\frac{\mathrm{VMD}^3}{2}\pi = \frac{\pi}{6}\mathrm{VMD}^3 = 4 \cdot 10^{-10}\mathrm{m}^3, \tag{5.1}$$

with VMD being the volume mean diameter. However, the determination of the VMD is based on EQPC, hence just strictly true for spheres. In contrast, ASA particles are needle shaped, hence a correction factor has to be applied.

Therefore, the measured particle distribution is modeled by a logarithmic normal distribution, whose parameters are different size fractions $x_{r,\%}$. The x denotes the equivalent diameter, r the kind of distribution ($r = 0$ represents a number distribution, $r = 3$ represents a volume distribution), and % the relative fraction. Hence, $x_{3,50}$ denotes the diameter, where 50% of the mass is contained in particles with a smaller diameter than said diameter. Those size fractions where determined experimentally and put into the model equation (according to ISO 9276-5)

$$q_r(x) = \frac{1}{\frac{1}{2}\ln\left(\frac{x_{r,84}}{x_{r,16}}\right)\sqrt{2\pi}}\frac{1}{x}\exp\left(-\frac{1}{2}\left(\frac{\ln\left(\frac{x}{x_{r,50}}\right)}{\frac{1}{2}\ln\left(\frac{x_{r,84}}{x_{r,16}}\right)}\right)^2\right). \tag{5.2}$$

A comparison between the measured and the modeled data can also be found in Figure 5.1.

Thus, the mean volume of a particle would be given by

$$V_A = \frac{\pi}{6}\int_0^\infty x^3 q_3(x)\mathrm{d}x = \frac{\pi}{6}\exp\left(\frac{9}{2}\left(\frac{1}{2}\ln\left(\frac{x_{3,84}}{x_{3,16}}\right)\right)^2\right)x_{3,50}^3, \tag{5.3}$$

still under the assumption that the particles are spheres. Assuming now a needle shape, as shown in Figure 5.2, where a cylinder with length $3d$ is cupped by two half spheres, a new *form factor* can be calculated.

As the QicPic uses EQPC (diameter of a circle of equal projection area) to determine the particle size, we can establish a relation between the diameter x obtained by the QicPic and the size d defining our needle shaped crystals. It holds for smooth and convex particles that in random orientation $1/4$ of their

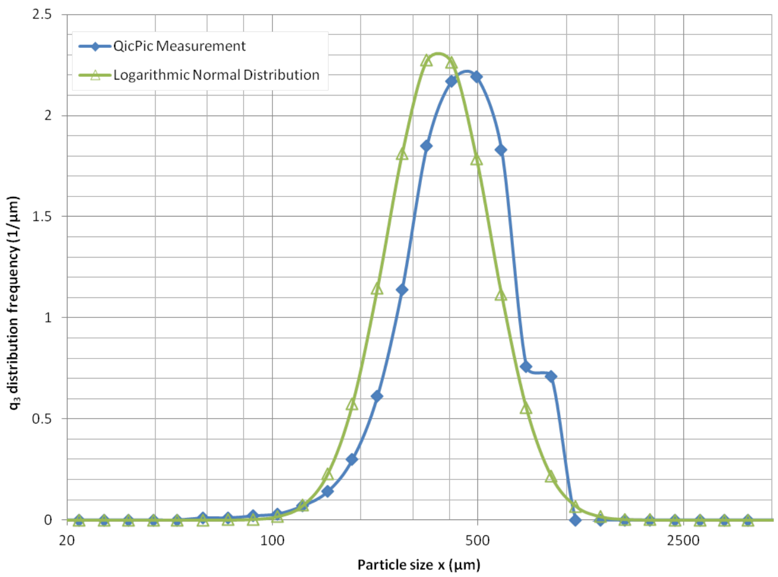

Figure 5.1: Comparison of measured and modeled size distribution of ASA crystals.

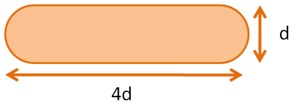

Figure 5.2: Assumed shape of ASA crystals as cylinders cupped with halph spheres.

surface is projected [141], leading to

$$O_{\text{ASA}} = 2\left(\frac{1}{2}\pi d^2\right) + 3d \cdot d\pi = 4\pi d^2 \tag{5.4}$$

$$\frac{1}{4}O_{\text{ASA}} = \pi d^2 = \frac{1}{4}O_{\text{circle}} = \frac{1}{4}\pi x^2 \tag{5.5}$$

$$x = 2d \tag{5.6}$$

and using this relation to calculate the volume again

$$V_{ASA} = 2\left(\frac{1}{2}\frac{\pi}{6}d^3\right) + \frac{1}{4}d^2\pi \cdot 3d = \frac{11}{12}\pi d^3 \tag{5.7}$$

$$= \frac{11}{12}\pi\left(\frac{1}{2}x\right)^3 = \frac{11}{96}\pi x^3 \approx \frac{\pi}{8}x^3 \tag{5.8}$$

revealing a form factor for the assumed ASA crystal shape of $\frac{\pi}{8}$ (instead of $\frac{\pi}{6}$ for a perfect sphere), which can be plugged into Equation 5.3 again. This finally leads to an estimated mean particle volume of

$$V_{ASA} = \frac{\pi}{8}\int_0^\infty x^3 q_3(x)\mathrm{d}x = 6.6 \cdot 10^{-11}\mathrm{m}^3. \tag{5.9}$$

5.1.2 Determination of Sample Volume

The sample volume, i.e. the volume which is scanned during the integration time (i.e. recording time of one spectra) and accumulation (i.e. the mean of several consecutive spectra), as sketched in 5.3, can be determined by

$$V_S = p \cdot 2\pi r \cdot d \cdot t \cdot s \cdot \tau. \tag{5.10}$$

p is the penetration depth and shall be discussed in a separate section, however 0.5 mm is a good approximation for now. r is the distance to the center of the rotating disk, hence defining the circumference of the scanned area.

The detection spot diameter d is determined by the fiber diameter. This diameter is 600 μm. Although every optical fiber has a certain aperture, this is neglected here, as it is very small compared to the effect of scattering in the sample. The time required for acquiring one spectrum τ, with a resolution of 8 cm^{-1} is 0.35 s.

The parameters which were alterable in the given set-up were the number of accumulated spectra t and the speed of the rotating disk s. The number of integrated spectra should be above 8 to give a reasonable signal to noise ratio, even in the static case, hence it was varied from 8 to 16. The different rotational speeds of the turning table were 0.34, 0.55 and 0.77 rpm.

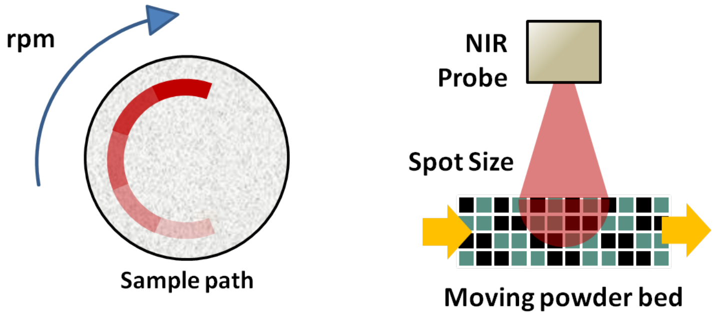

Figure 5.3: Sketch of the sampling on the rotating disk. A certain amount of powder passes through the probed volume.

Expected Fluctuations in Concentration

When accepting the penetration depth which will be determined in the next section, and referring to Equation 2.50 the volume needed for a certain accuracy in prediction can be calculated. Or in reverse, the fluctuations in concentration to be expected can be calculated with the sample size known. This is shown in Figure 5.4.

Effects of Sampling and Pretreatments on Variance

Now variances shall be calculated on the raw spectra, to illustrate the influence of chemometric pretreatments on the obtained variance. The first thing done however is the selection of the spectral range from 7226 - 4570 cm^{-1}, as a representative region for the two used substances ASA and LM. Variance was always calculated for one wavelength across spectra, and then the mean over all wavelengths was used. A multiple linear regression was then used, to determine the potential influential factors on the variance.

For unpretreated spectra the results are shown in Figures 5.5 and 5.6. The number of accumulated spectra, as well as the concentration show a strong influence. Furthermore the obtained variance is different from probe to probe. This is not that surprising, as the different probes do not have the exactly same distance to the powder bed. A change in distance results in a change of recorded intensity, and hence a change in variance. More interesting is the nearly linear increase of variance with increasing concentration. This is most likely caused by the change

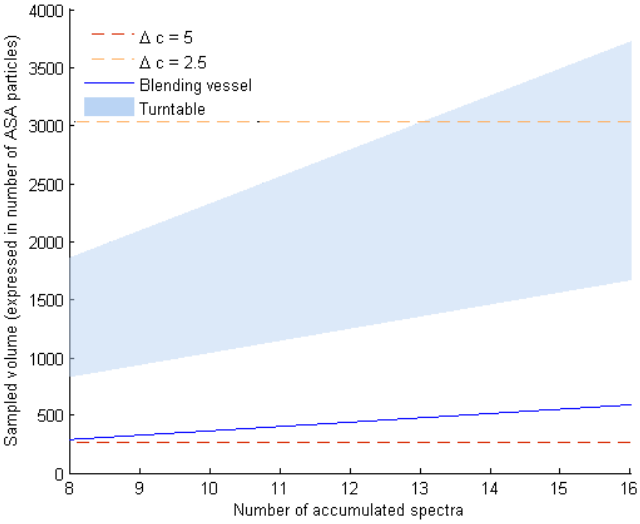

Figure 5.4: Relation of scanned volume and achievable concentration accuracy Δc, for concentration $c = 0.5$. The area marks the region achievable with different turntable speeds, whereas the line represents the conditions in the latter blending setup.

of texture, and hence scattering behavior, of the binary blend. The change of intensity level due to different scattering dominates over the change in variance due to compositional heterogeneity in this case.

For SNV-pretreated spectra, this already changes, as can be seen in Figures 5.7 and 5.8. A curvature can be seen for the variance with concentration, indicating the quadratic behavior due to compositional heterogeneity. Again, the number of accumulated spectra shows a strong influence. The more spectra are accumulated, the less the variance which is an indication, the measurement noise, from one spectra to the next, still plays a role. At the same time the sample volume is increased. Again the influence of the different probes does not disappear.

Variance, calculated on the concentration predictions, as shown in Figures 5.9 and 5.10 obtained by a chemometric model, clearly shows the dominant influence of compositional heterogeneity. The quadratic behavior based on concentration is dominant. Nonetheless, the number of accumulated spectra has a significant influence on the obtained variances.

For a certain test (10 accumulations and lowest turntable speed) the measured

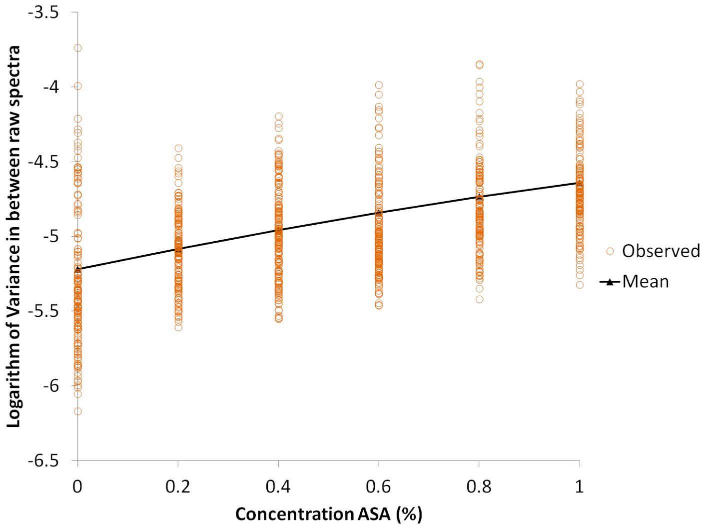

Figure 5.5: Variance versus concentration for unpretreated spectra. The glossy appearance of ASA leads to a more intense signal, and hence to an increased variance level.

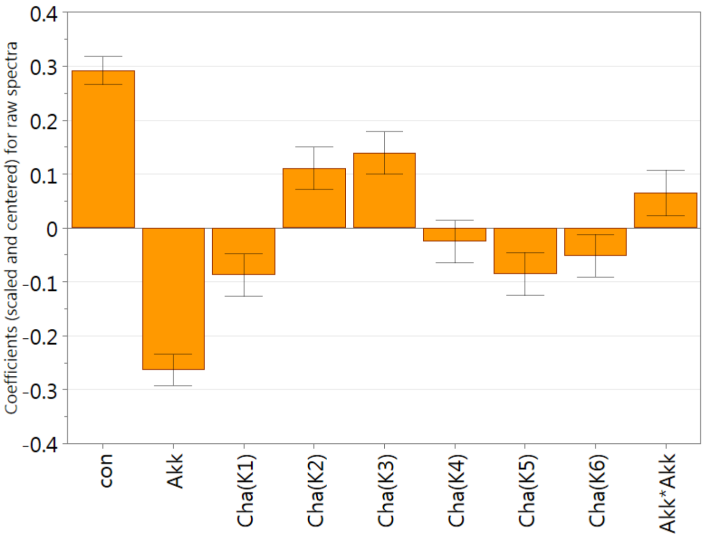

Figure 5.6: Coefficients for variances of unpretreated spectra. The concentration (con), number of accumulated spectra (Akk) and the probe number (Cha(#)) are influental.

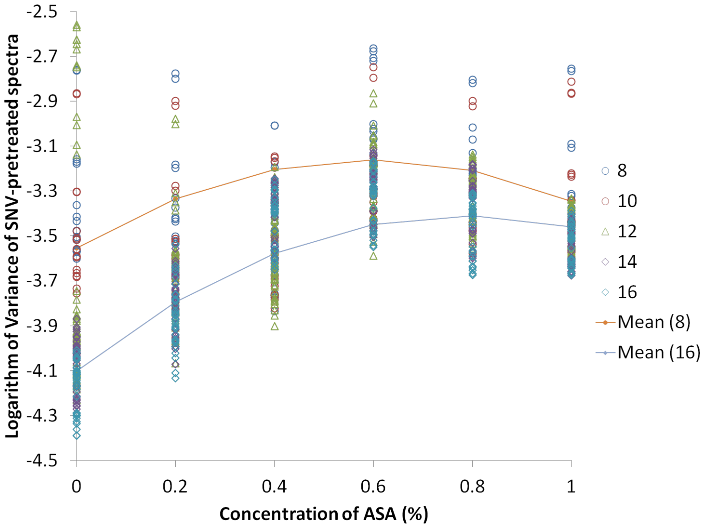

Figure 5.7: Variance versus concentration for SNV-pretreated spectra. The concentration has an influence on the variance, as well as the number of accumulated spectra, as can be seen by the difference of the mean values for different accumulation numbers.

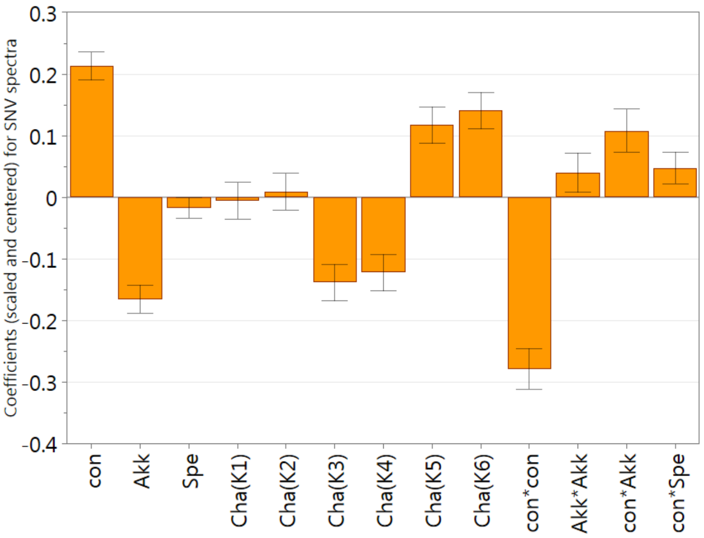

Figure 5.8: Coefficients for variances for SNV-pretreated spectra. As opposed to Figure 5.6, a quadratic term is necessary to describe the influence of the concentration (con*con).

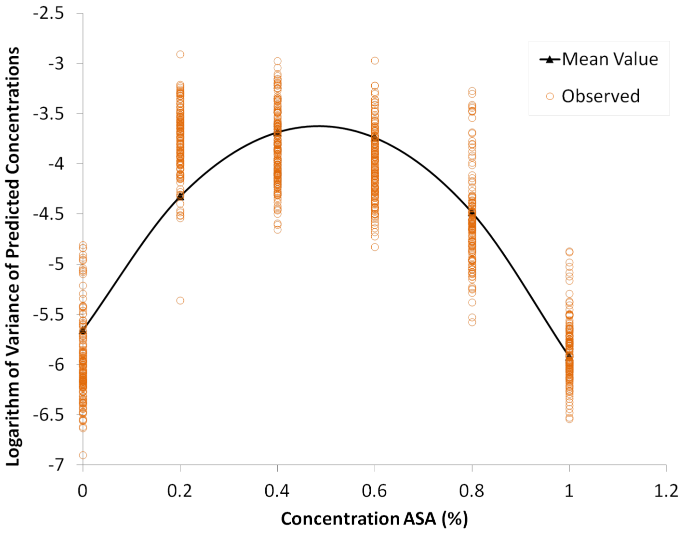

Figure 5.9: Variance versus concentration for predicted concentration levels. For the predictions, the variance follows the theoretical $\propto c(1-c)$ behavior.

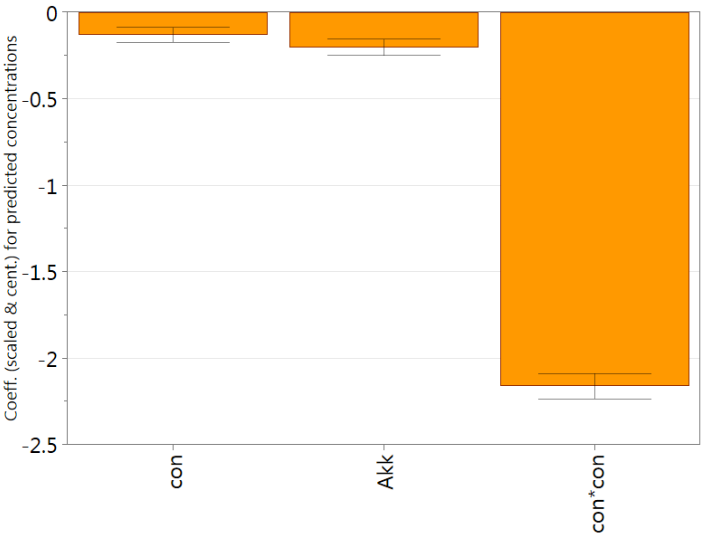

Figure 5.10: Coefficients for variances for predicted concentration levels. The non-significant coefficients are not shown; hence for the predicted concentration levels, the gained variance is independent of the probe number.

and theoretical variances are plotted in 5.11. The blue line indicates the theoretical variance level, whereas the other lines represent the confidence levels (hence 50% of all measured variances should be below the turquois line labeled with 50%). This is in good agreement.

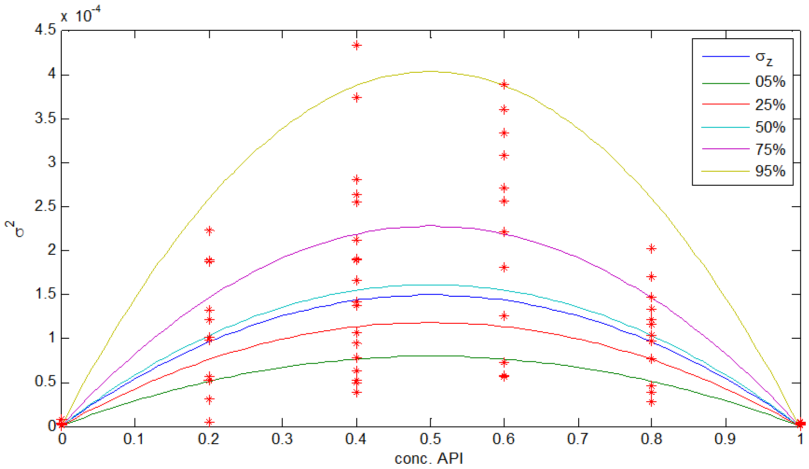

Figure 5.11: Empirical and theoretical variances for different concentration levels. σ_z is the theoretical variance, and the colored lines give the confindence level (i.e. the fraction of measured variance values that should be below this level).

Selecting a certain concentration level, e.g. a mass fraction of 0.4 API, the aforementioned relationship in equation 2.51 can be shown, as displayed in Figure 5.12, which fits quite nicely. Please note that the degrees of freedom is 10-1 in our case, as the empirical variance was calcualted over 10 spectra (each an accumulation of 10 measurements.)

Furthermore, when knowing the theoretical variance and the measured variance for several levels, it is possible to extract the variance of measurement and model via OLS-based variance estimation [100]

$$s_M^2 = \frac{\sum_i (s_i - \sigma_{z,i})^2}{n-1} \tag{5.11}$$

which yields the result $s_m^2 = 2.5 \cdot 10^{-5}$. Ergo, this is the lowest level of variance we can measure with the current set-up. This fits quite nicely with the variance measured for pure substances (which do not have compositional heterogeneity, and hence should reflect model and measurement error only, too) which are at a

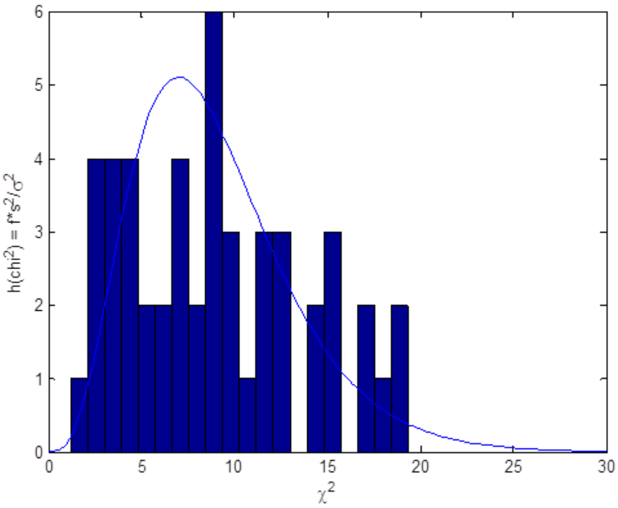

Figure 5.12: Histogram of the ratio of empirical and true variance. The line gives the corresponding χ^2-distribution. This is a cross-section of Figure 5.11 at $c = 0.4$.

level of $\sigma^2_{M,0} = 1.5 \cdot 10^{-5}$, and can be estimated by Figure 5.11 at the border cases (when zoomed in).

5.1.3 Conclusion

It is necessary to understand the behavior of measurements on the rotating disk for two reasons. First, the disk is a simplified set-up, compared to the actual blending vessel, and more possibilities for the intentional variation of parameters exist. Hence, effects observed on the rotating disk help in interpreting the blending.

Second, the disk was further used, in combination with the tumbler blender, to present perfectly mixed samples to the NIR-probes, and to build models which were then used in the following, to interpret spectra of actual blending processes.

5.2 Penetration Depth

Penetration depth was measured by building a slope of powder with changing thickness. For point measurements, this was done on the turntable, in order to have sufficient statistics, like shown in Figure 5.13.

For the imaging system, a linear chock was used. A defined height of the powder bed was constructed by using layers of aluminum foil for thickness determination. A similar approach is described in [27].

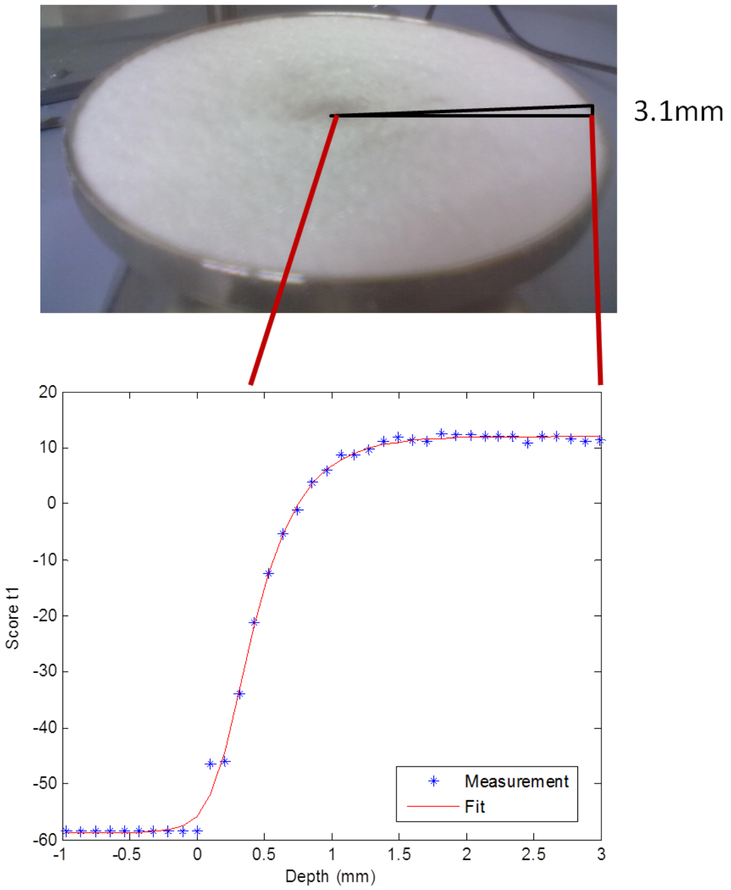

Figure 5.13: Sketch for calculating the penetration depth on the turntable. The score values decline at a certain powder bed thickness, when the powder bed is practically "infinitely thick".

To calculate the penetration depth, a PCA was built from the data. The highest principal component, showing the appearance of the chemical signature of the underlying material was than used. (Others showed the change of detector-sample distance, etc.) The gained score values were plotted against the powder bed height at this position. The data was then fitted to the generalized logistics regression function

$$Y(t) = A + \frac{K - A}{\left(1 + Q \exp^{-B(t-M)}\right)^{\frac{1}{\nu}}} \tag{5.12}$$

where A, K, Q, B, M, ν are fit parameters and t the powder bed thickness. The depth of penetration was defined by the powder bed thickness, when the score value was only $1/e$ of its original value, hence

$$t_{\frac{1}{e}} = \frac{1}{B} \cdot \left(BM - \ln\left(\frac{e^{\nu} - 1}{Q} \right) \right) \tag{5.13}$$

Hereby, the wavelength dependence of the penetration depth was neglected.

Furthermore, penetration depth is dependent on the illumination and detection setup, and strongly on the particle size. Even more, the voids separating particles, and hence bulk density, effect the obtained penetration depth. Therefore, the penetration depth was determined multiple times with different blend components, in order to have an estimation of its change. Results can be seen in the Figures 5.14 and 5.15.

Clearly, the main influence factor for the penetration depth in powders is the particle size. Voids in between the particles allow the radiation to penetrate further into the bed, without being absorbed or scattered.

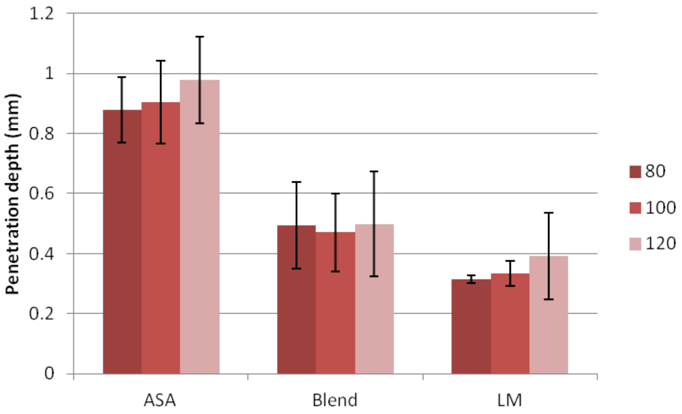

Figure 5.14: Penetration depth with the push-broom system for different substances, and a blend of ratio 50:50. Further on, different illumination intensities were tested (80,100,120 W of power).

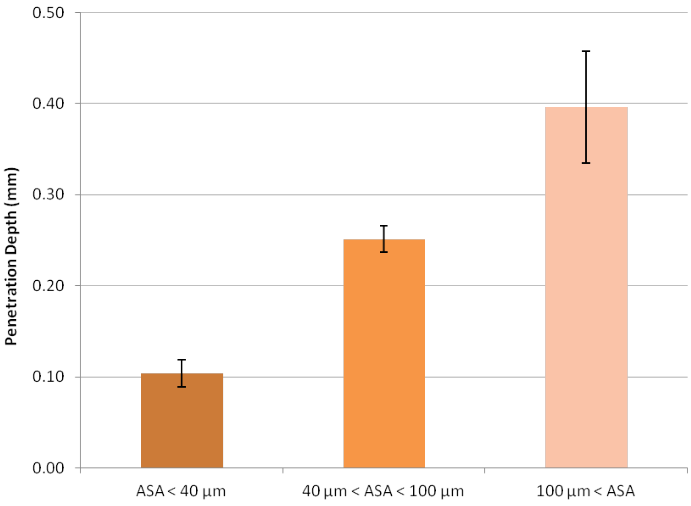

Figure 5.15: Penetration depth with the cupped fiber, and different particle sizes. Smaller particles exhibit a tremendously lower penetration depth.

5.3 Continuous Dosing

5.3.1 Introduction

Powder flow is an ever occurring event, in industry as well as in nature. The issue of granular material in movement, spans the length and time scale from debris to filling a pharmaceutical capsule. Moreover, powders are a complex system of solid granules, with a variety of attributes, and a gaseous filling phase, exhibiting very different behaviour, dependent on current and past external factors [74, 112]. Therefore, the monitoring of powder flow is still a challenging task [142].

Here we use a push broom based imaging system, for monitoring a powder flow leaving a dosing feeder. Not only can we determine the spatial distribution of the substances; even more it is possible, to change the sample size on the fly, by changing the number of pixels considered. This enables to change the scale we look at and enables to asses heterogeneity on different scales of scrutiny.

5.3.2 Experimental Set-Up and Spectral Interpretation Techniques

Hyperspectral Imaging and Push-Broom Technique

The spatial resolution in one direction is determined by the detector and the distance of the detector to the sample. To map a complete image, the sample is moved beneath the detector with a constant velocity. Choosing time and space as axis, a picture, at the detected NIR-wavelengths, can be reconstructed. The collected information therefore is

$$I(x, t, \lambda) \tag{5.14}$$

i.e. the reflected intensity I, in dependence of position x, time t and wavelength λ. Hence the information forms a so called *hypercube*. Such a reconstructed image is displayed in Figure 5.16.

Samples, Sample Preparation and Sample Presentation

---

[1] ©2012 IEEE. Reprinted, with permission, from Scheibelhofer et al., Continuous Powder Flow Monitoring via Near-Infrared Hyperspectral Imaging, I2MTC, May 2012

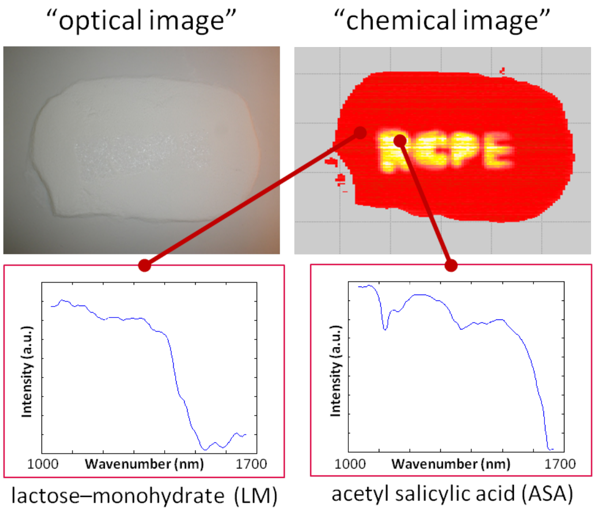

Figure 5.16: Comparison of an optical image (left), and an hyperspectral NIR-image (right). Although only the intensity of one certain wavelength is displayed in the image, the whole spectra for every point in the image is measured and available. Hence the two substances can be identified (below).[1]

Such push-broom based cameras are already in use for sorting in the fields of recycling and food classification. However, here the focus is put on powders. Therefore, the used model substances are pharmaceutical powders; those were already presented in section 3.6.

As the samples have to move in front of the camera, the camera was tilted. A ceramic plate served as glide for the powders, and at the same time as reference image for the measurements. The powders were fed on the glide by a screw feeder. A picture of the experimental setup can be seen in Figure 5.17.

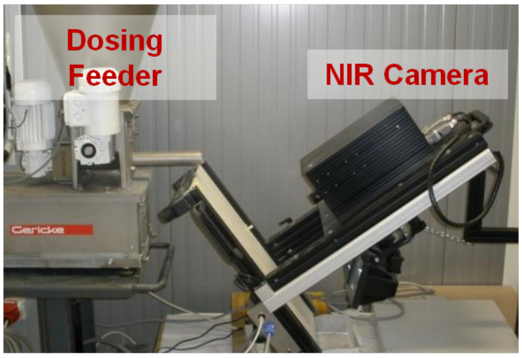

Figure 5.17: The experimental setup. The feeder can be seen left, its outlet deposits the powder on the plate. The powder then glides past the camera detection area. This setup is similar to the one used by [76].[2]

Data Acquisition and Pretreatment

The camera was operated at a rate of 25 Hz and the spectra were integrated for 10 ms. This proved to be sensitive enough and adequate in spatial resolution, while the amount of data produced was still manageable. The spectral data were pretreated as follows:

- Black and white adjustment: As the illumination at the detection line is not uniformlyy equal, the measured intensities are adjusted.
- Transformation to pseudoabsorbance: Beer's law states that concentrations are linearly related to the absorbance in transmittance. Therefore, the gained signal here, although a reflectance signal, is transformed the same way, in order to achieve a roughly linear relationship between pseudoabsorbance and chemical concentration.
- Smoothing: A Savitzky-Golay algorithm was used to smooth the spectral data.
- Offset correction: As the distance of the sample surface to the detector is not always the same, due to height patterns in the sample etc., an offset correction was performed to reduce this influence.

---

[2] ©2012 IEEE. Reprinted, with permission, from Scheibelhofer et al., Continuous Powder Flow Monitoring via Near-Infrared Hyperspectral Imaging, I2MTC, May 2012

Spectral Interpretation

For every image pixel, a spectrum is measured, and a PCA is performed on the whole dataset.

This way, an acquired image can be analyzed relatively easy, and differences in the sample, as caused by different chemical composition can be detected without further human intervention. However, it is necessary to look at the loadings, to asses on what they represent. Here, principal components often alternate in between chemical information and geometrical information, for example intensity differences due to slopes resulting in different reflection angles.

For establishing a quantitative model, premade blends have been prepared in a tumbling blender. Then those blends and the pure substances have been presented to the camera on the glide. As the glide was not fully covered by the calibration samples, for every calibration step (at 0, 33, 50, 66, 100%) 100 spectra of the whole image have been chosen. These spectra were selected by looking at the intensity of certain wavelengths, and have been controlled manually, as demonstrated in Figure 5.18. PLS was then used to establish a chemometric model. The resulting model had sufficient accuracy, in order to resolve changes in concentration for individual blends.

5.3.3 Monitoring Impurities

By performing a PCA on one of the measurements, impurities can be detected on the fly. In Figure 5.19 some crystals of our model API have been put as impurities onto a bed of LM.

The consecutive principal components show different attributes of the powder bed. The colour of every pixel is determined by the score of this pixel for the according principal component. Whereas the first component reflects the difference between the powder and the background plate, and the second component shows the influence of the angle of the powder bulk surface, finally the third component reflects the chemical difference between acetylic salicylic acid and lactose. The resolution was high enough, to distinguish single ASA crystals.

In contrast, there are some limitations. As NIR just offers a penetration depth of roughly 0.5 mm for such fine granular media, just the top surface of the powder flow can be analysed. If some substance is hidden beneath the analysed powder flow, it would not be detected in this setup.

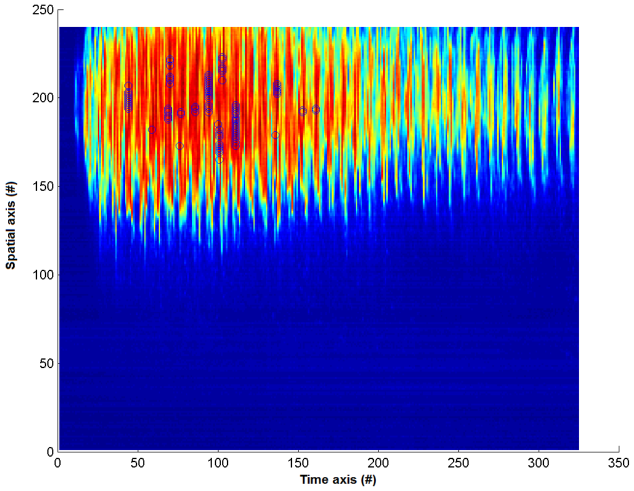

Figure 5.18: Powder flow across an inclined plate. The intensity at 1000 nm is shown, the vertical axis represents spatial pixel, whereas the horizontal axis represents the consecutive numbering of acquisitions. Spectra used for calibration later on were selected by the intensity profile, and are marked by circles in the image.

5.3.4 Monitoring Powder Flow

In Figure 5.20 we can see the powder leaving the feeder in a very intuitive way. A PLS model was used to determine the concentration of every pixel. Clearly the chemical inhomogeneity can be seen. In this example this was induced by layered filling of the feeder. As a contrasting example, we refer to Figure 5.21, which is a homogeneous premixed sample.

However, at the border of the flow regime, the particle density becomes very low. As the spectral intensity is lower, this is interpreted as a lower concentration. This can be corrected by also taking a “concentration of the background” into account or mathematically forcing a sum of 100% of the powder components. This is successful for correcting the periodical feeding rate, as can also be seen in the image very clearly. Although, for very low coverage, this is not feasible any more and the predicted concentrations at the border of the powder flow bear a large error. This is caused by the transition form diffuse reflectance to single particle reflectance.

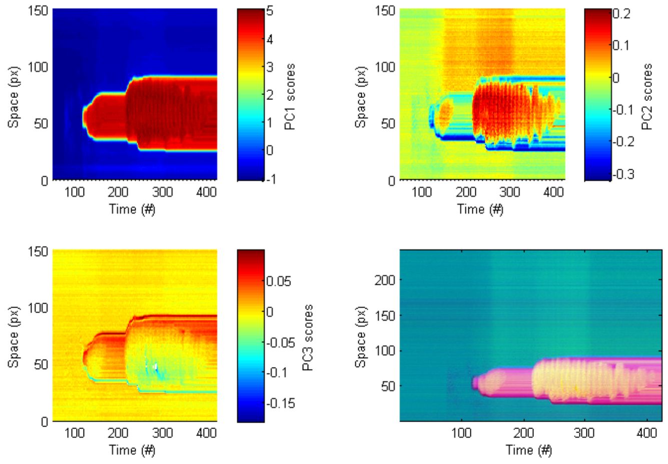

Figure 5.19: A PCA was performed on the recorded data of the powder passing the sensor. The impurities are clearly distinguished from the background substance in the third principal component. The colour represents the score value. Thew lower left image is a RGB-composition of all three score values.[3]

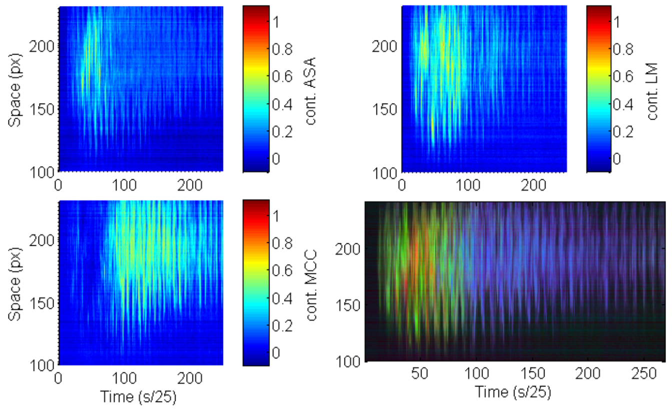

Figure 5.20: PLS analysis of fed powders. The first three pictures represent colour coded the concentration of the three different components. The intermittent flow caused by the feeder can be seen, as well as the loss in reflected intensity at the edges of the flow. Thew lower left image is a RGB-composition of all three score values.[4]

---

[3] ©2012 IEEE. Reprinted, with permission, from Scheibelhofer et al., Continuous Powder Flow Monitoring via Near-Infrared Hyperspectral Imaging, I2MTC, May 2012

[4] ©2012 IEEE. Reprinted, with permission, from Scheibelhofer et al., Continuous Powder Flow Monitoring via Near-Infrared Hyperspectral Imaging, I2MTC, May 2012

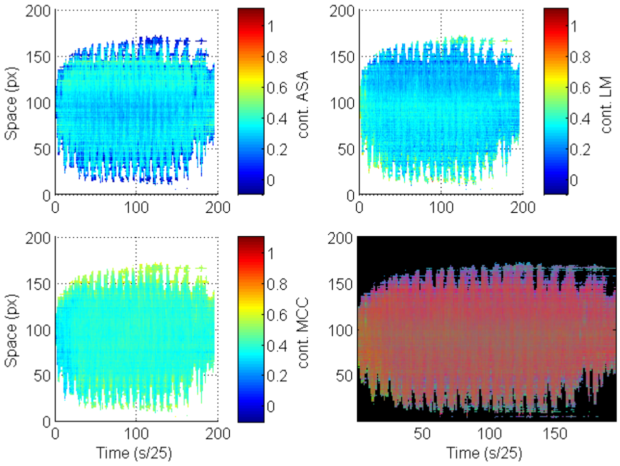

Figure 5.21: Example of a chemically homogeneous powder flow. Although the nominal concentration should be the same, at small scale there are deviations due to subsampling. Furthermore, there are miss-predictions at the edge of the flow.[5]

The confidence interval for the predictions was estimated by knowing the span of the calibration data X, the residual matrix E, the number of samples N, and the number of variables M, by

$$I = \frac{\sqrt{\mathrm{abs}\left(\mathrm{tr}\left(X\left(XX'\right)^{-1}X\right)\right)} \cdot \sum_j \sum_i e_{ij}^2}{N-M} * T_{\frac{\alpha}{2},N}, \tag{5.15}$$

where `tr` denotes the track, and $T_{\frac{\alpha}{2},N}$ a student-t coefficient; the intervals can be seen in Figure 5.22.

5.3.5 Depth of Scrutiny

Concentration and Sample Size

In the following we assume that our prepared samples (prepared in the tumbler blender) are stochastically homogeneous which should be guaranteed by the

---

[5] ©2012 IEEE. Reprinted, with permission, from Scheibelhofer et al., Continuous Powder Flow Monitoring via Near-Infrared Hyperspectral Imaging, I2MTC, May 2012

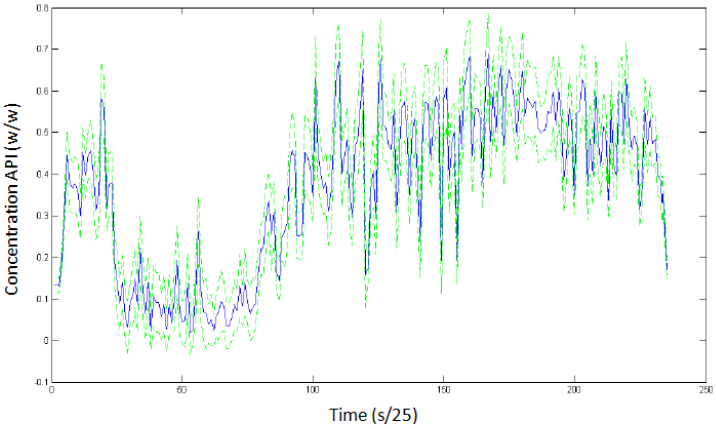

Figure 5.22: Estimated concentration of MCC with 95%-confidence interval, at pixel number 70 in Figure 5.20.

working principle of the blender and a sufficient blending time. Hence, they show no distributional heterogeneity.

It is then observed that our measurement device and mathematical interpretation is sufficient enough, to detect compositional heterogeneity.

Sample Volume in the Near-Infrared Case

When using NIR for sampling, the sample size is determined by certain factors:

- Penetration depth of NIR which is dependent on the substance;
- Area of the detection spot which is an attribute of the spectrometer optics and the sample distance;
- Integration time of the spectra;
- Amount of substance, passing this spot, during said time;

In the presented setup, we determined those parameters, and calculated the sample size to be around 3.6 mm^3.

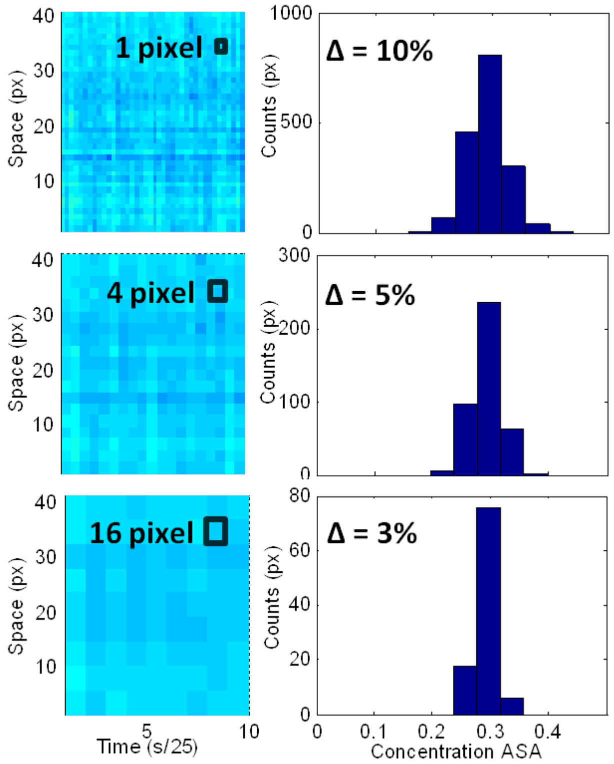

Figure 5.23: On the left hand side, a cutout of the measured homogeneous flow is presented. The rectangle indicates the sample size which is increased by summing up pixels. On the right hand side, a histogram of the concentrations is plotted. With increasing sample size, the width of the histogram narrows down. The numerical value Δ gives the expected 2-σ interval of the histogram, centered around the nominal value of $c = 0.33$.[6]

---

[6] ©2012 IEEE. Reprinted, with permission, from Scheibelhofer et al., Continuous Powder Flow Monitoring via Near-Infrared Hyperspectral Imaging, I2MTC, May 2012

Effects of the Sample Volume

Due to constitutional heterogeneity a certain minimal variance has to be expected.

The particle size distribution of ASA was modeled by a log-normal distribution. Therefore, we are able to estimate fraction/sample-volume ratio, and hence the variance and deviations in concentration, we expect to be observed (according to equation 2.50). In contrast, Figure 5.23 shows the experimentally determined concentration levels as histogram. The width of the histogram nicely corresponds to the expected (calculated) deviations of concentration due to finite particle size.

As a benefit of spectral imaging, the sample size can be changed afterwards, as indicated in the same Figure 5.23. By summing up pixels, after the measurement, we can still increase the sample size. As expected, the measured variance goes down.

On a further note, the measured variance will not be exactly the theoretical. As samples are drawn at random position, the variance also has the character of a random variable. Hence, the measured variances follow a χ^2-distribution, with its mean at the expected variance. This was also seen experimentally.

5.3.6 Conclusion

We have seen that NIR imaging can be used rather straightforward for monitoring powder flow. Further, its resolution is high enough to detect impurities. Although a homogeneous flow of equal thickness, without boundaries is preferred.

No general guideline for optimal sample size can be given, as this is dependent on process, product and measurement equipment. However, one has to be aware that fluctuations with a certain magnitude in concentration will appear intrinsically, and are determined by the sampling size.

5.4 Batch Blending Process

5.4.1 Introduction

In this work, simultaneous measurements of the powder composition at several positions of an agitated lab-scale blender were conducted. In our setup an FT-NIR spectrometer was connected to the blender via an optical fiber switch. The blender was equipped with six NIR-diffuse reflection probes. Using the switch made it possible to alter between those probes consecutively. One after another, the signals were then directed into the spectrometer. Using only one spectrometer made it easier to compare the spectra, as no corrections need to be made, for example, to avoid a signal drift between two different spectrometers. This method allowed us to continuously monitor a powder blending process and to study the blending (and segregation) kinetics.

5.4.2 Experimental Set-Up

For the experiments, the three ports at the bottom of the stainless steel vessel (position 1,2,3), and the three lowermost ports at the wall (position 4,5,6) were plugged with NIR-probes, whereas the other ports were sealed. For an amount of 140 g of material, the fill level was just above position 6, giving a height-to-diameter ratio of about $H/D = 0.35$ (see Figure 3.3). The NIR-probes were connected via a fiber switch to the FT-400 spectrometer, and the general setup can be seen in Figure 5.24.

As a consequence, due to the materials' tendency for segregation, it is not possible to perform calibration measurements inside the blending vessel. Therefore, a different calibration setup was used, namely the rotating disk described before.

Obtaining one spectrum with the spectrometer at a resolution of $2\,\mathrm{cm}^{-1}$ took 0.35 s. 12 spectra were accumulated for one position, this position was monitored for 4.2 s. After monitoring, 23.1 s ($5 \cdot 4.2\,\mathrm{s}$ for the other five positions + $6 \cdot 0.35\,\mathrm{s}$ skipped spectra) elapsed before the same position was monitored again. Therefore, this approach may be suitable for studying long-term process dynamics rather than very fast ones.

An important advantage of our method, however, is that only one spectrometer is used, and thus no further operational steps are required to compare the measurements at different positions. Note that with NIR only the surface of the

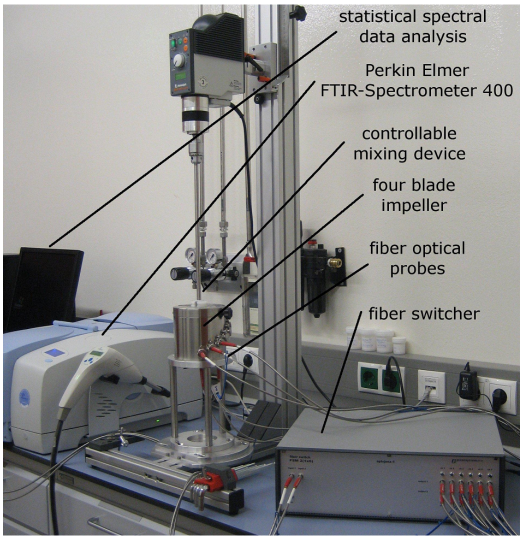

Figure 5.24: Set-up for lab-scale blending. The blending vessel, impeller gear, fiber switch and FT-spectrometer can be seen.

blending volume can be probed, while information regarding processes inside the blending vessel cannot be obtained.

5.4.3 Establishment of The Chemometric Model

Premixed binary powder blends with predefined concentrations were mixed in the tumbler blender for 16 min at 50 rpm. A separate set of experiments using hyperspectral imaging has shown that for these materials, after 8 minutes no significant change in homogeneity could be detected for longer blending times [143]. Hence 16 minutes for preparing the calibrations samples was chosen. The resulting blends ranging from 10 to 90% (w/w) concentrations with increments of 10% were used as calibration samples.

Several studies showed that there was a difference between measuring static and moving samples [144]. Thus, it can be concluded that it is optimal to perform calibration under the same conditions as the blending measurements. In our case, this would require calibration inside the blending vessel which was impossible for a number of reasons (i.e. the powders may segregate, window fouling may occur, all sensors may not detect the same concentration, etc.)

Therefore, a different setup was chosen to perform the calibration, using the strategy described in the literature [144], and implemented the following way, as already described in section 5.1.

This setup allowed fast calibration with predefined blends for all six positions simultaneously. Furthermore, the conditions under which the calibration samples were prepared are replicable. Thus, the powder bed is moving in front of the sensor, making calibrations more similar to the actual experiment inside the blender. At the same time, there is no movement of the powder bed itself that could induce segregation.

PLS was used for correlating spectra and components' concentration. It is applicable to our case since, to predict concentrations, a quantitative model was required rather than a qualitative model that is based on principal components analysis which can only identify steady-state levels. The spectra obtained from the spectrometer were already the mean of twelve consecutive spectra. Next, spectral pre-treatments were used to enhance the power of the predictive model. The methods used consecutively were:

- Wavenumber averaging: The resolution of the spectrometer was $2\,\mathrm{cm}^{-1}$, but the wave numbers were then averaged by taking the mean of 8 values (therefore a range of $16\,\mathrm{cm}^{-1}$) to modify the signal-to-noise ratio.
- Cutting of the spectral band: the region of $4489 - 7171\,\mathrm{cm}^{-1}$ was ultimately used, since due to the applied optics the regions with higher and lower wave numbers showed mainly noise and disturbances but no chemically relevant information.
- Standard normal variate (SNV) was used to account for physical differences, mainly a change in the distance, powder bed to sensor window, between calibration and measurement.

To account for the different optical paths and different fiber faces, a separate model for every position was created. The number of PLS components was chosen to be five.

The resulting model parameters are summarized in Table 5.1. Slope, offset and R^2 refer to the comparison of nominal and predicted concentrations. For an optimal model, the slope should be 1, offset 0, and $R^2 = 1$. However, these ideal values cannot be achieved due to statistical errors and nonlinear behavior of absorption and concentration [98]. The RMSE was used to estimate the error of prediction [145]. All predictions by the model, as shown in the figures below, have a standard deviation of about ±5% ASA.

		Slope	Offset (%)	RMSE (%)	R^2
Position 1	Cal.	0.98	0.91	3.67	0.98
	Val.	0.96	1.98	4.81	0.98
Position 2	Cal.	0.99	0.48	2.67	0.99
	Val.	0.98	0.81	3.07	0.99
Position 3	Cal.	0.99	0.54	2.82	0.99
	Val.	0.98	1.05	3.38	0.99
Position 4	Cal.	0.99	0.5	2.72	0.99
	Val.	0.98	1.01	3.13	0.99
Position 5	Cal.	0.98	0.82	3.47	0.98
	Val.	0.97	1.64	4.02	0.98
Position 6	Cal.	0.97	1.41	4.55	0.97
	Val.	0.96	2.04	5.88	0.96

Table 5.1: Parameters of the predictive PLS model. Separate models exist for every position. The first row for every position displays the parameters for the calibration model for all classes and RMSEC. The second row contains the statistics for the cross-validated model and RMSECV. Slope, offset and R^2 refer to the comparison of nominal and predicted concentrations.

5.4.4 Sampling Considerations with NIRS in the Blending Vessel

To assess the homogeneity of the blend, the standard formula for empirical variance was chosen, as mentioned in Equation 2.49. In contrast to traditional thief sampling, the sample size is determined here by the optical set-up and some considerations have to be made. The stochastic homogeneous mixture in a binary blend is defined by $\sigma_z^2 = c(1-c)1/\eta$, where c is the concentration of one component, and η is the number of particles of the larger-particle species in the sampled volume [146]. As the particle size distributions of both substances are known, their size distributions can be approximated by a log-normal distribution, as seen in section 5.1.1.

An estimate of the sample volume based on geometrical considerations is $V_S = (d/2)^2\pi * p * (1+k/d)$, where d is the opening of the fibre, and p the penetration depth into the powder blend. The fiber opening has diameter of 600 μm. As the fibers are separated from the material just by the sapphire window, this aperture was neglected. The penetration depth has been determined experimentally and depends on the blend composition. A mean value of 350 μm was determined. Hence the first part of the equation describes the illuminated and thus sampled area in the static case. As the powder is dynamically moving in front of the window, the fraction k/d estimates, how the sampled volume is enlarged by the powder movement. In a first approximation, the powder moves at f times the speed of the agitator's blade tip. Hence, we can estimate k by $k = f * \omega * r * n * t$, where $\omega \cdot r$ is the angular speed of the impeller and $n \cdot t$ is the time during which n spectra are recorded. The number of ASA particles η contained in the volume has also to consider the porosity ε and is therefore estimated by $\eta = V_S / V_A (1 - \varepsilon)$, with V_A being the typical particle volume of the larger species, i.e. ASA in this case.

Thus, in order to give a reliable prediction for the concentration estimated with NIR measurements, we use the relationship described in Equation 2.51 and can therefore estimate the number of particles in the sample volume which are necessary to estimate up to a certain accuracy (Δc) the concentration [113]. For a confidence of 95%, the factor $z(S) = 1.65$. Typical limits for the assumed sample size are shown in Figure 5.4. The figure demonstrates that even for well-mixed blends, concentration deviations in the order of 5% ASA and more should be expected.

The overall variance of the concentrations measured during blending is hence a sum of variances in the blend itself (σ_z^2), and errors originating in the chemometric model (σ_{model}^2) and the measurement devices (σ_{device}^2) itself. The error of the model was mentioned already and manifests itself in the RMSE value. The error induced by the measurement devices itself has been estimated by repeatedly measuring the pure components, and calculating the variances in between those measurements. It turned out that the error caused by the devices is negligible (i.e., two orders of magnitude smaller) compared to the error by the chemometric model and the error due to the finite sample size.

As a result, the number of 12 accumulated spectra was chosen, providing sufficient measurement accuracy, while still allowing a feasible number of time steps measured during the process. Additionally, the number of spectra to be discarded because of optical switching operations is acceptable. Although, for the calibration disk, the observed volume is larger, the identical spectral acquisition parameters were used, in order to avoid unexpected effects.

A second issue to consider is the size of the final dosage form. To ensure homogeneity at the size level of the solid dosage form, the measurement volume must be equal or smaller. The volume of a tablet of 8 mm in diameter and 1.5 mm in thickness is about 75 mm^3. The measured volume in our experiments was about 16 mm^3. (In reality, the monitored volume may be even lower, as close to the wall velocity gradients developed). Thus that the volume sampled was smaller than the dosage form, especially under the consideration that the powder will undergo a compression step later on.

5.4.5 Time-Evolution of Blending: Concentration Levels

Having estimated the sampled volume, blending experiments can be performed and heterogeneity assessed.

In this study, experiments were conducted to study (a) blending dynamics in the mixer, (b) to investigate whether segregation occurs and if it can be monitored in real-time and (c) how different locations are affected by the mixing dynamics in the system. The total amount of powder used was 140 g in each case. Every experiment followed the same strict protocol to ensure comparability and repeatability:

- Measurement of the spectral background. Spectralon©in contact with the sapphire windows in the vessel was used as a reference material.
- The first powder component (or the premix) was placed into the empty vessel.
- The four-bladed impeller was inserted and positioned 1mm above the vessel bottom.
- Filling of the second powder component, or the premix.
- Simultaneous start of the powder blending process and the measurements.

Two different starting conditions were chosen, in order to elucidate the blending process.

1. Preblended material of two species.
2. Two separated layers of material species.

Segregation of a Preblended Mixture

To test for segregation of the binary blends, a premix of 50% ASA and 50% LM was prepared in the aforementioned turbula blender. The premix was then placed into the blending vessel.

Figure 5.25 shows the concentration at the 6 NIR probes for 400 revolutions. It can be observed that most positions started at a concentration of 50% API, with the notable exception of position 4. This position is at the same height as the agitator blade and hence the recorded spectra are influenced by the blade repeatedly passing the sensor. Thus, the premix was clearly well mixed and neither the turbula blender nor the filling procedure did induce segregation. However, after a few revolutions the concentrations changed dramatically. The three positions at the bottom (positions 1, 2 and 3) showed a sudden decrease in the amount of ASA. While the same was true for the lower position on the side wall (position 4), the situation was the opposite for the positions higher up on the side wall (positions 5 and 6). These observations strongly indicate that segregation occurred quickly due to the movement of the agitator. Similar observations were also made in the literature, e.g. [147].

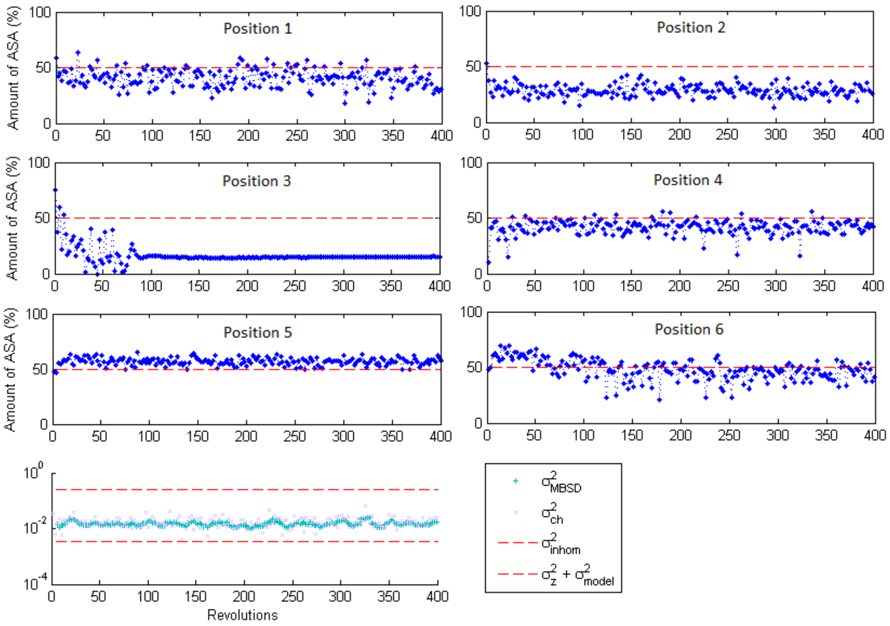

Figure 5.25: Concentration of ASA over time, for the case of segregation. Dashed lines show the nominal concentration. In the bottommost image the calculated variances are shown, together with the limits for completely separated and stochastically mixed blend.[7]

---

[7] Reprinted from Powder Technology, 243, Scheibelhofer et al., Spatially resolved monitoring of powder mixing processes via multiple NIR-probes, 161-170, (2013), with permission from Elsevier.

Most likely due to a size segregation mechanism (sieving effect), during the first few revolutions the larger ASA particles were transported upwards and LM downwards, i.e. the smaller LM particles fall into the gaps between the larger ASA particles. This is just possible inside a moving powder and leads to a net flow of small particles downwards, and indirectly large particles upwards. Hence, care has to be taken interpreting these results, as smaller particles trickle through the larger ones and may form a layer on the bottom sensors, shielding the ASA particles. However, as position 4 at the side wall also shows a decreased level of ASA, this cannot be the exclusive reason for the observed effects.

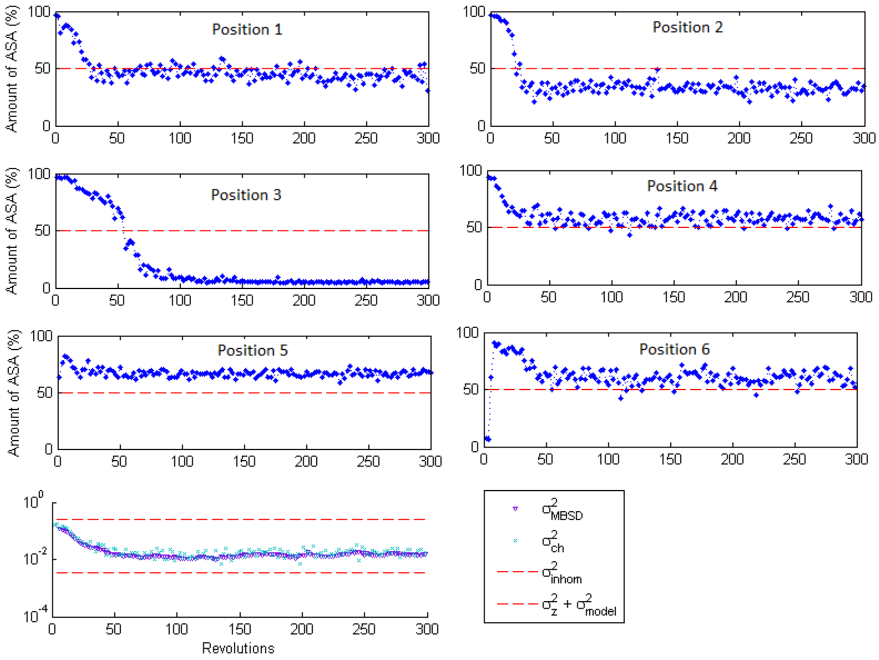

Figure 5.26: Concentration of ASA over time, for the case of blending. Dashed lines show the nominal concentration. In the bottommost image the calculated variances are shown, together with the limits for completely separated and stochastically mixed blend.[8]

After approximately 100-150 revolutions, a steady state is achieved. Although the concentrations showed fast fluctuations, due to the small sample volume,

---

[8] Reprinted from Powder Technology, 243, Scheibelhofer et al., Spatially resolved monitoring of powder mixing processes via multiple NIR-probes, 161-170, (2013), with permission from Elsevier.

the long-term trends were constant. Further blending did not improve the blend quality.

Note that while all the other positions showed fast fluctuations, position 3 maintained constant after 150 revolutions. The raw spectra still show the expected absorbance pattern, and it can be concluded that it is not a void region in front of the sensor interpreted wrongly. The static behavior of the raw spectra confirmed that in this region no particle flow occurred, maybe due to the formation of agglomerates and/or a densified region at this critical position.

Blending of Initially Separated Powder

In these experiments 70 g of LM were loaded on top of 70 g of ASA before blending and measurements began. The results are presented in Figure 5.26. At the start, the lower positions (positions 1-4) had an ASA content of (nearly) 100% and the uppermost position (position 6) shows an excess of LM. Position 5 is in the intermediate region, where blending already had begun, when the first spectra were collected from this position. However, after only a few revolutions, significant changes occurred. As before, ASA tended to move upwards after a few revolutions, as indicated by the signals at the upper positions, whereas LM was dominant in the lower positions. Thus, the filling order became almost inversed.

As mixing continued, a steady state evolved after about 60 revolutions (except for position 3). Concentrations fluctuated but the integral value remained steady over a longer time period, and further mixing failed to increase the homogeneity. This steady state again favors ASA at higher regions of the powder bed and LM in the lower regions.

Interesting is also the radial behavior of the mixing process. Positions 1 and 2 first reached a steady state among the bottom sensors which indicates the largest powder exchange in this region. Position 3 showed a much slower approach to the steady state. Moreover, it cannot be decided, if the behavior is due to slow powder movement or material stuck to the sensor, causing the long time span until the final state is reached.

5.4.6 Time-Evolution of Blending: Homo- and Heterogeneity

Determining Homogeneity

Another important issue of powder blending processes are the blending dynamics which can be evaluated via a method that is similar to MBSD (moving block standard deviation). In our approach, the MBSD methodology [22] is applied to the PLS predictions instead of the raw spectra. Therefore, the weighting of certain spectral regions, as defined in the PLS coefficient vector, was conserved. This strategy was chosen since the deviations that may have been induced by the movement of the powder (which can be seen in the raw spectra), but do not give any information about the composition, were reduced in the PLS.

In principle, different methods can be used to calculate the variance for assessing homogeneity. First, the predicted concentrations of different positions can be used to calculate the variance. Second, separately for every position a moving variance can be calculated and averaged over all positions. Moreover, variance can be calculated with the empirical concentration mean of the measurements, or with the nominal (expected) concentration (i.e., 50%).

These values can be compared to the variance of the completely segregated mixture, and the variance of the stochastic homogeneous mixture which is in theory, the lowest achievable value for variance by a mixing process. Taking into account Equation 2.52 a confidence area can be defined. If the variance is below this value, stochastic homogeneity is achieved with a certain confidence.

An example of the variance over a blending process is shown in Figure 5.27. The experiment had the same conditions, as the previously discussed blending experiment. Again position 3, at the corner of the vessel, shows reduced dynamics. Therefore, this position was excluded for calculation of the variance. The decrease of variance over time can be seen clearly, as well as the point of achieving a stationary mixture. However, as indicated by the red arrow, when changing the sample size, also all the according limits change.

Finally it has to be assured that the error due to measurement and model is lower than the stochastic homogeneity, otherwise it can not be detected.

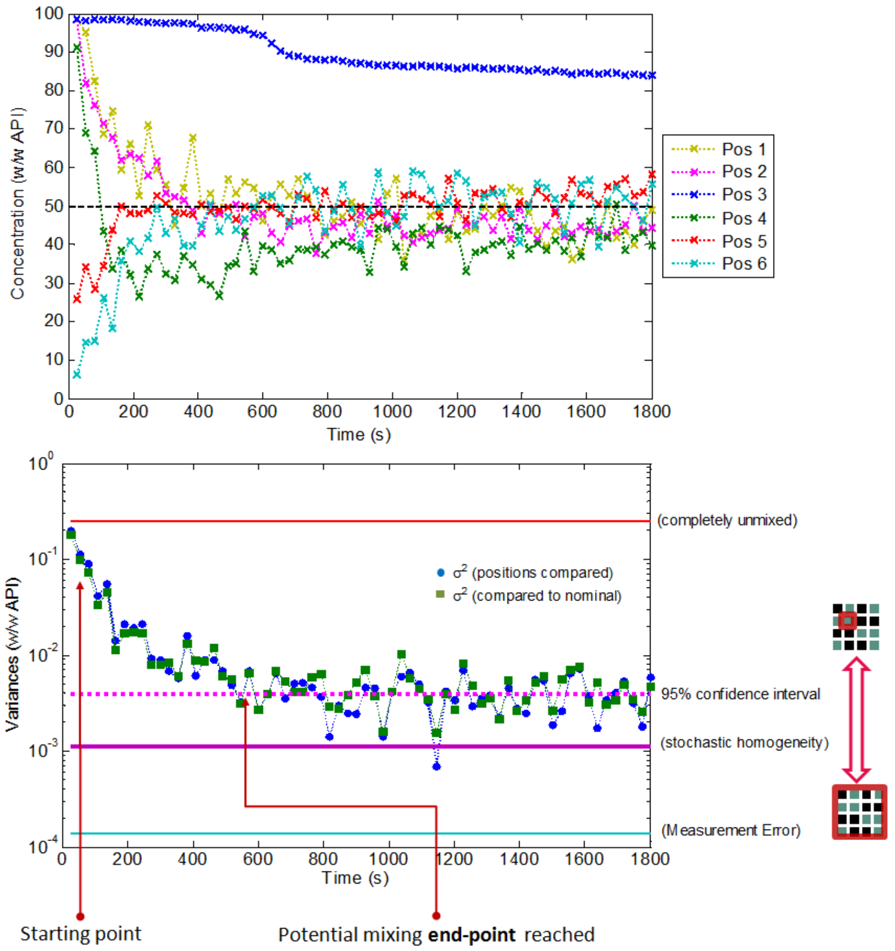

Figure 5.27: Above: Measured concentration level at different positions. Below: Decrease in variance during progression of blending. The achievable limit is dependent on the sample size.

Revision of The Blending and Segregation Process

Now, the previously discussed blending processes, can be discussed in terms of variance as well. Variance calculated by MBSD (σ^2_{MBSD}) and by comparing different positions (σ^2_{ch}), always with nominal concentrations are shown below the concentration trends in Figures 5.25 and 5.26. Position 3 was neglected due to its critical positioning.

For the segregation experiment, shown in Figure 5.25 during the first revolutions a rapid change of concentration is observed (e.g., position 2 and 3). The σ^2_{MBSD} is not able to capture this effect, as it occurs in just half the time of the considered moving block. In contrast, the σ^2_{ch} shows more fluctuations, but has lower values at the beginning of the experiment.

The same trend as in the concentrations is seen in the calculated variances which stay at a constant level over time, but do not reach the level of the stochastic homogeneous blend.

The calculated variances for the blending experiment, as shown in the bottom graph of Figure 5.26 show the typical behavior for a blending process, i.e., a decrease with time. The process could have been stopped after 70 revolutions already, as there was no change in mixing quality afterwards.

Similarities and Differences in Experiments

The initial states of both experiments are quiet contrary. The first experiment started with a stochastically homogeneous blend, whereas the second one started with a completely segregated blend. Nonetheless, the final blend qualities were similar but not the same. For example, positions 4 and 6 showed higher amounts of LM using the premix, compared to experiments with initially segregated powders. This indicates that powder mixing is dependent on the initial state of the system. Possibly, very slow mixing dynamics exist that after several thousands of revolutions would result in identical final states. However, from a practical point of view our experiments demonstrate that different steady-states are obtained for different initial condition, underlining the importance of online monitoring of blend quality.

The variances calculated reflect well the trends seen in the concentrations, and both methods of calculation give the same results. Whereas σ^2_{MBSD} reflects the fluctuations in time, σ^2_{ch} reflects the fluctuations in space. Note, the variances were based on the empirical concentration, attainment of a steady state would indicate “well-mixedness”. This is avoided by calculating variances based on the nominal concentration.

5.4.7 Improvement of The Chemometric Model

The presented chemometric model should be improved. Hence, the reasons for bad model performance, and ways to improve the model were analyzed next, as shown herein.

Difference between Calibration and Measurement

This time premixed blends were prepared in the tumbling blender for 20 min at 50 rpm to ensure homogeneity. Blends, with more concentration levels than before, i.e. with API contents of 0, 5, 10, 20, 30, 40, 45, 50, 55, 60, 70, 80, 90, 95 and 100% (w/w) were prepared for calibration. The premixes were placed on the turntable and spectra recorded.

The following differences between the calibration and in-line measurements were observed:

- Although the powders were moving in both cases (i.e., rotating disk and blender vessel) ensuring that the sampled powder mass was sufficiently high, the speed at which the powders were passing through the incident beam of the optical fibers was different.
- During the blender measurements, only a sapphire window separates the fiber from the vessel interior, whereas during the calibration there was a small gap of air to prevent powder segregation due to the probes.
- The optical fibers were bent slightly differently which might have led to artificial absorption bands in the spectra.

Spectral Acquisition and Pretreatment

Spectral pre-treatment was applied to separate the chemical signature contained in the signal from the physical interferences due to differences in the geometries and measurement conditions.

The following spectral pre-processing methods were used in combination since they enhance the spectral information related to capturing the blend evolution and powder properties. They slightly changed compared to before, to enhance the predictive power for the developed models.

- When exporting the spectra, intermediate points are interpolated automatically by the software of the spectrometer, giving a resolution of 2 cm^{-1}. To avoid dealing with that unnecessarily large amount of correlated data, 8 measurement points were averaged again, restoring the range of 16 cm^{-1}. Thus, the final number of spectral points is 368.
- Performing a standard normal variate (SNV) of the spectra within the range of 10,000 – 4560 cm^{-1}. The cut-off at the low energy end of the recorded spectra was chosen to ignore the region where the optical fibers cut the signal.
- The region above 7226 cm^{-1} does not contain any of the constituents' chemical signatures, and was therefore neglected. This leaves the region of 7226 – 4560 cm^{-1} containing the (partly overlapping) specific bands of ASA and LM, used for further analysis.

A principal component analysis (PCA) was carried out to determine the differences between the calibration and in-line spectra.

Every spectral measurement of the calibration samples is represented in Figure 5.28 by a colored dot. Overall, the calibration samples are arranged in the form of an arch, ranging from 0% at the right end to 100% at the left end of the arch. Superimposed on this is a typical blending experiment with 50% (w/w) of LM on top of 50% (w/w) ASA.

These in-line measurements are represented by the line-connected points. Different measurement positions originated in different positions in the score plot, due to their different initial concentrations of ASA. However, they stay on the same curve as the calibration samples, and end up at 50% concentration of ASA, indicating that steady state was reached where all positions showed similar spectra. Moreover, the in-line measurements follow the same trajectory in scores on the arch as the calibration measurements. This means that the model was not affected by the difference in spectral acquisition.

However, the points representing the spectra measured in position 4 were slightly off the trajectory. Changing the position of the impeller made it clear that the deviation originated from the impeller blade which in this case was in front of position 4, as seen in Figure 3.3.

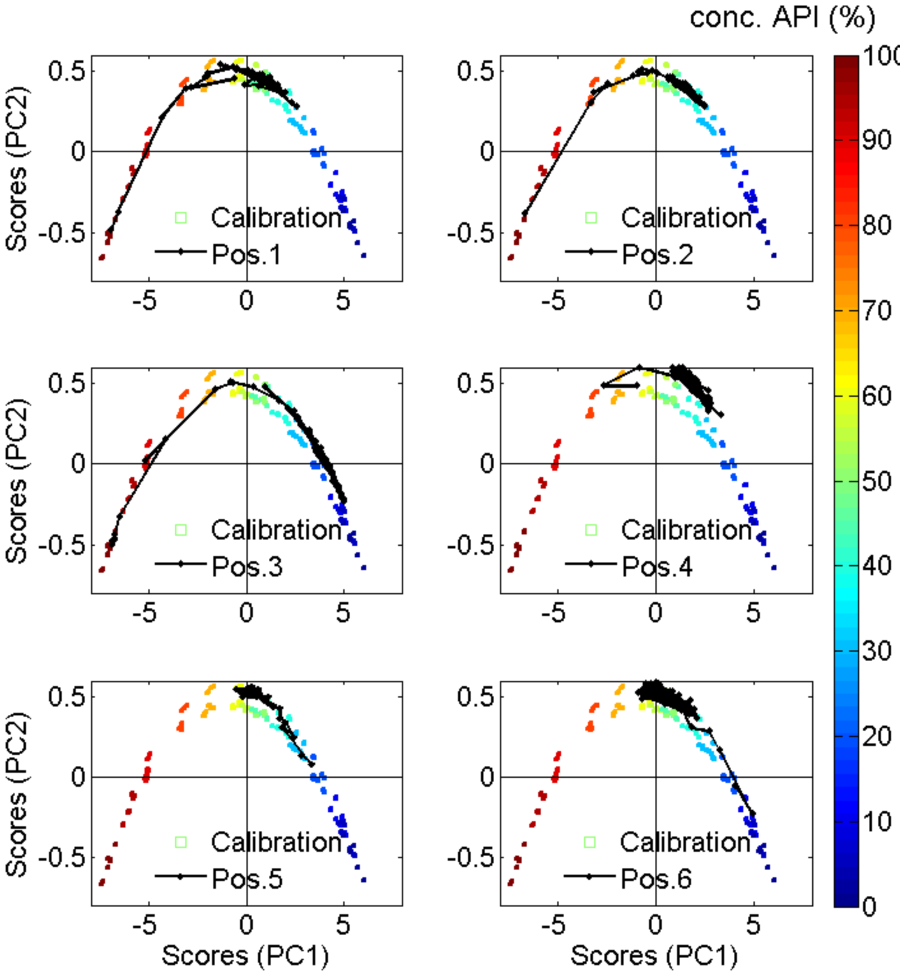

Figure 5.28: Score trajectory curve for the blending process. Calibration samples are represented by the colored dots. The black line represents the measurements during an actual blending process. The in-line measurements follow the trajectory of the calibration mostly.[9]

---

[9] With kind permission from Springer Science+Business Media: AAPSPharmSciTech, Monitoring Blending of Pharmaceutical Powders with Multipoint NIR Spectroscopy, 14, 2004, 234-44, Scheibelhofer et al., figure 3.

Calibration Based on Single vs. Multiple Probes

The multi-probe measurement system allows two different approaches for developing a predictive model:

- A model for every single probe (i.e., for each of the six measurement probes).
- A general model for all six probes which incorporates all calibration data of the different probes.

A distinct model for every position takes fiber-specific influences into consideration which can be everything in the light path, ranging from the fiber switch to the probe, including the unique bending of the fibers. In contrast, a general model incorporates all of these effects in one global model. Although the predictions may be less specific with respect to individual positions, this model is more robust since all the disturbances are accounted for and unknown but similar disturbances have little effect on the predictions.

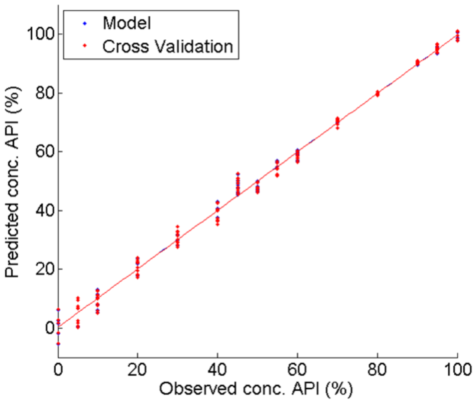

Figure 5.29: Observed vs. predicted plot of the PLS regression, including all positions. The red points represent the actual model, the blue points are obtained via cross validation. The best-fit line for both is plotted.[10]

The statistics of single-probe and general models are summarized in Table 5.2, an observed vs. predicted plot is shown in Figure 5.29. The models were based on

---

[10] With kind permission from Springer Science+Business Media: AAPSPharmSciTech, Monitoring Blending of Pharmaceutical Powders with Multipoint NIR Spectroscopy, 14, 2004, 234-44, Scheibelhofer et al., figure 4.

the same original data and consist of 2 PLS-components. The statistical summary for the regression models and the cross-validated models indicate that the single-probe models seem to perform better. However, the confidence intervals on the predicted values in the in-line experiments, as shown in Figure 5.30, indicate a different behavior.

For the calculation of the confidence intervals, it is taken into account, how good the PLS-models, based on offline spectra, can reflect the newly gained in-line spectra. Unexplained differences between in-line and offline spectra lead to a larger confidence interval. Hence, the confidence intervals give a more reliable estimation of the models' reliability.

A typical blending experiment predicted by the single-probe models and the general model is shown in Figure 5.30. As can be seen the confidence interval is larger in the single-probe models compared to the general model (with the notable exception in position 4, where the passing impeller influenced the measurement). A greater confidence interval typically suggests that there are unexplained differences between calibration and in-line measurements, leading to uncertainties in predictions. In our case, this may be due to the different bending of the fibers for calibration and in-line measurements. We therefore opted for the general probe model.

Determining Blending Dynamics, End Point and Homogeneity

In principle, two main questions arise during blending processes: (1) has the blending process reached its end point (i.e., can the blend quality be improved by further blending) and (2) is the blend homogenous?

Note that only a fraction of the whole powder volume was analysed, and thus the sum of all measurement positions does not have to be 100%.

To determine dynamics MBSD was used. Before employing it, a Savitzky-Golay Smoothing was applied to the predictions, with a window of 9 points and a second-order polynomial to minimize short-term fluctuations. A window size of 8 measurement points was chosen to calculate the MBSD as this reflects three times the volume of the standard dosage form (for a tablet of 6 mm in diameter and 3 mm in height).

For a blend to be considered homogenous, two requirements must be met. First, the concentration should be within the same level everywhere which can be

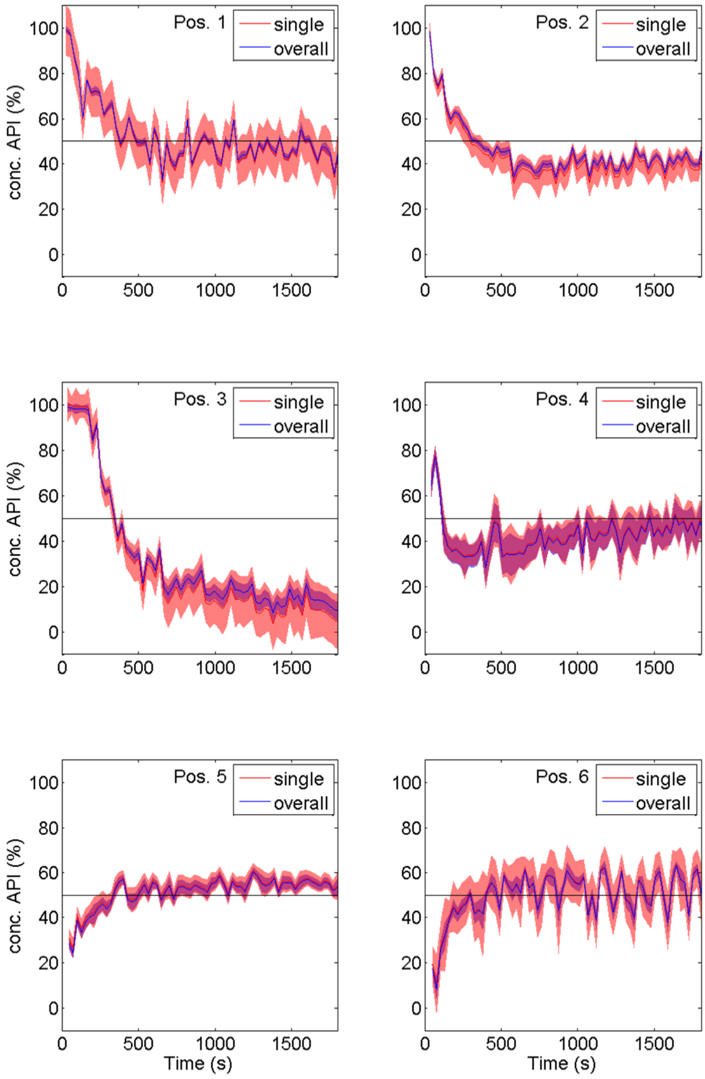

Figure 5.30: The same experiment predicted with the single probe and general models. The shaded area represents the 95%-confidence interval which is strikingly different for the applied models.[11]

---

[11] With kind permission from Springer Science+Business Media: AAPSPharmSciTech, Monitoring Blending of Pharmaceutical Powders with Multipoint NIR Spectroscopy, 14, 2004, 234-44, Scheibelhofer et al., figure 5.

	Slope	Offset (%)	RMSE (%)	R^2
Position 1	0.999	0.051	0.876	0.999
	1.001	-0.105	1.079	0.999
Position 2	0.998	0.088	1.334	0.998
	0.998	0.108	1.477	0.998
Position 3	0.996	0.196	1.985	0.996
	0.994	0.250	2.161	0.996
Position 4	0.998	0.105	1.456	0.998
	0.996	0.187	1.592	0.998
Position 5	0.998	0.103	1.438	0.998
	0.999	0.042	1.555	0.998
Position 6	0.998	0.120	1.553	0.998
	0.997	0.148	1.700	0.997
Overall	0.995	0.269	2.298	0.995
	0.994	0.270	2.407	0.995

Table 5.2: Summary of the model statistics for the single-probe calibration and general model. The first row of every pair gives the calibration statistics, whereas the second row gives the cross-validated statistics.

tested by directly comparing the spectra. Secondly, the predicted concentrations should be within the specification of the nominal concentration, according to the fractions filled into the blender, for which a valid prediction model is needed [83].

However, NIR is limited by the sampling position and only provides information regarding the surface region of the blend. Our investigation offered the opportunity to examine the blend in different positions at the bottom and on the side. As such, concentration in the different positions, especially in the vertical direction, could be monitored. However, we still cannot "look" inside the blend.

5.4.8 Different Blending Conditions

Replication experiments showed that the same dynamics were present inside the vessel under the same conditions, as will be presented in the next section. Thus, experiments were reproducible. In addition to that, the loading protocol of the vessel was varied in order to monitor the emergence of two blending regimes. Fast blending which was observed for low fill levels and near the impeller, was affected by segregation. Slow blending which was detected for high fill levels and far from the impeller, took longer to approximate the homogenous mixture.

Reproducibility of Experiments

Several experiments with the same composition and fill order were performed to investigate the reproducibility. 70 g of LM were loaded on top of 70 g of ASA (resulting in H/D = 0.35). Positions 1, 2 and 3 were at the bottom of the vessel, as shown in Figure 3.3. They were separated from the blade by a layer of powder. As can be seen position 3 was a critical location, as it was located directly at the edge of the vessel. Position 4 was on the side wall, at the height of the impeller blades which affected the measurement signals. The integration time of the spectra was optimized to reduce this effect, but it still resulted in a larger confidence interval at this position. Position 5 was above the blade and position 6 was slightly under the powder fill level.

Three runs with the same composition and fill order were performed to study the reproducibility of our setup. The predictions made using the PLS model are shown in Figure 5.31. Positions 1, 2 and 3 were at the bottom of the vessel.

As pointed out above, at the beginning of the experiment, pure ASA was at the bottom and in the lower part of the vessel (positions 1-4), whereas LM was in the upper part of the vessel (positions 5, 6). As can be seen in Figure 5.31 the API concentration decreased to approximately 50% (the final value for a perfect mixture) at positions 1 and 2 at the bottom of the vessel and seemed to reach a homogeneous state within roughly 500 s.

At position 3 in the corner of the blending vessel, the API concentration decreased as well. However, in 2 out of 3 experiments it reached a much lower value, while in the third experiment, just a slight decrease occurred. In addition, different experiments showed a different trajectory. Thus, some segregation occurred and powder seems to have stuck to the wall at these positions. Additionally, there were random events, e.g., when powder gets stuck and is removed again. Hence, these positions are critical for mixing and powder stuck to the wall should not be emptied into the processing container after blending, unless it is deemed negligible in amount. Note however that if a large amount of a specific material

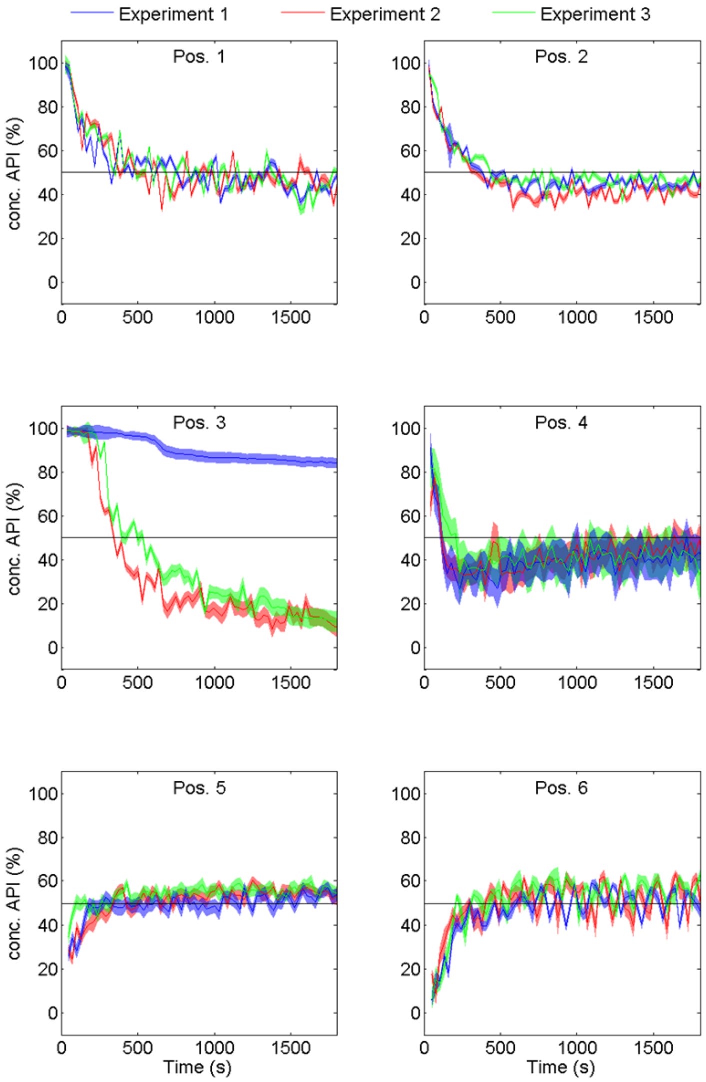

Figure 5.31: Monitoring a blending process, where initially seventy grams of LM was deposited on 70g of ASA.[12]

---

[12] With kind permission from Springer Science+Business Media: AAPSPharmSciTech, Monitoring Blending of Pharmaceutical Powders with Multipoint NIR Spectroscopy, 14, 2004, 234-44, Scheibelhofer et al., Figure 6.

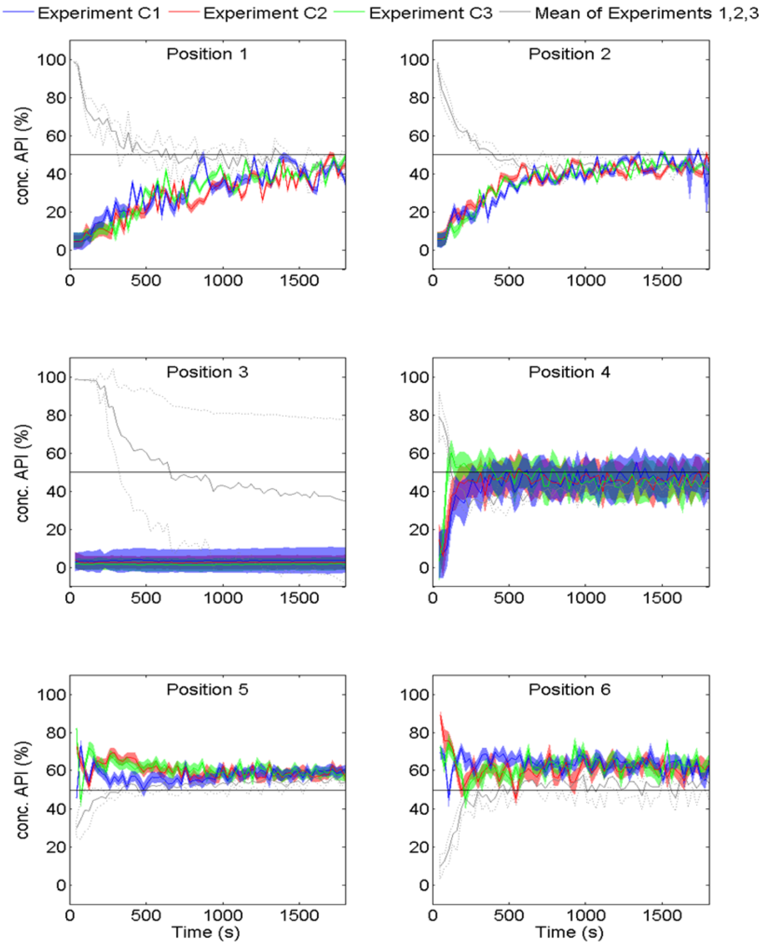

Figure 5.32: Monitoring a blending process, where initially seventy grams of ASA was deposited on 70g of LM. This is reversed compared to figure 5.31, whose mean concentration and standard deviation are shown by the gray lines.[13]

---

[13] With kind permission from Springer Science+Business Media: AAPSPharmSciTech, Monitoring Blending of Pharmaceutical Powders with Multipoint NIR Spectroscopy, 14, 2004, 234-44, Scheibelhofer et al., Figure 7.

selectively sticks to the wall (e.g., in small blenders with a high surface-to-volume ratio), the overall blend composition may be significantly affected.

Position 4 showed an interesting behavior, as it started with pure ASA. However, quickly LM concentrated at this position (overshoot) and it reached a final steady-state of about 50% only after many revolutions. This seems to indicate that ASA at the bottom of the vessel was pushed upwards by the blade, to the region above the blade, and trickled down afterwards. Positions 5 and 6 showed a decrease in LM and an increase in ASA concentrations. Position 6 which was the highest, showed a slower convergence to the nominal state. However, the convergence to the steady-state was faster at these positions compared to positions 1 and 2. Overall, the experiments show fluctuations in the order of 10% API in the range of 100 s. This was a real effect due to a small sample size but could be observed for the whole duration of the experiments.

Influence of Loading Order

Since the two materials showed significant differences in particle size and shape, variations in the mixing time and performance were expected, depending on the loading order. Therefore, experiments with reversed loading order, i.e., 70 g of ASA on top of 70 g of LM, were performed. They were repeated three times to test the reproducibility of the results. The results are presented in Figure 5.32.

As before, similar mixing dynamics were observed. However, there were some differences. For position 4 which was covered with LM in the beginning, the previously observed overshoot did not appear. The ASA was only transported down (and LM up). Moreover, the blending time until homogeneity in the lower part of the vessel was reached was significantly increased. In contrast, the mixing in the top part of the vessel was faster. For position 3 the deposition of powder was observed again.

As in the previous experiments, we observed that there was more than the expected concentration (i.e., 50%) of ASA in the upper half of the vessel and less in the lower part, indicating the segregation tendencies of the two-component system ASA and LM. However, in the latter experiments (ASA on top) the effect was slightly more pronounced. Long term dynamical studies should reveal if in both cases an identical final steady state could be reached. The times until a steady state was reached, estimated via MBSD, are summarized Table 5.3.

Choosing the loading order with ASA on top was favourable in terms of the required time. However, the reproducibility of the blending time was rather low. Further, homogeneity of the blend cannot be predicted based on the time it takes to reach the stationary state, as in different locations different steady states may exist, e.g., in the case of complete segregation. Therefore, the concentration levels must be monitored directly at various spatial locations.

The time to reach steady state was defined when all positions (except position 3 due to its location at the corner of the blender) were below the set level of 5% at the same time. The resulting times (see Table 5.3) provide estimates for the blending end point. As mentioned earlier, the estimated times until the stationary state was reached did not necessarily correspond with the overall homogeneity.

LM on ASA	Blending Time (s)	ASA on LM	Blending Time (s)
Experiment 1	441	Experiment C1	339
Experiment 2	472	Experiment C2	315
Experiment 3	414	Experiment C3	458
Mean	442 ± 29	Mean	370 ± 76

Table 5.3: Blending times for different loading orders, until steady state is reached.

Different Fill Levels

The amount of powder used in the above-mentioned experiments was always 140 g which corresponds to a fill level of H/D=0.35. To investigate the respective contribution of the convective and diffusive mixing mechanisms, the fill level was varied (H/D= 0.25 (80 g), 0.35 (140 g), 0.50 (200 g), 0.60 (250 g), 0.95 (400 g)). The height-to-diameter ratio is also shown in Figure 3.3. As for the vessel, diameter and height are the same and the H/D values are directly the fractions of volumes filled. Moreover, the fraction of ASA:LM was changed to 20:80, with LM on top. The loading order was not chosen in order to optimize the blending time, but to highlight the ASA transport within the powder bed. Clearly, the blending time increased with the fill level, as shown in Figure 5.33, which illustrates the mixing dynamics for position 2 at the bottom of the vessel. This position was chosen, since it clearly reveals the delay in reaching the nominal concentration. For every fill level, this position was covered by ASA at the start, and should reach the nominal concentration of 20% ASA.

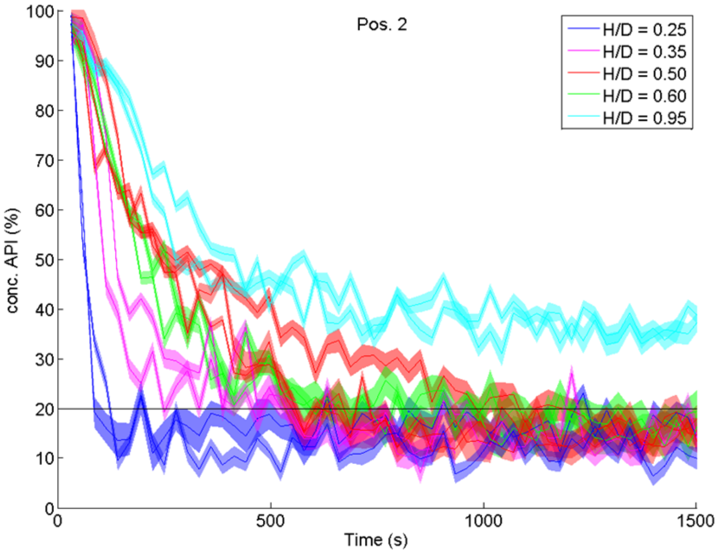

Figure 5.33: Concentration change over time at position 2, for experiments with different H/D ratios.[14]

The estimated blending times according to the MBSD methodology are summarized in Figure 5.34. A higher fill level resulted in a longer blending time. However, MBSD might not be suitable for this particular case since at high fill levels mixing and changes in the spectra are very slow. Therefore, if the same MBSD limit for all fill levels is used, the blending time for high levels may be underestimated.

Further it was observed that for a fill ratio of H/D = 0.5, the blending time varied unexpectedly, when compared to other fill levels. An additional third run was performed, but showed the same result. The reason for this unexpected behavior is not clear, and might be a result of a newly emerging powder flow pattern.

Of special interest is the experiment with H/D = 0.95, with blending occurring rather fast in the beginning, i.e., during the first 500 s. However, after that a state was reached with nearly no change in the API concentration, but far from the

---

[14] With kind permission from Springer Science+Business Media: AAPSPharmSciTech, Monitoring Blending of Pharmaceutical Powders with Multipoint NIR Spectroscopy, 14, 2004, 234-44, Scheibelhofer et al., Figure 9.

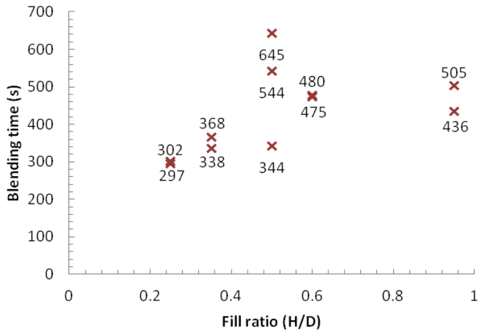

Figure 5.34: Blending times for different fill levels. Not surprisingly, a higher fill level leads to elongated blending time. Strange though, is the unanticipated behaviour for H/D = 0.5.

nominal value. The predicted concentrations are shown in Figure 5.35 for the measurement position 2 at the bottom and 4, 5, 6, 7, 9 on the side of the vessel (see Figure 3.3 for a geometrical sketch).

The different time scales of convective and diffusive mixing could clearly be observed. First, ASA was at the bottom of the vessel (positions 2 and 4). During the first minutes of mixing, ASA was transported into the upper regions of the powder bed, as evidenced by the decrease in concentration in positions 2 and 4. Respectively, positions 5 and 6 showed a significant increase in concentration. However, the probes at position 7 and 9 indicated no change in concentration. This can be interpreted as follows: ASA is first transported up in the powder bed due to the convective flow induced by the impeller. Then, in the intermediate region of the vessel, ASA particles are transported upwards due to a segregation mechanism that was already observed above. However, for segregation to occur the particle bed must be agitated, i.e., a certain fluctuation level of particles (i.e., diffusive motion) must occur. This is the case in a defined region above the stirrer, where an accumulation of ASA particles occurs (as seen in positions 5 and 6). However, in the top part of the vessel the bed is stagnant, and the granular temperature is very low. Thus, no accumulation of ASA occurs as can be seen in Figure 5.35. After 73000 s (approximately 20 hours), the concentration still failed to reach a steady state. Furthermore, the NIR probes at positions 2 to 6 showed a concentration above the expected value of 20% ASA since a large portion of pure LM was still accumulated in the upper part of the vessel and showed no noticeable mixing at all.

The edge of the mixing zone is roughly at position 7. Above this position very little mixing occurs. For a long time, only LM is seen by sensor 7. Concentration changes very slowly, indicating the slow movement of powder in front of the sensor at position 7. This is further backed by the large confidence interval which indicates a low moving speed. However, at a certain time point, concentration rises continuously within 2000 s to a different concentration level of about 90% ASA. As no rapid fluctuations can be seen, this might just be a volume containing mainly ASA crystals, passing directly in front of the sensor. The overall powder movement is very slow and the receptive area of the probe is just slightly larger than the mean crystal diameter. Hence we can just predict the concentration of LM and ASA in the small volume in front of the sensor, seeing the influence of stray crystals, if the movement of the powder bed is not sufficiently fast.

5.4.9 Conclusions

Our study presents a multiple-probe NIR setup for a lab scale blender. The interpretation of the spectra was performed using a chemometric model based on partial least squares regression. Calibration samples for the models were presented to the probes on a rotating disk. This eliminated the problems associated with calibrating inside the vessel. It proved to be a rather quick and easy way to ensure good calibration samples and dynamic measurements, while still reflecting the dynamic flow of powder inside the vessel.

The setup was suitable for monitoring slow blending processes, allowing us to scrutinize the powder-blending and segregation dynamics inside the blending vessel which is impossible with just a single probe. Segregation inside the vessel during the blending process was observed.

Moreover, we studied the emerging concentration gradient in the vessel which did not disappear with time. On the contrary, steady states were observed.

- Blending dynamics and time are different for different blender compartments. Thus, monitoring the blender with one probe alone does not provide a correct assessment of the blend quality. Alternatively, if only one sensor is available, e.g. for estimating the blending end-point, its position has to be chosen very carefully.
- The initial state has influence on the quality of the final blend. Initial variations, e.g. of the loading order, will have influence on the outcome and required time of a blending process.

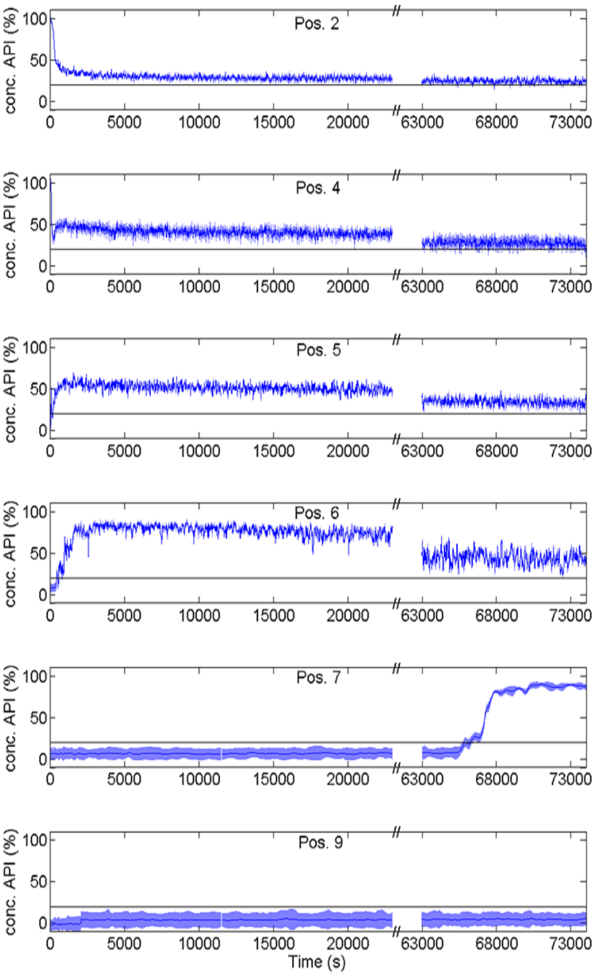

Figure 5.35: Example for a long term blending experiment lasting 20 hours. Whereas there is a large dynamic at the beginning, blending proceeds slower afterwards, and still has not stopped after 20 hours.[15]

---

[15] With kind permission from Springer Science+Business Media: AAPSPharmSciTech, Monitoring Blending of Pharmaceutical Powders with Multipoint NIR Spectroscopy, 14, 2004, 234-44, Scheibelhofer et al., Figure 10.

- Blending of a premix enables a quick estimation for the possibility of segregation during process steps.
- Material might get stuck at the wall and edges of the blending vessel which cannot be observed with traditional sampling techniques, as those always induce shear, thus breaking up such structures.

Developing a global model for all attached fibers and not separating the models makes the global model more robust and versatile. Moreover, by considering the confidence intervals of the predictions made via the PLS-model, additional information regarding the investigated processes was obtained.

The multiple probe measurements allow a detailed analysis and understanding of powder mixing processes by gaining spatial information of the local powder concentration. For example, we demonstrated how loading order of the investigated materials resulted in different blending dynamics. Furthermore, increasing the fill level affected the mixing dynamics, by creating different zones where different mixing effects dominate, i.e., convective and diffusive mixing. Multi-probe NIR monitoring allows the detailed monitoring of these spatial mixing dynamics.

Multiple measurement positions open up yet another possibility for determining the blending end-point. As opposed to comparing subsequently taken spectra, spectra at different positions can be used to calculate the standard deviation. Hence, it is possible to find the time point, when a stationary state is reached. Compared to traditional thief sampling, the advantage of the presented method is that there is no interference with the blending process itself of any kind. Nevertheless, as a drawback samples can only be taken at the interface of blend and vessel. Additionally, it is important to place probes at locations where sufficient powder movement is obtained, as the sample volume of the NIR probe is small, and a single stagnant crystal may bias the results. That is, a stagnant well-mixed area may be falsely reported as being demixed.

In summary, monitoring by multiple points showed that single-point measurements with NIR could lead to misinterpretations of the entire blending process. Hence, it is essential to choose a proper position – and even better multiple positions - when monitoring blending processes.

5.5 Continuous Blending Process

5.5.1 Introduction

Continuous blending is especially useful for the production of a low amount of especially. The quality of the blend, produced by a continuous blender is strongly influenced by the quality of the dosing feeders controlling the input of the blender. The only remaining set-point that could influence the homogeneity of the blend, despite different blender geometries, is the rotational speed of the impeller inside the blender. Other possible parameters are predetermined by production settings, as the substance ratios and throughput.

In the end, the describing quantity is the residence time distribution of the material inside the blender. The broader the residence time distribution, the more impeller passings were experienced by the material, leading to a more homogeneous blend. However, dependent on the throughput and mixer geometry, a higher rotational speed may either lead to a broadening of residence time, as the flow pattern becomes more chaotic, or to a shortening, as the material leaves the blender faster [64, 66, 67, 148–150].

5.5.2 Preparation Steps

In the presented case, basic requirements on the blender, regarding substance properties and throughput settings were defined beforehand. The fulfillment of those requirements, the quality of the blend, i.e. homogeneity, and the effect of various settings should be determined by NIRS.

To successfully determine the concentration and homogeneity at the continuous blender, several preparation steps were necessary.

- For interpretation of the spectral data, chemometric models were built offline, and validated at the blender with preblended material. Again the set-up including the turn-table was used.
- The penetration depth into the blends was determined, as described in section 5.2. This is necessary to determine the sample volume, and hence the scale of scrutiny on which homogeneity is tested. Measurements with NIR usually sample a smaller volume, and thus show larger fluctuations, than is defined in the requirements. Hence, the experimentally determined homogeneity has to be corrected for the desired depth of scrutiny.

- The mass flow leaving the blender was determined via a dynamic balance. Furthermore the particle speed at the blender inlet and outlet was determined with the aid of a high speed camera, again in order to determine the sample volume.

5.5.3 Experiments at The Blender

The multiprobe setup was used in the following to categorize the blender. An experimental design was created to systematically vary the factors of throughput, concentration, and impeller rotational speed. The resulting design is visualized in Figure 5.36.

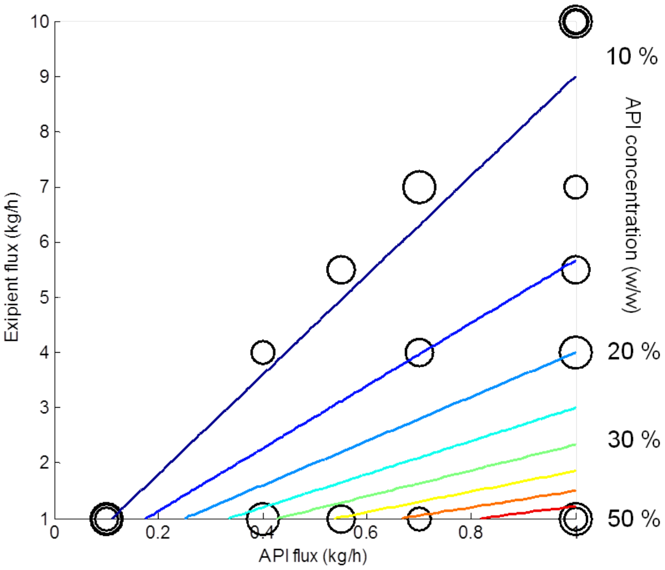

Figure 5.36: Scheme of the experimental design for testing the blender. The axis represent the mass flow of the two ingredients. Accordingly, the relative fraction is indicated by the colored lines. The circles represent testing points, whereas the varying circle size reflects the different rotational speed settings of the blender.

For measuring during the blending process, fibers were placed at the inlet ports of the blender, at the outlet, and/or on a conveyer belt placed after the outlet. A

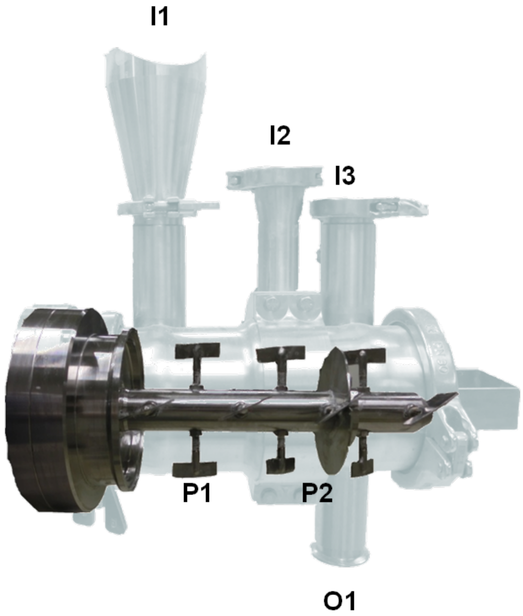

Figure 5.37: Illustration of the blender, by composition of several photographs. The impeller is shown opaque, and the hull of the blender translucent. I1, I2, I3 are different inlet ports, O1 names the outlet port, P1 and P2 are positions of a weir, to dam up material.

sketch of the blender is shown in Figure 5.37, and the acquired data in terms of mass and concentration during a blending run can be found in Figure 5.38.

Figure 5.38 immediately reveals several facts:

- Between the start of feeding, as seen by the NIR-probe at the blender entrance, and the blender outlet, time elapses. This time lapse is determined by the material throughput and blender speed, and describes the amount of time necessary for the powder to progress through the empty blender. Furthermore this allows an estimation of the amount of material residing inside the blender.
- Deviations in concentration are larger at the inlet than at the outlet. This is a direct effect of homogenization of the powder inside the blender. This ratio is sometimes used for describing the blender [64].
- The concentration level at the inlet and at the outlet does not agree. The outlet concentration was ultimately confirmed by taking samples and per-

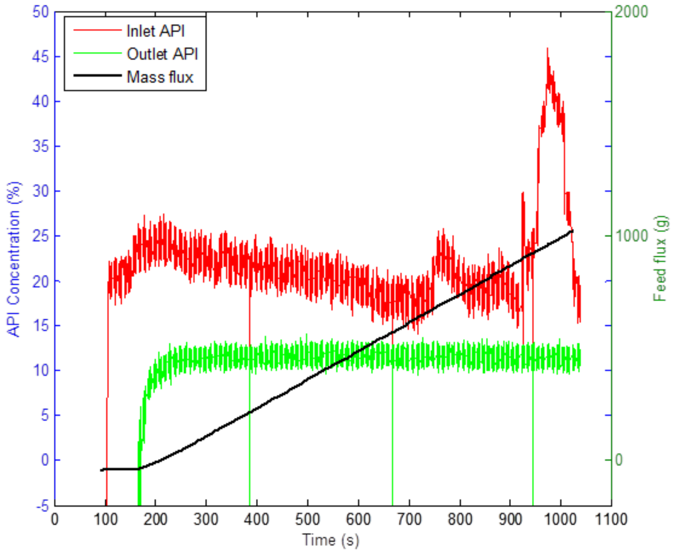

Figure 5.38: Measurements acquired during a typical blending run. Shown are the cumulative mass leaving the blender, as determined by a balance at the outlet, and the API concentration at the blender inlet and outlet, gained by NIR spectroscopy.

forming HPLC analysis. The deviation at the inlet is caused by two main reasons: (a) Dust development at the inlet led to a cloaking of the NIR probe. (b) The powder stream at the inlet is not blended, but just a parallel stream of two feeders, which leads to a different measured concentration levels dependent on the point of view of the NIR probe.

The quality of the blender was assessed using two different strategies:

1. When determining the concentration at the output of the blender, variance and hence homogeneity can be determined. As the output should be stationary, random samples over time were chosen and the variance calculated.
2. By simultaneous measurement at the input and outlet of the blender, and feeding a step function, the residence time distribution inside the blender was calculated.

5.5.4 Conclusion and Remarks

Hence, by performing the number of runs according to the experimental design, the factors determining the hold-up time and mass inside the blender, and the homogeneity regarding mass flow and API concentration could be determined. This was done by multiple linear regression, which also allows to calculate a confidence interval for the factor coefficients and hence a decision about the significance of the individual factors.

For assessing heterogeneity, the Coefficient of Variation (CoV) was used. Its value could be modeled with a quality of $R^2 = 0.78$, and the resulting response plot, showing the expected CoV for different settings, is shown in Figure 5.39.

It could be ensured that the quality of the blend is sufficient. However, only rotational speed showed a significant influence on the homogeneity. Counterintuitively, a lower rotational speed leads to improved homogenization behavior. Hence, the longer residence time of the material inside the blender outweighs the slower movement, leading to better mixing.

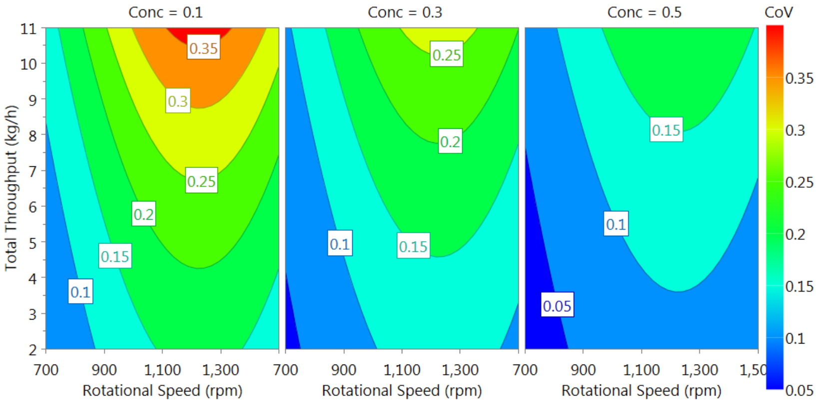

Figure 5.39: Contour plot of the Coefficient of Variation (CoV) for different settings. Total throughput and concentration range are predetermined by the process; rotational speed can be varied. The lowest CoV and hence best mixture quality is found at lower rotational speed of the blender.

For a more detailed description of the experimental design, the set-up and the following analysis, the reader is kindly referred to the bachelor thesis of G. Weber [151], who gives a detailed account therein.

A next endeavor is to measure inside the blender, in order to evaluate the development of the blend quality along the blender axis. However severe window fouling prohibited the acquisition of exploitable data inside the blender.

5.6 Window Fouling in A Coating Process

5.6.1 Introduction

Sample presentation and spectra acquisition greatly influences the quality of the obtained spectra, complicating or disabling model building. Hence, effort has been made to apply the theory of sampling [152] to near-infrared probes and to present specimen accurately [27, 153, 154].

Especially, window fouling remains a severe issue (i.e., substances sticking to or even growing on the sensor window, preventing an accurate measurement). This happens during different processes and depends on humidity, the processed material's attributes, geometry and operating conditions. Once established, fouling becomes persistent, and thus, must be prevented for accurate measurements [155, 156].

A variety of physical counter-measures has been developed to prevent window fouling. A looking window in a suitable position that is not affected by fouling, can serve as a suitable interface, as demonstrated in [157]. Clever design of the apparatuses and the enclosed air and material streams can prevent window fouling. [158].

A common method is to introduce a probe-cleaning mechanism (e.g., by wiping) or at least to clean the probe in a regular interval. For example, Green et al. proposed an air purge to clean the probe window [159]. A more complex approach is to use a probe retracting mechanism (e.g., the Lighthouse Probe™ by GEA Pharma Systems, Belgium) and to clean the probe with solvents and wiping [160–162]. Additional strategies, e.g., the application of non-adhesive films [163] and more, exist.

For the process investigated in this study, a hot-melt coating process in a fluidized bed, such possibilities were considered and, for specific reasons, dismissed. Specifically, the process deals with lipid coating of substrate crystals, and the intention is to estimate the amount of lipid coating on substrate crystals. The system design and the process conditions lead to severe window fouling. Due to the temperature sensitivity of the lipid, heating of the probes was not an option. Moreover, since no solvent is used in the actual process, introducing one for cleaning the probe was not desired, as this might led to contamination. Furthermore, using an air purge would disturb the sensitive air flow pattern of the fluid-bed system. Finally, because several NIRS probes are applied simultaneously inside the fluidized bed as a strategy to perform three-dimensional process analysis, there was limited space for cleaning devices.

Thus, a post-measurement strategy was required. The proposed mathematical method of correcting for window fouling is founded on physical first principles. As a prerequisite, Extended Multiplicative Signal Correction (EMSC) [98] is used to split the spectra into different parts. The obtained coefficients are further used to estimate the distance to the substrate crystals. Thus, these signal parts provide the basis for correcting for window fouling. Although limited to certain applications, the proposed method will allow accurate monitoring of complex fluid-bed processes.

5.6.2 Experimental Setup

Hot-melt Coating

The process under consideration was a hot-melt coating process in a fluidized bed. The coating process followed a precise sequence. The carrier material was introduced into the hot-melt coater and a fluidized bed was established. The product temperature was 55° C. The molten coating, a lipid, was sprayed into the fluid bed at a certain rate. The pump-head temperature and spray-air temperature were set to 95° C which ensured a stable process and sufficiently homogenous coating of the substrate crystals. As a side effect, the probe window was covered with the coating material too, i.e. fouling occurred.

The recrystallization temperature of the molten lipid is between 69-74° C, and the process temperature was slightly lower. Since the lipid used as coating has a freezing point slightly below the feeding temperature, it solidified on contact with the substrate material. Its behavior was plastic in the solid state. It was not abraded off the surfaces by the moving crystals, showing a high sticking capacity on most surfaces of the experimental pilot set-up.

Measurement Equipment

The spectrometer prototype, EVK Helios EyeC Multiprobe Spectrometer, was used to monitor the process, with a frequency of 105 Hz. Every spectrum had an illumination time of 1.5 μs. The probes were placed at different parts in the coating equipment, and observed different levels of fouling. To find a location suitable for process monitoring, several probe positions inside the vessel at various heights and looking in different directions were tested. In the end, the combined information of three well-placed probes can be used for online evaluation of the process state. A more elaborate comparison of the investigated positions can be found in [164].

After every 5.3 s, a pause of 8.3 s was used to empty the computer memory. This procedure resulted in about 60,000 spectra in 30 min process time.

Overview of Data Handling

When the process was started, spectra were recorded and saved with a timestamp. Further treatment and calculations happened after the end of the process:

- Calculating the absorbance spectra by using the white and dark references.
- Cropping the spectra to the wavelengths of 1000-2100 nm.
- A median filter over 30 nm was used for the spectra to enhance signal to noise ratio.
- All spectra with a mean absorbance level above 1.0 were disregarded, since no or insufficient reflected light was collected to perform feasible EMSC which would lead to erroneous results.

Further EMSC was performed independently for each time step. With the parameters obtained by EMSC, the proposed procedure for fouling correction (described in the next section) was applied.

5.6.3 Spectral Interpretation

Physical Background

According to Beer-Lambert's law (see equation 2.12) the absorbance A is given by the negative logarithm of the ratio of the collected intensity I (by transmission or reflection) and the reference intensity I_0 (when no sample is present or a totally reflecting white background is observed, respectively). This absorbance is a result of the specific absorptivity of the investigated material, multiplied by its concentration c and the optical path length d in the material. As such, if not known by other means, the path length and the concentration cannot be separated by spectroscopic means [92].

In order to measure the coating mass on the crystals by absorbance, a regression model can be established and the growth of the coating layer during the process can be determined. However, *a priori* it is not possible to distinguish between coating on the crystal surface and coating on the sensor window, as it is the same substance. Moreover, large variations between consecutively acquired spectra exist.

As can be seen in Figure 5.40 the most prominent change in spectra is a large baseline shift. The standard approach (and often a good choice) is to use a spectral transformations and to average consecutive spectra which leads to clearer spectra with less noise. Nonetheless, averaging consecutive spectra over a pre-defined process time window results in the loss of short-time sensitivity related to process and measurement variations.

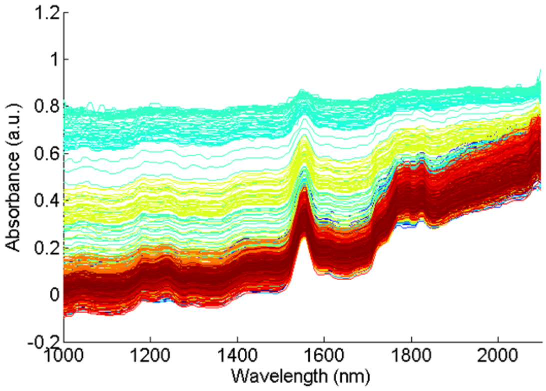

Figure 5.40: Some of the spectra acquired throughout the coating process. A prominent change in offset and peak heights can be seen.[16]

Due to the short illumination time, and the small detection area of the bifurcated fibers, just one or at maximum a few crystals pass the field of view of the sensor during the acquisition of a single spectrum. Fast captured spectra include the distance-information of the crystals and avoid averaging out these differences over time. If several instead of a single crystal pass through the probe's field of view during spectral acquisition, the mean distance of those crystals still differs from one spectrum to the next. To perform this work, there are several requirements: powders have to be able to be fluidized, to form a fluidized bed with a large

---

[16] Reproduced from Scheibelhofer et. al., Journal of Near Infrared Spectroscopy, Pharmaceutical Special Issue, 2014 (in press). Copyright IM Publications 2014.

percentage of voids. In addition, a sufficient amount of material has to be present in front of the sensor to obtain a strong signal and good signal-to-noise ratio.

Thus, a distinction can be made between the window and crystal coating. This, however requires understanding of the spectral effects. Specifically, the measured absorbance $\boldsymbol{a}_{\text{measured}}$, which is noted down as a vector, as it contains a series of wavelengths, can be split in several parts:

$$\begin{aligned}\boldsymbol{a}_{\text{measured}} &= \boldsymbol{a}_{\text{coating on substrate}} + \boldsymbol{a}_{\text{material of substrate}} + \\ &+ \boldsymbol{a}_{\text{distance to crystal}} + \boldsymbol{a}_{\text{coating on window}} + \boldsymbol{a}_{\text{residual}}\end{aligned} \tag{5.16}$$

In equation 5.16 a substantial part of the absorbance stems from the substrate material $\boldsymbol{a}_{\text{material of substrate}}$. The contributions of the coating material $\boldsymbol{a}_{\text{coating on window}}$ and $\boldsymbol{a}_{\text{coating on substrate}}$ have the same wavelength dependence since they originate from the same substance.

The distance-to-the-crystal particles contribution has several effects. In general, the air between the probe window and crystals does not have a notable influence on the measured spectra. However, as the illumination and detection fiber of the probes are placed next to each other, and the cupped fibers have a certain aperture, light intensity is lost. Hence, if a substrate particle is far away, less light reflected by the substrate crystals is detected; as is sketched in Figure 5.41. This leads to a high baseline of the calculated absorbance (or pseudo-absorbance) and comparably weak absorbance bands of substrate and coating material. In Figure 5.41, the left peak in the sketched spectra corresponds to substrate material; the right peak corresponds to coating material. In the top row particles are close to the NIR probe and absorption peaks are clearly visible. In the bottom row particles have a larger distance to the NIR probe. The absorption peaks are less intense, but high baseline absorption can be found. On the left side of Figure 5.41 coating is only on the particles, but the probe is clean. Thus, the relative height of substrate and coating material peaks are in a fixed ratio. On the right side also the probe window is coated. Thus, the height of substrate and coating material absorbance do change their ratio as more of the signal is absorbed by the window. This establishes the basis of the developed method. In our case, at a distance of more than roughly 0.5 cm, a single crystal is not detected any more.

Finally, the residual may contain the spectrometer drift, unconsidered substances, stray light and other effects. Spectral transformations, including standard normal variate (SNV) or Kubelka-Munk transformation are regularly used to remove such effects, e.g. sample distance, from spectra and hence reduce spectra to contain only chemical information [95]. In contrast, here we use this very information of sample distance contained in the spectra.

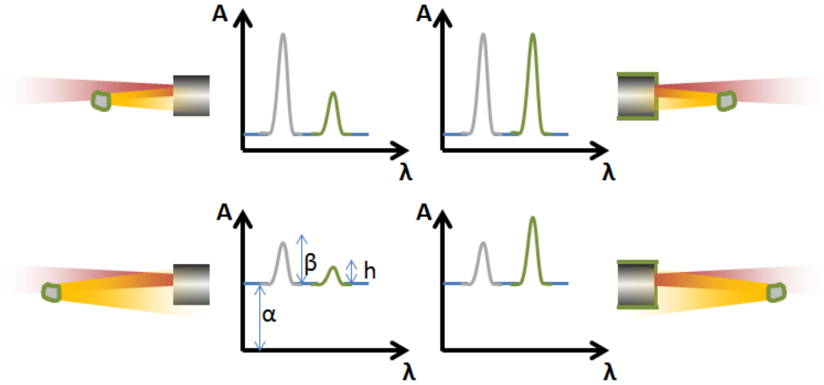

Figure 5.41: Sketch of probes (gray) and particles (grey with green coating) at different distances, and the effect on the recorded spectra. Gray peaks in the spectra represent the substrate materials, and green peaks the coating material. In the lower left graph, the parameters as used in equation 5.17 are indicated.[17]

Spectral Decomposition with EMSC

To split up the measured absorbance into the parts described in equation 5.16, we adopted the method of extended multiplicative signal correction (EMSC) [98, 165, 166]. The method was already explained in section 2.3.1, and is used here in the form

$$\boldsymbol{a}_{\text{measured}} = \alpha \cdot \mathbf{1} + \beta \cdot \boldsymbol{a}_{\text{substrate}} + h \cdot \boldsymbol{a}_{\text{coating}} + \delta \cdot \boldsymbol{\lambda} + e \cdot \boldsymbol{\lambda}^2 + \boldsymbol{R} \tag{5.17}$$

The constituents of $\boldsymbol{a}_{\text{measured}}$ represent different physical contributions. $\mathbf{1}$ was set to be a constant additive value for all wavelengths and primarily reflects the influence of the crystal distance. A high value of α corresponds to a larger distance of the particles. $\boldsymbol{a}_{\text{substrate}}$ is a typical spectrum (taken offline) of pure substrate material. Therefore, if substrate particles are near the probe window, and give an intense absorption spectrum, β is high. Since α and β depend both on particle distance, they show a correlation, as is shown in Figure 5.42.

---

[17] Reproduced from Scheibelhofer et. al., Journal of Near Infrared Spectroscopy, Pharmaceutical Special Issue, 2014 (in press). Copyright IM Publications 2014.

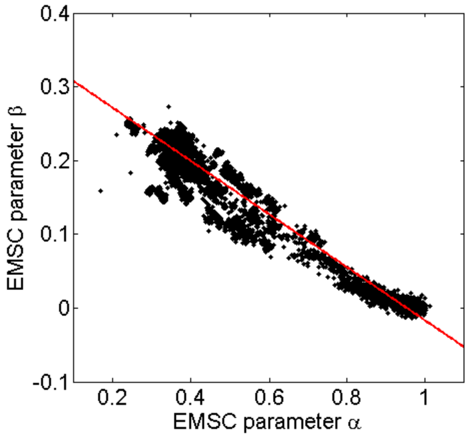

Figure 5.42: EMSC parameters α and β during a coating process. Both are dependent on the particle distance, and hence show a strong correlation.[18]

$\boldsymbol{a}_{\text{coating}}$ describes the coating spectrum on the crystals. It was obtained by taking offline-spectra of the samples collected during the coating process. A principal component analysis was performed, and the loadings of the first component, representing the coating, were taken. Unlike a pure coating sample, this takes into account the matrix effects of the crystal substrate material.

$\boldsymbol{\lambda}$ and $\boldsymbol{\lambda}^2$ represent linear baseline offset and curvature. $\boldsymbol{\lambda}$ is a vector ranged from -1 to 1, with the number of measured wavelengths defining the number of elements. $\boldsymbol{\lambda}^2$ is the element-wise square of this vector. Therefore, the parameters δ and ε can correct for the curvature of the spectra that was caused, for example, by an outdated background measurement.

As the cropped spectra consist of 175 elements, the scalar parameters $\alpha, \beta, h, \delta, \varepsilon$ are overdetermined and estimated using a classical least squares algorithm, for every time step independently. $\boldsymbol{R}$ is the residual which is the difference between the sum of the constituents and the actual measured spectra. Hence the length $||\boldsymbol{R}||$ must be minimized in the least squares method. Furthermore, it serves as a parameter indicating the overall quality of the least squares fit. A different structure of a measured spectrum would lead to an unexpectedly large $||\boldsymbol{R}||$.

---

[18] Reproduced from Scheibelhofer et. al., Journal of Near Infrared Spectroscopy, Pharmaceutical Special Issue, 2014 (in press). Copyright IM Publications 2014.

The obtained parameters provide valuable information regarding the process. This is shown in Figure 5.43. The parameters α and β are fluctuating randomly within a certain range. This reflects the varying distance of observed crystals. While for parameter α no long-term trend can be observed, the mean of parameter β shows a growth with time. The origin of this effect will be explained later. At the beginning of the process, the fluid bed was not fully established yet, most likely leading to a direct contact of the particles with the probe, resulting in the peak at process start.

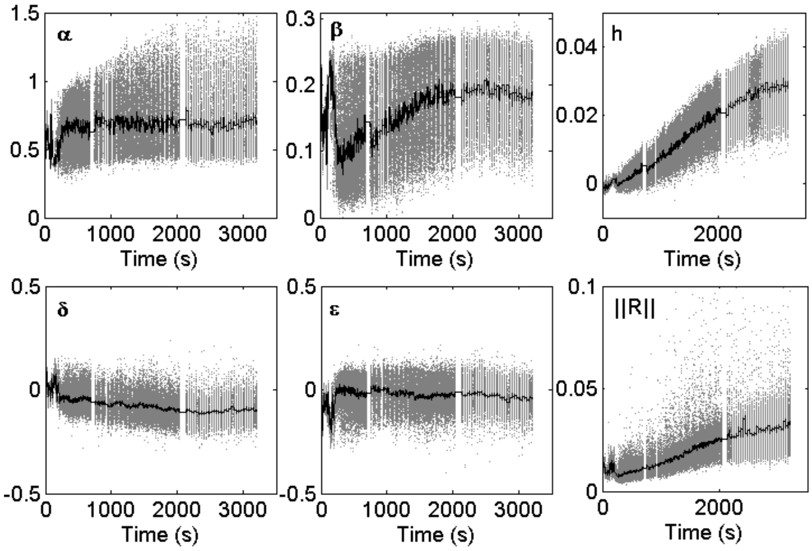

Figure 5.43: The obtained EMSC parameters over the coating process. The dots mark individual measurements and the black line is a moving mean over 1 s.[19]

By examining the parameter h, the amount of coating in the field of view of the probe can be estimated. However, as the coating spectra are the same on the crystals and on the window, it is impossible to distinguish between these two contributions yet.

The parameter δ shows a certain trend over time which might be related to a slight shift in the background, connected to temperature changes in the measurement set-up, or changes in the physical appearance of the investigated material. Parameter ε does not show any trend. It is important to test if δ and ε are smaller

---

[19] Reproduced from Scheibelhofer et. al., Journal of Near Infrared Spectroscopy, Pharmaceutical Special Issue, 2014 (in press). Copyright IM Publications 2014.

than the sum of α, β, h (with all the $\boldsymbol{a}$'s normalized). If this is not the case, the underlying corrections would be considered unrealistic. Although the residuals also increase with time, they were very small, compared to the total sum of a squared spectrum (>10), which confirms that above assumptions are valid.

Compensation for Window Fouling

The difference between the coating on the sensor window and that on the substrate particles is: the former is visible at all times, while the latter just appears when there is a substrate particle in front of the sensor. As particles pass by the probe window at different distances, the parameter of coating h varies. However, since the distance is also indirectly "measured" by the contribution of the crystal material, one can distinguish between the contribution by crystal coating or window fouling. Thus, there must be an additional term included in h for the window coating which is influenced less by the distance to the crystal. Ideally, only fouling would be observed when no crystal is present (i.e., when $\beta = 0$). In practice, for reflected light to be detected a crystal must be in front of the sensor since the coating on the sensor window is not opaque or thick enough to act as a sufficient reflector. The spectral signal-to-noise ratio in that case is insufficient for an accurate EMSC parameter estimation. As such, these spectra have to be excluded from the analysis.

By plotting parameter h against parameter β, we observe, as expected, an increase of h with β. It is now possible to represent the parameters as

$$h = h_{\text{coating}} \cdot \beta + h_{\text{fouling}} \tag{5.18}$$

where h is still the coefficient obtained by EMSC; h_{coating} originates from the coating on the particles and is directly proportional to β since the substrate shows the same effect of distance (as indicated in Figure 5.41) and h_{fouling} represents the window fouling. When the probe is clean, the line passes through the origin ($\beta = 0, \quad h_{\text{fouling}} = 0$), where no coating and no substrate material is observed. However, as the amount of coating on the window increases, this line moves towards a higher h_{fouling} value, indicating the presence of coating without a crystal, i.e. window fouling.

Figure 5.44 shows a whole coating process in terms of the parameters β and h. Every spectrum corresponds to a single point in this parameter space. To correct the crystal coating analysis for window fouling, the following strategy was adopted: For spectra with $\beta < 0.1$, which indicates that the substrate crystals are far away, the moving mean for β and h over 60 spectra (equivalent to 0.57 s) is calculated. For spectra with $\beta > 0.2$, which represent close-by crystals, again a moving mean over the coefficients is calculated (indicated by the black lines in Figure 5.44). The spectra between $\beta = 0.1$ and 0.2 are neglected. Those two moving means are then used to determine h_{coating} and h_{fouling} according to equation 5.18.

When interpreting equation 5.18 as a straight line, the offset in Figure 5.44 represents the part of the coefficient h due to window fouling, and the inclination the part due to the crystal coating as shown by the dashed line. For convenience, h_{fouling} is the inclination times 0.22 (the mean β value for all $\beta > 0.2$) in order to preserve the size of the original coefficients.

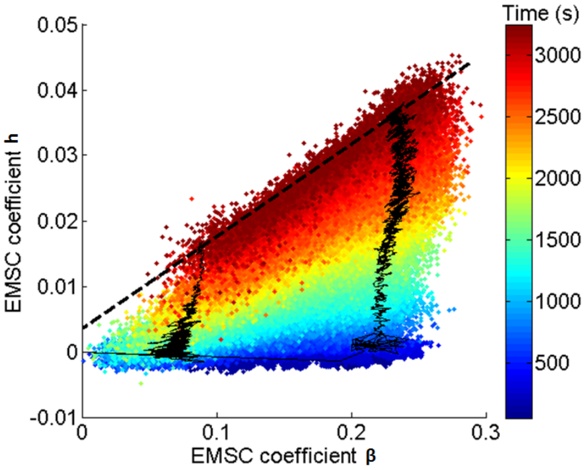

Figure 5.44: EMSC parameters h over β during a coating process. Every point represents a recorded spectrum, and color is chosen according to process time. In the beginning of the process, no coating is visible, only crystals at different distances (lower blue part of the data). With time passing, increasing coating becomes visible, as indicated by the shift of the data points in the ordinate direction. On the right side of the figure this trend is clear. It shows the superposition of coating on the pellets and the probe window. On the left side, the coating on the probe window is dominant and the pellets and their coating appear fainter to the sensor. The black lines represent the moving means for low β and high β values (both start at zero.) The dashed straight line represents equation 5.18 at the end of the coating process.[20]

---

[20] Reproduced from Scheibelhofer et. al., Journal of Near Infrared Spectroscopy, Pharmaceutical Special Issue, 2014 (in press). Copyright IM Publications 2014.

To confirm this interpretation, two preliminary experiments were conducted. First, a process without any coating was performed (Figure 5.45). The coefficient β which represents the crystals, varied strongly according to the changing crystal distance. The coefficient h which represents the coating, is scattered around zero. No trend with time is observed.

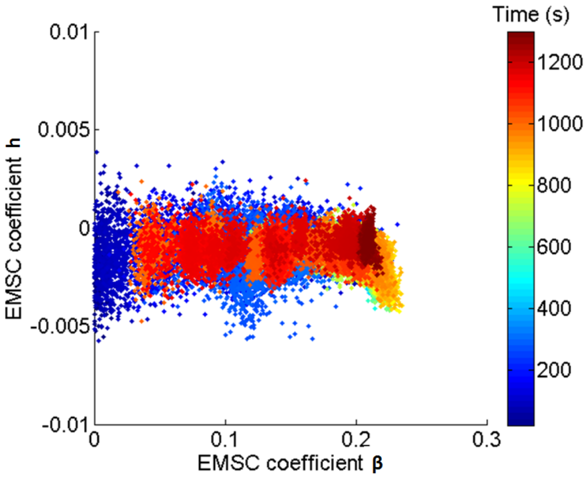

Figure 5.45: The obtained EMSC parameters β and h for a process where no coating was applied. Whereas the change in β still reflects the varying particle distance, h is distributed around 0 during the whole process, as no coating is seen.[21]

Second, samples collected during various intervals in the coating process were analyzed offline. Therefore, it is guaranteed that the probe window is free of coating (Figure 5.46). The spectra were recorded at varying positions with respect to the samples. When fitting a straight line through the coefficients obtained via multiple measurements of one sample (i.e., one defined coating thickness), the intercept at the y-axis is close to zero, and does not follow any trend.

To further confirm that the correction procedure for the amount of coating delivers correct results, offline samples (with a clean probe window) and inline measurements (with gradual window fouling) are compared from several experiments and time steps. The data treatment is exactly the same, except for the fouling correction, and the corrected (h_{coating}) and uncorrected coefficients (h) are compared in Figure 5.47. The corrected coefficients show a much better

---

[21] Reproduced from Scheibelhofer et. al., Journal of Near Infrared Spectroscopy, Pharmaceutical Special Issue, 2014 (in press). Copyright IM Publications 2014.

agreement with their offline counterparts than the uncorrected. Additionally, variations in the corrected coefficients are much smaller, indicating that the effects of different probe positions, and hence fouling behavior, are corrected for.

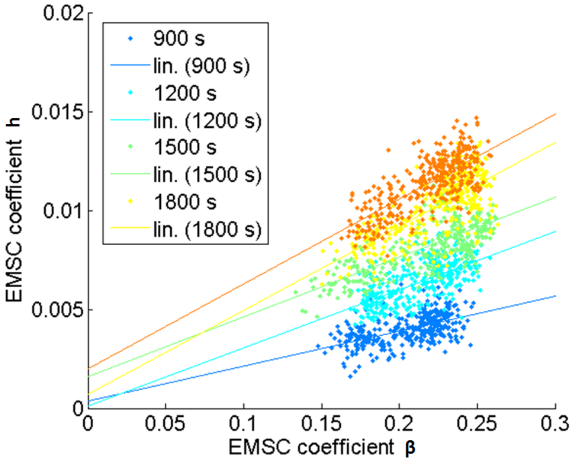

Figure 5.46: The obtained EMSC parameters β and h for samples measured offline. β and h show the same correlation as on-line. Points represent individual spectra and lines a linear fit for the respective time window.[22]

As the coating forms a shell around the crystal, geometry factors must be taken into account to establish a connection between the coating mass, measured by NIR, and coating thickness which is the true "critical quality attribute" [132]. The substrate particle size in our case was 250 μm Feret diameter, and the desired coating thickness at the end of the process was 40 μm. For several runs, these values were confirmed based on microscopic images obtained with a Leica DM 4000 microscope equipped with a Leica DFC 290 camera. This allows to establish a relationship between the absolute coating thickness and the value of $h_{\text{coating}}(t)$.

An automated script can now handle these corrections, and further work will focus on the actual observation, state estimation, control of the fluid bed and testing its general purpose.

---

[22] Reproduced from Scheibelhofer et. al., Journal of Near Infrared Spectroscopy, Pharmaceutical Special Issue, 2014 (in press). Copyright IM Publications 2014.

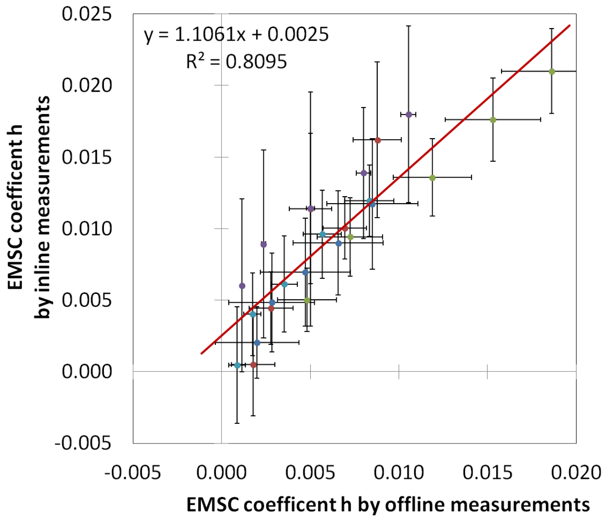

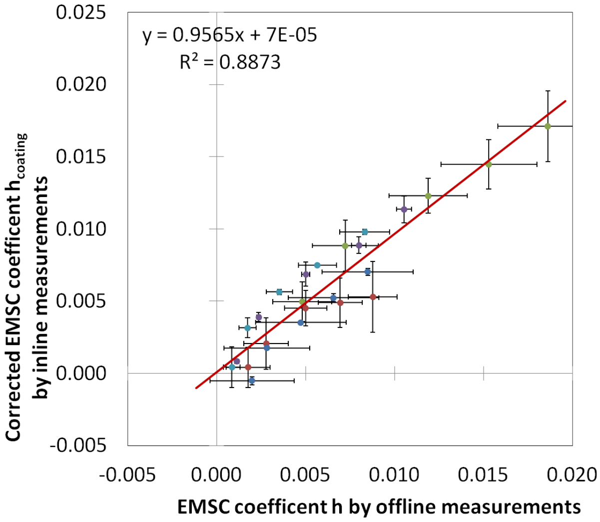

Figure 5.47: Comparison between off- and in-line measurements. The upper and lower figures show the coefficients without and with correction for fouling, respectively. Different colors indicate different batches, the error bars are standard deviations for measurements in different positions in the vessel (inline) and the thieved samples (offline). The statistics of the regression line are in the top left corner. The corrected coefficients are in better agreement with the offline samples. Furthermore, the deviations in different batches are reduced, indicating that window fouling is not the same for every batch and position.[23]

---

[23] Reproduced from Scheibelhofer et. al., Journal of Near Infrared Spectroscopy, Pharmaceutical Special Issue, 2014 (in press). Copyright IM Publications 2014.

Limits of The Correction

There are limitations to the proposed correction. The procedure is based on the assumption that the material causing the fouling is purely coating. Further, crystals at different distances must be detected as discussed above. To enable this, a sufficient signal to noise ratio is needed.

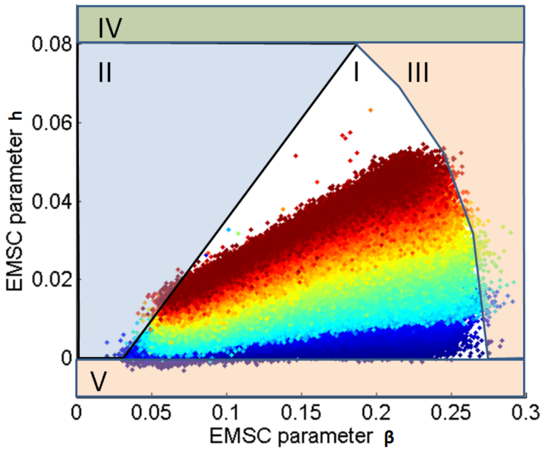

Figure 5.48: The obtained EMSC parameters β and h for a coating process. The regions mark various extreme cases: I) Regular process, II) too large overall absorption, III) unusual substrate absorption, IV) coating dominated spectra, V) negative coating;[24]

In Figure 5.48, a typical process is depicted in the $\beta - h$ parameter space. Moreover, the limitations are indicated, dividing the graph in several regions.

Regular measurements are found in region I, where the discussed correction procedure can be applied. In region II, the signal of the substrate crystals is very weak, and the signal to noise ratio would not be sufficient to perform an EMSC. Such spectra were recorded, but were discarded by the exclusion of measurements with a mean pseudo-absorbance higher than 1. As fouling increases, more and more radiation is absorbed, leading to the broadening of the region with increasing parameter h. The border between the regions I and III is given by the most intense absorption spectra of the substrate material, and spectra inside region III are usually not measured. Again with increasing

---

[24] Reproduced from Scheibelhofer et. al., Journal of Near Infrared Spectroscopy, Pharmaceutical Special Issue, 2014 (in press). Copyright IM Publications 2014.

coating, the absorption of substrate material decreases, leading to the expansion of region III along the y-axis. At the intersection of region I, II, III, and in region IV, just coating and noise is seen, invalidating the mathematical correction. Finally region V describes the physically impossible state of less than zero coating and cannot be observed.

A time delay in interpreting the spectra is essential for the moving mean to be calculated. A delay of about 10 s was required to correct the values. The quality of spectra needed, and the time windows used in the calculations were based on existing process understanding and initial testing experiments and calculations. For other processes, these values may be different and must be determined which may turn out to be a time-consuming procedure.

5.6.4 Process Examples

Various typical runs of the coating process are discussed in this section. In the following figures, $h_{\text{coating}}(t)$ will be given as fraction of the desired coating thickness. Moreover, to reduce fluctuations, the mean of 100 acquisitions steps (approx. 1 second) is shown, as well as the standard deviation for this 1 second.

A typical desired coating run is illustrated in Figure 5.49 (it is the same run as in Figures 5.43 and 5.44). The upper line represents the amount of coating (h_{coating}) detected on the substrate particles, in fractions of the desired amount. After some disturbances at the beginning of the process, the continuous growth of coating can be observed. The increase is linear in both cases, since the amount of the added liquid is linear with time. The lower line represents the amount of coating attributed to window fouling (h_{fouling}). This indicates that the layer of coating on the probe window also gradually grows with time. Without the applied correction method, one would observe the sum of both curves. The process ends after approximately 50 min, when the crystals have received the desired amount of coating.

What is notable in Figure 5.49 is that it shows the simultaneous acquisition of spectra at different positions inside the fluid bed. This allows a much more powerful estimation of the process state, a rough location of fault development, the cross control of different sensors, and much more. As this is a large topic on itself, the reader is referred to [164], where the advantages of the multipoint system for the fluid bed are discussed extensively.

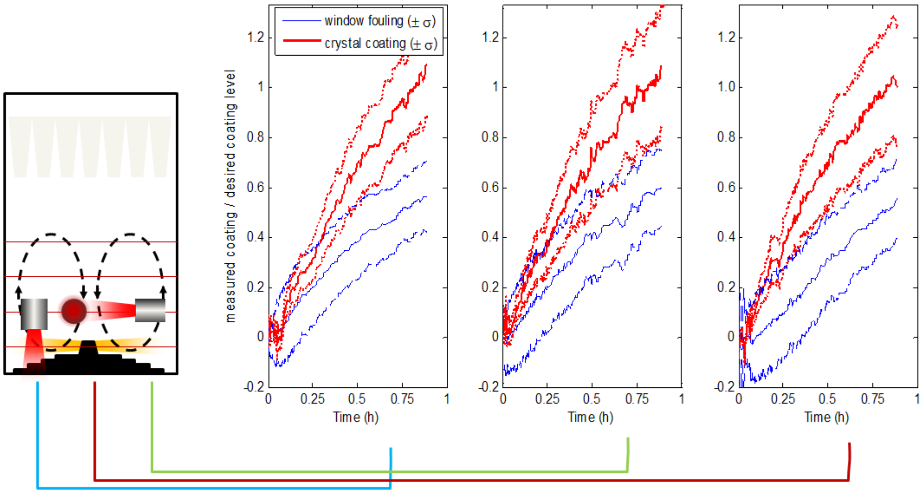

Figure 5.49: Example of a typical coating process, monitored at several positions. The blue lines correspond to the estimated amount of window fouling, and the red line to the amount of coating on the substrate material. The dashed lines give the standard deviation.

Two further examples are discussed. Figure 5.50 shows in the upper part a process with an unclean probe, i.e., there is still a layer of coating on the probe from a previous run. Already at the beginning, the layer of coating on the probe window is detected. Nonetheless, the growth of coating on the crystals can be observed. However, an unusual behavior can be seen in the beginning of the process, for unclear reasons.

For the last example, the supply of the coating material was suspended for 25 min (Figure 5.50, below). During that time the amount of coating remained the same on the probe window but seemed to have slightly decreased on the crystals, probably due to abrasion. The process was run for a longer time than usual and the final amount of coating applied is more than desired.

For all three mentioned processes, the coating mass followed a linear growth trend in the beginning of the coating process which reflects the linear nature of feeding of the coating. However, as the process continued, this trend slowly declined, due to the increasing thickness of the coating and the exponential decay of near-infrared light in the coating layer, leading to a smaller contribution of lower coating layers in the absorption spectra.

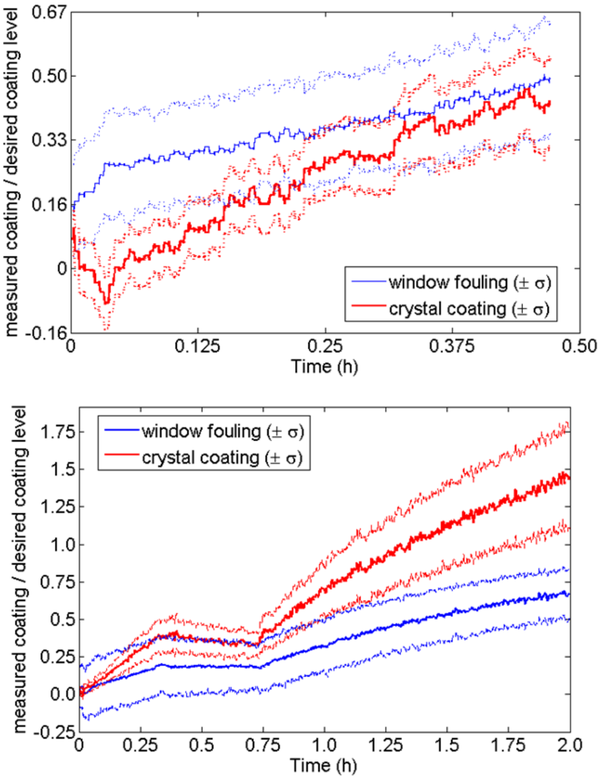

Figure 5.50: Examples of untypical coating processes. The blue lines correspond to the estimated amount of window fouling, and the red line to the amount of coating on the substrate material. The dashed lines give the standard deviation. The upper picture shows a process, where the probe was already coated at the beginning of the process. In the lower picture the addition of coating material was halted for 25 minutes.[25]

---

[25] Reproduced from Scheibelhofer et. al., Journal of Near Infrared Spectroscopy, Pharmaceutical Special Issue, 2014 (in press). Copyright IM Publications 2014.

5.6.5 Results

A hot-melt coating process in a fluidized bed reactor was investigated, and the growth of coating that resulted in window fouling was monitored. The proposed mathematical treatment allowed the elimination of the influence of window fouling on the measurements, without changing the measurement geometry.

Specifically, the presented method allows a distinction between coating on the crystals and coating on the probe window resulting in fouling. We have shown that, rather than averaging scans to eliminate the unwanted spectral variability, this variability can be used to obtain information regarding the process state which is a novel approach to monitor such processes.

The benefits of our method include the elimination of cleaning cycles during the running process which may lead to a black out of measurement. However, the presented approach cannot substitute window cleaning in between different batches or over long operation times.

Although the presented method has limitations, it can be used for a variety of other processes, where window fouling presents a problem. If sufficient spectral data is available, the presented procedure may also be well-suitable for reevaluation of historical data.

6 Summary and Conclusion

Understanding production processes of pharmaceuticals is crucial, in order to guarantee the potency and safety of the medicine. In this work, NIR spectroscopy was used to create process data, and thereof process knowledge. To this advance, systems enabling synchronous measurements at several positions were used. Such systems are novel, and hence were reappraised for their utility and interpretation possibilities, to afterwards add to process understanding.

Providing automatic and contact-free non-invasive monitoring, near-infrared spectroscopy is the non-destructive method of choice. Furthermore, with the current interest in continuous processing, the speed of spectroscopic methods, in particular of near-infrared spectroscopy, offers a significant advantage. In this work NIRS has proven to be a versatile tool for the monitoring of several different processes.

Since pharmaceutical processes often involve air/moisture sensitive and/or high-potency substances, transport between unit operations and processes must be carefully contained. Hence, the proper probe should be chosen carefully. The illumination and detection area, the position and probe to sample distance, the chemical inertia, possibilities to clean the probe and much more have to be considered. Therefore, the right set-up is crucial. As a consequence, the effect of different sampling parameters; and the effect of spectral treatments was considered in this work.

To maximize process information it is desirable to measure at multiple positions either in parallel production lines or at consecutive steps or even at several positions in one unit operation. Different possibilities enabling parallel sampling exist, of which three were used in this work. So the question of comparability between measurements and the transferability of chemometric models is of imminent importance, and appears throughout the thesis several times.

For the monitoring of an open powder stream, leaving a dosing feeder unit, hyperspectral imaging was used. Hyperspectral imaging successfully allowed to detect impurities, determine the concentration of trinary mixtures, and finally to asses the homogeneity of the powder stream at varying scrutiny.

For the monitoring of a blending process, a FT-spectrometer in combination with an optical fiber switch was used. A customized blending vessel enabled to access the blending process at several positions. Thus, following the distribution of chemical entities inside the blending vessel via spectroscopic means, gave access to a picture of the blending dynamics inside the vessel, which would have been impossible with just a single probe. Even more extreme, in the case of blending, it was shown that the naive use of a single probe can lead to a misinterpretation of the blending quality.

Finally, the combination of fiber connective optics and hyperspectral imaging units leads to a synergy of the benefits using the versatility of probes with speed and parallel abilities of imaging systems. In this work, such a multipoint NIR spectrometer based on an adapted hyperspectral imaging system was used.

As such combined systems are still rare nowadays, a number of basic performance tests were performed, to appraise the benefits of this system. Within the pharmaceutical hot-melt-coating process discussed here that was monitored with this device, it was shown that it is not useful to implement further variables into the model to correct for port and position. In contrast, the simple application of a model by joining all sensors shows the best performance, whereas overfitting appears otherwise.

An emerging problem when operating the coating process, was window fouling. As a counteract, a mathematical treatment was developed, to distinguish between coating on the probe window, and coating on the processed particles, which is also presented in this work.

In the end, it should not be concealed that handling the emerging large data volume turned out to be a complex task, even for modern equipment.

All in all, the application of multipoint-measurements turned out to be a suitable and powerful method to deliver information of the investigated processes. It enables to clarify, if unexpected measured or predicted values are caused by errors of the measurement system, or have their origin in the monitored process.

The ability of model transfer between ports, i.e. positions, opens up a field of possibilities, e.g. several NIR probes at the same process allow the development of self-referencing methods. Hence, different sensors can control and correct themselves. For example, a mechanism of reacting to sensor failure can be established. Furthermore, having several points of investigation at a process step clearly enhances the abilities for process control and understanding.

The sample size, and desired depth of scrutiny, when measuring at pharmaceutical processes is not straightforward, and discussions on the correct application are still going on at the very moment. In future tasks, the combination of several sources of information to understand a process will become increasingly important. Measurements of spectrometer and probe combinations, suitable for the task at hand, as well as information gained by univariate sensors, e.g. pH-values, must be combined to enlarge the knowledge, and finally physically apprehend, already existing, but often just poorly and empirically understood processes.

Danksagung (Acknowledgments)

Hier, zwischen der Zusammenfassung der letzten Ergebnisse, und dem trockenen Anhang, ist wohl ein guter Moment, innezuhalten, um den Menschen die das Gelingen dieser Arbeit ermöglicht haben, zu danken.

Zuallererst bedanken möchte ich mich bei meinem Betreuer Herrn Prof. Schennach der mich durch die Jahre der Dissertation geleitet hat. Ebenso gilt der Dank Herrn Prof. Kleinebudde, der die Arbeit des Zweitgutachters auf sich genommen hat.

Die vorliegende Arbeit entstand am Research Center Pharmaceutical Engineering GmbH (RCPE), unter Führung von Daniel Koller, Christina Voura, Simon Fraser, Jose Menezes und Stephan Sacher, die alle zu verschiedenen Zeitpunkten meine Vorgesetzten waren, auch ihnen sei an dieser Stelle gedankt.

Besonderer Dank gilt Herrn Daniel Sandu und Herrn Peter Kerschhaggl von der EVK DI Kerschhaggl GmbH, für ihren unverzichtbaren Beitrag an dieser Dissertation.

Nicht zuletzt bedanken möchte ich mich aber bei meinen Kollegen in der Continuous Process [sic!] and Quality Control Gruppe die mich über die Jahre hinweg unter- und ausgehalten haben, und zu zahlreichen fruchtbringenden Diskussionen beigetragen haben. Vielen Dank an Nikolaus Balak, Patrick Wahl, Roland Hohl, Daniel Markl, Elena Stocker, und Hanna Greiner. Weiters möchte ich mich bei den Kolleginnen und Kollegen Eva Faulhammer, Eva Saurugger, Verena Wahl, Michael Gruber, Paul Rinner, Helmut Pessek, Manuel Zettl und Daniel Wiegele, die mir alle auf die eine oder andere Art geholfen haben, und so diese Dissertation ermöglicht haben, bedanken.

Schlussendlich auch noch Dank an jene, die mich unterstützt haben, deren Namen hier aber nicht explizit aufgeführt sind.

List of Figures

0.1 Powders, in VIS and NIR-PC space 2

1.1 An example for chemical imaging 11

2.1 Comparison of energy, wavelength and wavenumber for the near-infrared range. 16
2.2 Examples for different numbers of scattering centers. 18
2.3 Photon path distribution in a media with absorption. 21
2.4 Photon path distribution from source to detector. 22
2.5 Probe head of the Hellma NIR diffuse reflectance probe. 24
2.6 Raw spectra with different concentrations of citric acid 27
2.7 SNV-transformed spectra 28
2.8 Spectra smoothed with Savitzky-Golay 29
2.9 1st derivative of spectra with Savitzky-Golay 30
2.10 MSC transformed spectra 31
2.11 Mean centered and UV-scaled spectra 33
2.12 Illustration of the basics of principle component analysis. 34
2.13 Loading plot of the SNV-transformed spectra 35
2.14 PCA - Score plot of the SNV-transformed spectra 36
2.15 Inner Relation of PLS 41
2.16 Loading weight plot of the SNV-transformed spectra 42
2.17 Score plot of the SNV-transformed spectra 42
2.18 Regression coefficients for a PLS model 43
2.19 Observed vs. Prediction plot 44
2.20 Examples for different homogeneity levels 47
2.21 Typical length scales 49

3.1 Experimental set-up with the EVK Helios Starter-Kit 54
3.2 Image of the laboratory workbench 55
3.3 Schematic illustration of the blending vessel. 58
3.4 Particle images of the used materials 60
3.5 Size distributions of the materials obtained 61

4.1 Screenshot of the HeliosViewer. 65
4.2 Intensity on chip for dark and white reference measurements. . . . 68
4.3 Measurement of the wavelength standard sample. 69
4.4 First derivative of the measurement of the wavelength standard. . 69
4.5 Linear and quadratic regression between wavelength and pixel position. 70
4.6 Spectra of polystyrene wavelength standard. 72
4.7 Dynamic ranges for low gain and high gain 73
4.8 Signal to noise ratio for low gain and high gain 73
4.9 RMSN noise estimation 74
4.10 Intensity measured on chip for specimen with different reflectivity 75
4.11 Absorbance measured for specimen with different reflectivity . . . 76
4.12 Comparison of expected and observed absorbance at three different wavelengths 76
4.13 Intensity on chip 77
4.14 Comparison of the wavelength mapping 78
4.15 Reproduction of signal pattern at a different port 78
4.16 Elucidation of pixel overflow. 80
4.17 Counts for dark current. 81
4.18 Dark current correction interval. 82
4.19 Fraction of signal caused by dark current. 82
4.20 Long term drift of the baseline. 83
4.21 Intensity on chip when measuring dark current and white background 84
4.22 Dynamic range and signal to noise ratio. 85
4.23 Different binning scenarios. 85
4.24 Same sample monitored with three different probes. 86
4.25 Differences for port 1 compared to the ports 2 and 3. 87
4.26 PCA scores plot on gray standard measurements 90
4.27 Regression coefficients for gray standard measurements 91
4.28 PCA scores plot on coating process data 93
4.29 Regression coefficients for coating process data 94
4.30 Spectra corrected with the reference measurement at the lamp. . . 96

5.1 Comparison of measured and modeled size distribution 99
5.2 Assumed shape of ASA crystals 99
5.3 Sketch of the sampling on the rotating disk 101
5.4 Relation of scanned volume and concentration accuracy 102
5.5 Variance versus concentration for unpretreated spectra 103

5.6 Coefficients for variances of unpretreated spectra 103
5.7 Variance versus concentration for SNV-preatreated spectra 104
5.8 Coefficients for variances for SNV-pretreated spectra 104
5.9 Variance versus concentration for predicted concentration levels . 105
5.10 Coefficients for variances for predicted concentration levels 105
5.11 Empirical and theoretical variances for different concentration levels 106
5.12 Histogram of the ratio of empirical and true variance 107
5.13 Sketch for calculating the penetration depth on the turntable . . . 108
5.14 Penetration depth with the push-broom system. 110
5.15 Penetration depth at different particle sizes 110
5.16 Comparison of an optical image and a hyperspectral NIR-image . 112
5.17 The experimental setup with feeder and HSI-camera 113
5.18 Powder flow across an inclined plate and selection of calibration samples 115
5.19 PCA on the recorded data to detect impurities 116
5.20 PLS analysis of an inhomogeneous powder flow 116
5.21 PLS analysis of a homogeneous powder flow 117
5.22 Estimated concentration with confidence interval 118
5.23 Measured concentrations with different sample sizes 119
5.24 Set-up for lab-scale blending 122
5.25 Concentration of ASA over time, for the case of segregation 127
5.26 Concentration of ASA over time, for the case of blending with LM 128
5.27 Decrease in variance during progression of blending 131
5.28 Score trajectory curve for the blending process 135
5.29 Observed vs. predicted plot of the PLS regression with all positions 136
5.30 Same experiment predicted with the single probe and general models 138
5.31 Seventy grams of LM was deposited on 70g of ASA 141
5.32 Seventy grams of ASA was deposited on 70g of LM 142
5.33 Experiments with different H/D ratios. 145
5.34 Blending times for different fill levels 146
5.35 Example for a long term blending experiment lasting 20 hours . . 148
5.36 Scheme of the experimental design for testing the blender 151
5.37 Illustration of the continuous blender 152
5.38 API concentration and mass over time for a typical blending run. . 153
5.39 Contour plot of the Coefficient of Variation for different blender settings 154
5.40 Spectra of the coating process 159
5.41 Sketch of the effect of probe-particle distance 161
5.42 EMSC parameters α and β 162

5.43 The obtained EMSC parameters over the coating process 163
5.44 EMSC parameters h over β during a coating process 165
5.45 EMSC parameters h over β during a coating process without coating material 166
5.46 The obtained EMSC parameters β and h for offline samples 167
5.47 Comparison between off- and in-line measurements 168
5.48 Extreme cases for the EMSC parameters 169
5.49 Example of a typical coating process 171
5.50 Examples of untypical coating processes 172

List of Tables

2.1 Explained variance with increasing PCs 38

3.1 Attributes of materials 61

4.1 Nominal and reconstructed wavelengths and their difference. . . . 71
4.2 Linear regression for mapping wavelength to pixel number 79
4.3 Statistics on the created PLS-models with gray standards 92
4.4 Statistics on the created PLS-models on maturity 95

5.1 Parameters of the predictive PLS model 124
5.2 Summary of the model statistics for the single-probe calibration and general model 139
5.3 Blending times for different loading orders 144

Bibliography

[1] U. S. Food and Drug Administration. *Guidance for Industry. PAT - A Framework for Innovative Pharmaceutical Development, Manufacturing, and Quality Assurance*. 2004. URL: `http://www.fda.gov/downloads/Drugs/GuidanceComplianceRegulatoryInformation/Guidances/UCM070305.pdf` (visited on 01/13/2014).

[2] International Conference on Harmonisation of Technical Requirements for Registration of Pharmaceuticals for Human Use. *ICH Q8: pharmaceutical development (R2)*. 2009. URL: `http://www.ich.org/fileadmin/Public%5C_Web%5C_Site/ICH%5C_Products/%20Guidelines/Quality/Q8%5C_R1/Step4/Q8%5C_R2%5C_Guideline.pdf` (visited on 01/13/2014).

[3] International Conference on Harmonisation of Technical Requirements for Registration of Pharmaceuticals for Human Use. *ICH Q9: quality risk management*. 2005. URL: `http://www.ich.org/fileadmin/Public%5C_Web%5C_Site/ICH%5C_Products/Guidelines/%20Quality/Q9/Step4/Q9%5C_Guideline.pdf` (visited on 01/13/2014).

[4] International Conference on Harmonisation of Technical Requirements for Registration of Pharmaceuticals for Human Use. *ICH Q10: pharmaceutical quality risk management*. 2008. URL: `http://www.ich.org/fileadmin/Public%5C_Web%5C_Site/ICH%5C_Products/%20Guidelines/Quality/Q10/Step4/Q10%5C_Guideline.pdf` (visited on 01/13/2014).

[5] Gabriele Reich. “Near-infrared spectroscopy and imaging: basic principles and pharmaceutical applications.” In: *Advanced drug delivery reviews* 57.8 (June 2005), pp. 1109–43. ISSN: 0169-409X. DOI: `10.1016/j.addr.2005.01.020`.

[6] Gary W. Small. “Chemometrics and near-infrared spectroscopy: Avoiding the pitfalls.” In: *TrAC Trends in Analytical Chemistry* 25.11 (Dec. 2006), pp. 1057–1066. ISSN: 01659936. DOI: `10.1016/j.trac.2006.09.004`.

[7] Jan P. Luypaert, Désiré L. Massart, and Yvan V. Vander Heyden. "Near-infrared spectroscopy applications in pharmaceutical analysis." In: *Talanta* 72.3 (May 2007), pp. 865–83. ISSN: 1873-3573. DOI: `10.1016/j.talanta.2006.12.023`.

[8] Yves Roggo et al. "A review of near infrared spectroscopy and chemometrics in pharmaceutical technologies." In: *Journal of Pharmaceutical and Biomedical Analysis* 44.3 (July 2007), pp. 683–700. ISSN: 0731-7085. DOI: `10.1016/j.jpba.2007.03.023`.

[9] Donald A. Burns and Emil W. Ciurczak. *Handbook of Near-Infrared Analysis*. 3rd ed. CRC Press, 2008. ISBN: 978-0-8493-7393-0.

[10] Åsmund Rinnan, Frans Van Den Berg, and Søren Balling Engelsen. "Review of the most common pre-processing techniques for near-infrared spectra." In: *TrAC Trends in Analytical Chemistry* 28.10 (Nov. 2009), pp. 1201–1222. ISSN: 01659936. DOI: `10.1016/j.trac.2009.07.007`.

[11] Don E. Pivonka, John M. Chalmers, and Peter R. Griffiths, eds. *Applications of Vibrational Spectroscopy in Pharmaceutical Research and Development*. John Wiley & Sons Ltd., 2007.

[12] Thomas De Beer et al. "Near infrared and Raman spectroscopy for the in-process monitoring of pharmaceutical production processes." In: *International Journal of Pharmaceutics* 417 (Dec. 2011), pp. 32–47. ISSN: 1873-3476. DOI: `10.1016/j.ijpharm.2010.12.012`.

[13] Tarja Rajalahti and Olav M. Kvalheim. "Multivariate data analysis in pharmaceutics: A tutorial review." In: *International Journal of Pharmaceutics* 417.1-2 (Feb. 2011), pp. 280–290. ISSN: 1873-3476. DOI: `10.1016/j.ijpharm.2011.02.019`.

[14] Marzena Jamrógiewicz. "Application of the near-infrared spectroscopy in the pharmaceutical technology." In: *Journal of Pharmaceutical and Biomedical Analysis* 66 (July 2012), pp. 1–10. ISSN: 1873-264X. DOI: `10.1016/j.jpba.2012.03.009`.

[15] Rudolf W. Kessler. "Perspectives in process analysis." In: *Journal of Chemometrics* 27.11 (Sept. 2013), pp. 369–378. ISSN: 08869383. DOI: `10.1002/cem.2549`.

[16] Alexey L. Pomerantsev and Oxana Ye. Rodionova. "Process analytical technology: a critical view of the chemometricians." In: *Journal of Chemometrics* 26.6 (June 2012), pp. 299–310. ISSN: 08869383. DOI: `10.1002/cem.2445`.

[17] David L. Wetzel. "Near-Infrared Reflectance Analysis." In: *Analytical Chemistry* 55.12 (1983), pp. 1165–1176.

[18] Fred W. McClure. "The Giant is Running Strong." In: *Analytical Chemistry* 66.1 (1994), 43A–53A.

[19] Jukka Rantanen et al. "On-line monitoring of moisture content in an instrumented fluidized bed granulator with a multi-channel NIR moisture sensor." In: *Powder Technology* 99 (1998), pp. 163–170.

[20] Nicolas Heigl et al. "Quantitative on-line vs. off-line NIR analysis of fluidized bed drying with consideration of the spectral background." In: *European Journal of Pharmaceutics and Biopharmaceutics* September (Sept. 2013). ISSN: 1873-3441. DOI: `10.1016/j.ejpb.2013.09.012`.

[21] Arwa S. El-Hagrasy et al. "Near-Infrared Spectroscopy and Imaging for the Monitoring of Powder Blend Homogeneity." In: *Journal of Pharmaceutical Sciences* 90.9 (Sept. 2001), pp. 1298–307. ISSN: 0022-3549.

[22] Sonja S. Sekulic et al. "On-Line Monitoring of Powder Blend Homogeneity by Near-Infrared Spectroscopy." In: *Analytical Chemistry* 68.3 (Feb. 1996), pp. 509–13. ISSN: 0003-2700. DOI: `10.1021/ac950964m`.

[23] Daniel M. Koller et al. "Continuous quantitative monitoring of powder mixing dynamics by near-infrared spectroscopy." In: *Powder Technology* 205.1-3 (Jan. 2011), pp. 87–96. ISSN: 00325910. DOI: `10.1016/j.powtec.2010.08.070`.

[24] Lars Petersen, Pentti Minkkinen, and Kim H. Esbensen. "Representative sampling for reliable data analysis: Theory of Sampling." In: *Chemometrics and Intelligent Laboratory Systems* 77.1-2 (Dec. 2004), pp. 261–277. ISSN: 01697439. DOI: `10.1016/j.chemolab.2004.09.013`.

[25] Kim H. Esbensen and Peter Paasch-Mortensen. "Process Sampling (Theory of Sampling, TOS)-the Missing Link in Process Analytical Technology." In: *Process Analytical Technology*. Ed. by K. A. Baakev. 2nd ed. Wiley, 2010, pp. 37–80.

[26] José Torrent and Vidal Barrón. "Diffuse Reflectance Spectroscopy." In: *Methods of Soil Analysis: Part 5 - Mineralogical methods*. Ed. by A. L. Ulery and L. R. Drees. 5. Madiosn: Soil Science Society of America Inc., 2008. Chap. 13, pp. 367–385. ISBN: 978-0-89118-846-9.

[27] Ola Berntsson et al. "Effective Sample Size in Diffuse Reflectance Near-IR Spectrometry." In: *Analytical Chemistry* 71.3 (Feb. 1999), pp. 617–23. ISSN: 0003-2700. DOI: `10.1021/ac980652u`.

[28] Yang Liu and Daniel Blackwood. “Sample Presentation in Rotary Tablet Press Feed Frame Monitoring by Near Infrared Spectroscopy.” In: *American Pharmaceutical Review* May (2012).

[29] Kristiina Järvinen et al. “In-line monitoring of the drug content of powder mixtures and tablets by near-infrared spectroscopy during the continuous direct compression tableting process.” In: *European Journal of Pharmaceutical Sciences* 48.4-5 (Mar. 2013), pp. 680–8. ISSN: 1879-0720. DOI: `10.1016/j.ejps.2012.12.032`.

[30] Thorsten Herkert, Heino Prinz, and Karl-Artur Kovar. “One hundred percent online identity check of pharmaceutical products by near-infrared spectroscopy on the packaging line.” In: *European Journal of Pharmaceutics and Biopharmaceutics* 51.1 (Jan. 2001), pp. 9–16. ISSN: 0939-6411.

[31] Muhanned Saeed et al. “Assessment of Diffuse Transmission Mode in Near-Infrared Quantification — Part I : The Press Effect on Low-Dose Pharmaceutical Tablets.” In: *Journal of Pharmaceutical Sciences* 98.12 (2009), pp. 4877–4886. DOI: `10.1002/jps`.

[32] Fiona Clarke. “Extracting process-related information from pharmaceutical dosage forms using near infrared microscopy.” In: *Vibrational Spectroscopy* 34.1 (Jan. 2004), pp. 25–35. ISSN: 09242031. DOI: `10.1016/j.vibspec.2003.08.005`.

[33] Neil E. Lewis, Joe Schoppelrei, and Eunah Lee. “Near-infrared Chemical Imaging and the PAT Initiative.” In: *Spectroscopy* 19.April (2004), pp. 26–36.

[34] Simin H. Tabasi et al. “Quality by Design , Part II : Application of NIR Spectroscopy to Monitor the Coating Process for a Pharmaceutical Sustained Release Product.” In: *Journal of Pharmaceutical Sciences* 97.9 (2008), pp. 4052–4066. DOI: `10.1002/jps`.

[35] Anna Palou et al. “Determination of drug, excipients and coating distribution in pharmaceutical tablets using NIR-CI.” In: *Journal of Pharmaceutical Analysis* (Nov. 2011). ISSN: 20951779. DOI: `10.1016/j.jpha.2011.11.003`.

[36] Ravendra Singh, Marianthi Ierapetritou, and Rohit Ramachandran. “System-wide hybrid MPC-PID control of a continuous pharmaceutical tablet manufacturing process via direct compaction.” In: *European Journal of Pharmaceutics and Biopharmaceutics* 85.3 Part B (Mar. 2013), pp. 1164–1182. ISSN: 1873-3441. DOI: `10.1016/j.ejpb.2013.02.019`.

[37] Matheus P. Freitas et al. "Prediction of drug dissolution profiles from tablets using NIR diffuse reflectance spectroscopy: A rapid and nondestructive method." In: *Journal of Pharmaceutical and Biomedical Analysis* 39.1-2 (Oct. 2005), pp. 17–21. ISSN: 0731-7085. DOI: `10.1016/j.jpba.2005.03.023`.

[38] Patrick R. Wahl et al. "Inline monitoring and a PAT strategy for pharmaceutical hot melt extrusion." In: *International Journal of Pharmaceutics* 455.1-2 (Oct. 2013), pp. 159–68. ISSN: 1873-3476. DOI: `10.1016/j.ijpharm.2013.07.044`.

[39] Lizbeth Martínez, Antonio Peinado, and Lorenz Liesum. "In-line quantification of two active ingredients in a batch blending process by near-infrared spectroscopy: Influence of physical presentation of the sample." In: *International Journal of Pharmaceutics* 451.1-2 (July 2013), pp. 67–75. ISSN: 1873-3476. DOI: `10.1016/j.ijpharm.2013.04.078`.

[40] Barabara Boldrini et al. "Hyperspectral imaging: a reveiw of best practice, performace and pitfalls for in-line and on-line applications." In: *Journal of Near Infrared Spectroscopy* 20 (2012), pp. 483–508.

[41] Waltraud Kessler, Dieter Oelkrug, and Rudolf Kessler. "Using scattering and absorption spectra as MCR-hard model constraints for diffuse reflectance measurements of tablets." In: *Analytica Chimica Acta* 642.1-2 (May 2009), pp. 127–34. ISSN: 1873-4324. DOI: `10.1016/j.aca.2009.01.057`.

[42] Christoffer Abrahamsson et al. "Time-resolved NIR spectroscopy for quantitative analysis of intact pharmaceutical tablets." In: *Analytical Chemistry* 77.4 (Feb. 2005), pp. 1055–9. ISSN: 0003-2700.

[43] Aoife A. Gowen et al. "Recent applications of Chemical Imaging to pharmaceutical process monitoring and quality control." In: *European Journal of Pharmaceutics and Biopharmaceutics* 69.1 (May 2008), pp. 10–22. ISSN: 0939-6411. DOI: `10.1016/j.ejpb.2007.10.013`.

[44] Aoife A. Gowen et al. "Time series hyperspectral chemical imaging data: Challenges, solutions and applications." In: *Analytica Chimica Acta* 705.1-2 (Oct. 2011), pp. 272–82. ISSN: 1873-4324. DOI: `10.1016/j.aca.2011.06.031`.

[45] Da-Wen Sun, ed. *Hyperspectral Imaging for Food Quality Analysis and Control*. London: Elsevier Inc., 2010. ISBN: 978-0-12-374753-2.

[46] Paul Geladi et al. “Principal component analysis of multivariate images.” In: *Chemometrics and Intelligent Laboratory Systems* 5.3 (Mar. 1989), pp. 209–220. ISSN: 01697439. DOI: 10.1016/0169-7439(89)80049-8.

[47] Aoife A. Gowen et al. “Hyperspectral imaging – an emerging process analytical tool for food quality and safety control.” In: *Trends in Food Science & Technology* 18.12 (Dec. 2007), pp. 590–598. ISSN: 09242244. DOI: 10.1016/j.tifs.2007.06.001.

[48] Marcus Groinig, Markus Burgstaller, and Manfred Pail. “Industrial Application of a New Camera System based on Hyperspectral Imaging for Inline Quality Control of Potatoes.” In: *ÖAGM/AAPR Workshop*. Graz, 2011.

[49] Markus Burgstaller. “Anwendungen von Chemical Imaging Kameras zur Inline-Sortierung von Kunststoffen in der Recycling Industrie.” In: *Arbeitskreid Prozessanalytik in der GDCh-Fachgruppe Analytische Chemie und in der DECHEMA, 6. Kolloquium*. 2010.

[50] Juan G. Rosas and Marcelo Blanco. “A criterion for assessing homogeneity distribution in hyperspectral images. Part 2: Application of homogeneity indices to solid pharmaceutical dosage forms.” In: *Journal of Pharmaceutical and Biomedical Analysis* 70 (Nov. 2012), pp. 691–9. ISSN: 1873-264X. DOI: 10.1016/j.jpba.2012.06.037.

[51] Otto Scheibelhofer et al. “Continuous powder flow monitoring via near-infrared hyperspectral imaging.” In: *IEEE International nstrumentation and Measurement Technology Conference (I2MTC) Proceedings*. Graz, 2012, pp. 748–753. DOI: 10.1109/I2MTC.2012.6229431.

[52] Lene Maurer and Hans Leuenberger. “Terahertz pulsed imaging and near infrared imaging to monitor the coating process of pharmaceutical tablets.” In: *International Journal of Pharmaceutics* 370.1-2 (Mar. 2009), pp. 8–16. ISSN: 1873-3476. DOI: 10.1016/j.ijpharm.2008.11.011.

[53] Juan G. Rosas and Marcelo Blanco. “A criterion for assessing homogeneity distribution in hyperspectral images. Part 1: Homogeneity index bases and blending processes.” In: *Journal of Pharmaceutical and Biomedical Analysis* 70 (Nov. 2012), pp. 680–90. ISSN: 1873-264X. DOI: 10.1016/j.jpba.2012.06.036.

[54] José Manuel Amigo. “Practical issues of hyperspectral imaging analysis of solid dosage forms.” In: *Analytical and Bioanalytical Chemistry* 398.1 (Sept. 2010), pp. 93–109. ISSN: 1618-2650. DOI: 10.1007/s00216-010-3828-z.

[55] Otto Scheibelhofer et al. "Spatially Resolved Monitoring of Powder Mixing Processes via Multiple NIR-Probes." In: *Powder Technology* 243 (2013), pp. 161–170.

[56] Benoît Igne et al. "Online Monitoring of Pharmaceutical Materials Using Multiple NIR Sensors—Part I: Blend Homogeneity." In: *Journal of Pharmaceutical Innovation* 6.1 (Apr. 2011), pp. 47–59. ISSN: 1872-5120. DOI: `10.1007/s12247-011-9099-1`.

[57] Payal Roychoudhury et al. "Multiplexing fibre optic near infrared (NIR) spectroscopy as an emerging technology to monitor industrial bioprocesses." In: *Analytica Chimica Acta* 590.1 (May 2007), pp. 110–7. ISSN: 1873-4324. DOI: `10.1016/j.aca.2007.03.011`.

[58] Anne Heikkilä. *Multipoint-NIR-measurements in pharmaceutical powder applications*. 704. Espoo: VTT Technical Research Center of Finland, 2009, pp. 1–59. ISBN: 9789513873349.

[59] Otto Scheibelhofer et al. "Monitoring Blending of Pharmaceutical Powders with Multipoint NIR Spectroscopy." In: *AAPS PharmSciTech* 14.1 (Mar. 2013), pp. 234–44. ISSN: 1530-9932. DOI: `10.1208/s12249-012-9910-4`.

[60] Julia Märk et al. "Online Process Control of a Pharmaceutical Intermediate in a Fluidized-Bed Drier Environment Using NearIinfrared Spectroscopy." In: *Analytical Chemistry* 82.10 (May 2010), pp. 4209–15. ISSN: 1520-6882. DOI: `10.1021/ac1004579`.

[61] Turghun Muhammad et al. "Monitoring Dissolution Rate of Amiodarone Tablets by a Multiple Fiber-Optic Sensor System." In: *Dissolution Technologies* February (2008), pp. 22–27.

[62] Andreas S. L. Mendez, Gláucia de Carli, and Cássia V. Garcia. "Evaluation of powder mixing operation during batch production: Application to operational qualification procedure in the pharmaceutical industry." In: *Powder Technology* 198.2 (Mar. 2010), pp. 310–313. ISSN: 00325910. DOI: `10.1016/j.powtec.2009.11.027`.

[63] Norman Harnby. "An engineering view of pharmaceutical powder mixing." In: *Pharmaceutical science & technology today* 3.9 (Sept. 2000), pp. 303–309. ISSN: 1461-5347.

[64] Aditya U. Vanarase and Fernando J. Muzzio. "Effect of operating conditions and design parameters in a continuous powder mixer." In: *Powder Technology* 208.1 (Mar. 2011), pp. 26–36. ISSN: 00325910. DOI: `10.1016/j.powtec.2010.11.038`.

[65] Ralf Weinekötter and Lothar Reh. "Continuous Mixing of Fine Particles." In: *Particle & Particle Systems Characterization* 12.December 1994 (1995), pp. 46–53.

[66] Ralf Weinekötter. "Compact and efficient continuous mixing processes for production of food and pharmaceutical powders." In: *Trends in Food Science & Technology* 20 (2009), pp. 48–50.

[67] John Bridgwater. "Mixing of powders and granular materials by mechanical means—A perspective." In: *Particuology* 10.4 (Aug. 2012), pp. 397–427. ISSN: 16742001. DOI: `10.1016/j.partic.2012.06.002`.

[68] Brenda Remy, Benjamin J. Glasser, and Johannes G. Khinast. "The Effect of Mixer Properties and Fill Level on Granular Flow in a Bladed Mixer." In: *AIChE Journal* 56.2 (2010), pp. 336–353. DOI: `10.1002/aic`.

[69] Stefan Radl et al. "Mixing characteristics of wet granular matter in a bladed mixer." In: *Powder Technology* 200.3 (June 2010), pp. 171–189. ISSN: 00325910. DOI: `10.1016/j.powtec.2010.02.022`.

[70] Dean Brone, Albert Alexander, and Fernando J. Muzzio. "Quantitative Characterization of Mixing of Dry Powders in V-Blenders." In: *AIChE Journal* 44.2 (1998), pp. 271–278.

[71] Atul D. Karande, Celine V. Liew, and Paul W. S. Heng. "Calibration sampling paradox in near infrared spectroscopy: a case study of multi-component powder blend." In: *International Journal of Pharmaceutics* 395.1-2 (Aug. 2010), pp. 91–7. ISSN: 1873-3476. DOI: `10.1016/j.ijpharm.2010.05.011`.

[72] Fernando J. Muzzio, Priscilla Robinson, and Carolyn Wightman. "Sampling practices in powder blending." In: *International Journal of Pharmaceutics* 155.2 (Sept. 1997), pp. 153–178. ISSN: 03785173. DOI: `10.1016/S0378-5173(97)04865-5`.

[73] Martine Poux et al. "Powder mixing: Some practical rules applied to agitated systems." In: *Powder Technology* 68.3 (Dec. 1991), pp. 213–234. ISSN: 00325910. DOI: `10.1016/0032-5910(91)80047-M`.

[74] Fernando J. Muzzio, Troy Shinbrot, and Benjamin J. Glasser. "Powder technology in the pharmaceutical industry: the need to catch up fast." In: *Powder Technology* 124.1-2 (Apr. 2002), pp. 1–7. ISSN: 00325910. DOI: `10.1016/S0032-5910(01)00482-X`.

[75] Thomas Puchert et al. “A new PAT/QbD approach for the determination of blend homogeneity: combination of on-line NIRS analysis with PC Scores Distance Analysis (PC-SDA).” In: *European journal of Pharmaceutics and Biopharmaceutics* 78.1 (May 2011), pp. 173–82. ISSN: 1873-3441. DOI: `10.1016/j.ejpb.2010.12.015`.

[76] Aditya U. Vanarase et al. “Real-time monitoring of drug concentration in a continuous powder mixing process using NIR spectroscopy.” In: *Chemical Engineering Science* 65.21 (Nov. 2010), pp. 5728–5733. ISSN: 00092509. DOI: `10.1016/j.ces.2010.01.036`.

[77] Morten J. Maltesen, Marco van de Weert, and Holger Grohganz. “Design of experiments-based monitoring of critical quality attributes for the spray-drying process of insulin by NIR spectroscopy.” In: *AAPS PharmSciTech* 13.3 (Sept. 2012), pp. 747–55. ISSN: 1530-9932. DOI: `10.1208/s12249-012-9796-1`.

[78] Nhat-Hang Duong et al. “A Homogeneity Study Using NIR Spectroscopy: Tracking Magnesium Stearate in Bohle Bin-Blender.” In: *Drug Development and Industrial Pharmacy* 29.6 (2003), pp. 679–687.

[79] Marcelo Blanco, Ramón González Bañó, and Enriqueta Bertran. “Monitoring powder blending in pharmaceutical processes by use of near infrared spectroscopy.” In: *Talanta* 56.1 (Jan. 2002), pp. 203–12. ISSN: 1873-3573.

[80] Ola Berntsson et al. “Quantitative in-line monitoring of powder blending by near infrared reflection spectroscopy.” In: *Powder Technology* 123.2-3 (Mar. 2002), pp. 185–193. ISSN: 00325910. DOI: `10.1016/S0032-5910(01)00456-9`.

[81] Arwa S. El-Hagrasy and James K. Drennen III. “A Process Analytical Technology approach to near-infrared process control of pharmaceutical powder blending. Part III: Quantitative near-infrared calibration for prediction of blend homogeneity and characterization of powder mixing kinetics.” In: *Journal of Pharmaceutical Sciences* 95.2 (Feb. 2006), pp. 422–34. ISSN: 0022-3549. DOI: `10.1002/jps.20465`.

[82] Ola Berntsson et al. “Quantitative determination of content in binary powder mixtures using diffuse reflectance near infrared spectrometry and multivariate analysis.” In: *Analytica Chimica Acta* 419 (2000), pp. 45–54.

[83] Zhenqi Shi et al. "Process characterization of powder blending by near-infrared spectroscopy: blend end-points and beyond." In: *Journal of Pharmaceutical and Biomedical Analysis* 47.4-5 (Aug. 2008), pp. 738–45. ISSN: 0731-7085. DOI: 10.1016/j.jpba.2008.03.013.

[84] Hua Ma and Carl A. Anderson. "Characterization of Pharmaceutical Powder Blends by NIR Chemical Imaging." In: *Journal of Pharmaceutical Sciences* 97.8 (2008), pp. 3305–3320. DOI: 10.1002/jps.21230.

[85] Hendrik C. van de Hulst. *Light Scattering by Small Particles*. Dover Publications Inc., 1981.

[86] Nicolas Heigl. "Novel Applications of Near-Infrared Diffuse Reflection Spectroscopy in Material Science - Physicochemical Characterisation of Polymers and Nano-Structured Materials." PhD thesis. Leopold-Franzens University Innsbruck, 2009.

[87] Michael B. Simpson. "Near-infrared Spectroscopy for Process Analytical Technology: Theory, Technology and Implementation." In: *Process Analytical Technology*. Ed. by Katherine A. Baakev. 2nd ed. 2010. Chap. 5, pp. 107–155. ISBN: 978-0-470-72207-7.

[88] Craig F. Bohren and Donald R. Huffman. *Absorpton and Scattering of Light by Small Particles*. Wiley-VCH Verlag GmbH & Co. KG, 2004.

[89] Farnaz Boroumand, Jacques E. Moser, and Hubert van den Bergh. "Quantitative Diffuse Reflectance and Transmittance Infrared Spectroscopy of Nondiluted Powders." In: *Applied Spectroscopy* 46.12 (Dec. 1992), pp. 1874–1886. ISSN: 00037028. DOI: 10.1366/0003702924123502.

[90] Tobias Haist. *Optische Phänomene in Natur und Alltag*. 2011. URL: http://elib.uni-stuttgart.de/opus/volltexte/2007/3003/ (visited on 07/08/2013).

[91] Eugene Hecht. *Optik*. Oldenburg Wissenschaftsverlag GmbH, 2009.

[92] Heinz W. Siesler et al., eds. *Near-Infrared Spectroscopy Principles, Instruments, Applications*. Michigan: Wiley-VCH Verlag GmbH, 2002. ISBN: 3-527-30149-6.

[93] Daniel Sandu and Enrico Pigorsch. "Use of a Novel NIR Hyperspectral Imaging Sensor System for Sorting of Recovered Paper." In: *Zukunft Forum Papier, Österreichische Papierfachtagung*. 2010.

[94] Lukas K. H. Bittner et al. "Near-infrared reflection spectroscopy (NIRS) as a successful tool for simultaneous identification and particle size determination of amoxicillin trihydrate." In: *Journal of Pharmaceutical and Biomedical analysis* 54.5 (Apr. 2011), pp. 1059–64. ISSN: 1873-264X. DOI: 10.1016/j.jpba.2010.12.019.

[95] Waltraud Kessler. *Multivariate Datenanalyse für die Pharma-, Bio- und Prozesanalytik*. Weinheim: Wiley-VCH Verlag GmbH & Co. KGaA, 2007. ISBN: 978-3-527-3126-7.

[96] Abraham Savitzky and Marcel E. J. Golay. "Smoothing and Differentiation of Data by Simplified Least Squares Regression." In: *Analytical Chemistry* 36 (1964), pp. 1627–1639.

[97] Lennart Eriksson et al. *Multi- and Megavariate Data Analysis: Basic Principles and Applications*. 3rd ed. Malmö: MKS Umetrics AB, 2013, p. 503. ISBN: 91-973750-5-2.

[98] Harald Martens, Jesper Pram Nielsen, and Søren B. Engelsen. "Light Scattering and Light Absorbance Separated by Extended Multiplicative Signal correction. Application to Near-Infrared Transmission Analysis of Powder Mixtures." In: *Analytical Chemistry* 75.3 (Feb. 2003), pp. 394–404. ISSN: 0003-2700.

[99] Paul Geladi and Bruce R. Kowalski. "Partial least-squares regression: A tutorial." In: *Analytica Chimica Acta* 186 (1986), pp. 1–17.

[100] Lothar Sachs and Jürgen Hedderich. *Angewandte Statistik*. 12th ed. Berlin: Springer Berlin Heidelberg New York, 2006. ISBN: 3-540-32160-8.

[101] Lennart Eriksson et al. *Design of Experiments: Principles and Application*. 3rd ed. Umeå: MKS Umetrics AB, 2008. ISBN: 91-973730-4-4.

[102] Svante Wold, Michael Sjöström, and Lennart Eriksson. "PLS-regression : a basic tool of chemometrics." In: *Chemometrics and Intelligent Laboratory Systems* 58 (2001), pp. 109–130.

[103] Rasmus Bro, Åsmund Rinnan, and Nicolaas (Klaas) M. Faber. "Standard error of prediction for multilinear PLS." In: *Chemometrics and Intelligent Laboratory Systems* 75.1 (Jan. 2005), pp. 69–76. ISSN: 01697439. DOI: 10.1016/j.chemolab.2004.04.014.

[104] Nicolaas (Klaas) M. Faber, Xin-Hua Song, and Philip K. Hopke. "Sample-specific standard error of prediction for partial least squares regression." In: *TrAC Trends in Analytical Chemistry* 22.5 (May 2003), pp. 330–334. ISSN: 01659936. DOI: 10.1016/S0165-9936(03)00503-X.

[105] Lin Zhang and Salvador Garcia-Munoz. “A comparison of different methods to estimate prediction uncertainty using Partial Least Squares (PLS): A practitioner’s perspective.” In: *Chemometrics and Intelligent Laboratory Systems* 97.2 (July 2009), pp. 152–158. ISSN: 01697439. DOI: `10.1016/j.chemolab.2009.03.007`.

[106] Jon Gabrielsson et al. “OPLS methodology for analysis of pre-processing effects on spectroscopic data.” In: *Chemometrics and Intelligent Laboratory Systems* 84.1-2 (Dec. 2006), pp. 153–158. ISSN: 01697439. DOI: `10.1016/j.chemolab.2006.03.013`.

[107] Waltraud Kessler and Rudolf W. Kessler. “Multivariate Curve Resolution - Integration von Wissen in Chemometrische Modelle.” In: *Chemie Ingenieur Technik* 82.4 (Apr. 2010), pp. 441–451. ISSN: 0009286X. DOI: `10.1002/cite.200900176`.

[108] Ralf Marbach. “Multivariate Kalibrierung, Selektivität und die SBC-Methode.” In: *Chemie Ingenieur Technik* 82.4 (Mar. 2010), pp. 453–466. ISSN: 0009286X. DOI: `10.1002/cite.200900174`.

[109] Claudia V. Möltgen, Thorsten Herdling, and Gabriele Reich. “A novel multivariate approach using science-based calibration for direct coating thickness determination in real-time NIR process monitoring.” In: *European Journal of Pharmaceutics and Biopharmaceutics* 85 (Nov. 2013), pp. 1056–63. ISSN: 1873-3441. DOI: `10.1016/j.ejpb.2013.09.011`.

[110] Ernesto Kriesten et al. “Fully automated indirect hard modeling of mixture spectra.” In: *Chemometrics and Intelligent Laboratory Systems* 91.2 (Apr. 2008), pp. 181–193. ISSN: 01697439. DOI: `10.1016/j.chemolab.2007.11.004`.

[111] Ernesto Kriesten et al. “Identification of unknown pure component spectra by indirect hard modeling.” In: *Chemometrics and Intelligent Laboratory Systems* 93.2 (Oct. 2008), pp. 108–119. ISSN: 01697439. DOI: `10.1016/j.chemolab.2008.05.002`.

[112] Richard Hogg. “Mixing and Segregation in Powders : Evaluation , Mechanisms and Processes.” In: *Powder Technology* 27.27 (2009), pp. 3–17.

[113] Matthias Stieß. *Mechanische Verfahrenstechnik - Partikeltechnologie 1*. 3rd ed. Springer, 2009.

[114] Matthew J. Metzger, Brenda Remy, and Benjamin J. Glasser. “All the Brazil nuts are not on top: Vibration induced granular size segregation of binary, ternary and multi-sized mixtures.” In: *Powder Technology* 205.1-3 (Jan. 2011), pp. 42–51. ISSN: 00325910. DOI: `10.1016/j.powtec.2010.08.062`.

[115] Hongming Li and J. McCarthy. “Controlling Cohesive Particle Mixing and Segregation.” In: *Physical Review Letters* 90.18 (May 2003), pp. 2–5. ISSN: 0031-9007. DOI: `10.1103/PhysRevLett.90.184301`.

[116] John J. Fitzpatrick. “Particulate and powder mixing.” In: *Food Mixing*. Ed. by Patrick J. Cullen. Oxford, UK: Blackwell Publishing Ltd., 2009. Chap. 13, pp. 269–287. DOI: `10.1002/9781444312928.ch13`.

[117] Ola Berntsson, Lars-Göran Danielsson, and Staffan Folestad. “Estimation of effective sample size when analysing powders with diffuse reflectance near-infrared spectrometry.” In: *Analytica Chimica Acta* 364 (1998), pp. 243–251.

[118] JungHwan Cho et al. “Effective mass sampled by NIR fiber-optic reflectance probes in blending processes.” In: *Analytica Chimica Acta* 348 (1997), pp. 303–310. DOI: `10.1016/S0003-2670(97)00094-9`.

[119] Weiyong Li et al. “The effect of beam size on real-time determination of powder blend homogeneity by an online near infrared sensor.” In: *Journal of Pharmaceutical and Biomedical Analysis* 43.2 (Jan. 2007), pp. 711–7. ISSN: 0731-7085. DOI: `10.1016/j.jpba.2006.07.015`.

[120] Bowen Wang et al. “Study of probe-sample distance for biomedical spectra measurement.” In: *Biomedical Engineering Online* 10.1 (Jan. 2011), p. 95. ISSN: 1475-925X. DOI: `10.1186/1475-925X-10-95`.

[121] Zhenqi Shi and Carl A. Anderson. “Application of Monte Carlo Simulation-Based Photon Migration for Enhanced Understanding of Near-Infrared (NIR) Diffuse Reflectance . Part I : Depth of Penetration in Pharmaceutical Materials.” In: *Journal of Pharmaceutical Sciences* 99.5 (2010), pp. 2399–2412. DOI: `10.1002/jps`.

[122] Fernando J. Muzzio et al. “Sampling and characterization of pharmaceutical powders and granular blends.” In: *International Journal of Pharmaceutics* 250.1 (Jan. 2003), pp. 51–64. ISSN: 0378-5173.

[123] Isabelle Storme-Paris et al. “Near InfraRed Spectroscopy homogeneity evaluation of complex powder blends in a small-scale pharmaceutical preformulation process, a real-life application.” In: *European Journal of Pharmaceutics and Biopharmaceutics* 72.1 (May 2009), pp. 189–98. ISSN: 1873-3441. DOI: `10.1016/j.ejpb.2008.11.002`.

[124] Ernest Teunou and Denis Poncelet. “Batch and continuous fluid bed coating – review and state of the art.” In: *Journal of Food Engineering* 53.4 (Aug. 2002), pp. 325–340. ISSN: 02608774. DOI: 10.1016/S0260-8774(01)00173-X.

[125] Sharareh Salar-Behzadi, Stefan Toegel, and Helmut Viernstein. “Innovations in Coating Technology.” In: *Recent Patents on Drug Delivery & Formulation* 2.3 (Jan. 2008), pp. 209–230. ISSN: 2212-4039.

[126] Roy Jackson. *The Dynamics of Fluidized Particles*. Cambridge: Cambridge University Press, 2000, p. 352.

[127] Daizo Kunii and Octave Levenspiel. *Fluidization Engineering*. 2nd ed. Boston: Butterworth-Heinemann, 1991, p. 491.

[128] John F. Davidson. *Fluidization*. Ed. by J. F. Davidson. London: Academic Press, 1971, p. 874.

[129] Dalibor Jajcevic et al. “Large-scale CFD–DEM simulations of fluidized granular systems.” In: *Chemical Engineering Science* 98 (July 2013), pp. 298–310. ISSN: 00092509. DOI: 10.1016/j.ces.2013.05.014.

[130] Vinayak S. Sutkar, Niels G. Deen, and J. A. M. (Hans) Kuipers. “Spout fluidized beds: Recent advances in experimental and numerical studies.” In: *Chemical Engineering Science* 86 (Feb. 2013), pp. 124–136. ISSN: 00092509. DOI: 10.1016/j.ces.2012.06.022.

[131] Paul Frake et al. “Process control and end-point determination of a fluid bed granulation by application of near infra-red spectroscopy.” In: *International Journal of Pharmaceutics* 151.1 (May 1997), pp. 75–80. ISSN: 03785173. DOI: 10.1016/S0378-5173(97)04894-1.

[132] Martin Andersson et al. “Quantitative analysis of film coating in a fluidized bed process by in-line NIR spectrometry and multivariate batch calibration.” In: *Analytical Chemistry* 72.9 (May 2000), pp. 2099–108. ISSN: 0003-2700.

[133] Min-Jeong Lee et al. “Dynamic Calibration for the In-Line NIR Monitoring of Film Thickness of Pharmaceutical Tablets Processed in a Fluid-Bed Coater.” In: *Journal of Pharmaceutical Sciences* 99.1 (2010), pp. 325–335. DOI: 10.1002/jps.

[134] Perkin Elmer. *Perkin Elmer Spectrum 400 Series Manual*. 2007.

[135] Wolfgang Witt, Ulrich Köhler, and Joachim List. "Experiences with Dry Dispersion and High-Speed Image Analysis for Size and Shape Characterisation." In: *Particle & Particle Systems Characterization* 2 (2005), pp. 2–6.

[136] Martin Rhodes. *Introduction to Particle Technology*. 2nd ed. Wiley-VCH, 2008. ISBN: 978-0-470-01428-8.

[137] Cornelis Th. J. Alkemade et al. "A review and tutorial discussion of noise and signal-to-noise ratios in analytical spectrometry - I. Fundamental principles of signal-to-noise ratios." In: *Spectrochimica Acta Part B: Atomic Spectroscopy* 33 (1978), pp. 383–399.

[138] Glenn D. Boutilier et al. "A review and tutorial discussion of noise and signal-to-noise ratios in analytical spectrometry-II . Fundamental principles of signal-to-noise ratios." In: *Spectrochimica Acta* 33B (1978), pp. 401–415.

[139] Wai K. Chen. *The Electical Engineering Handbook*. Ed. by Wai Kai Chen. Boston: Academic Press, 2005, p. 1227. ISBN: 9780121709600.

[140] Svante Wold et al. "Some recent developments in PLS modeling." In: *Chemometrics and Intelligent Laboratory Systems* 58.2 (Oct. 2001), pp. 131–150. ISSN: 01697439. DOI: `10.1016/S0169-7439(01)00156-3`.

[141] Barry R. Jennings and Kevin Parslow. "Particle size measurement : the equivalent spherical diameter." In: *Proceedings of the Royal Society of London. Series A, Mathematical and Physical Sciences* 419.1856 (1988), pp. 137–149.

[142] John Bridgwater. "Mixing of particles and powders: Where next?" In: *Particuology* 8.6 (Dec. 2010), pp. 563–567. ISSN: 16742001. DOI: `10.1016/j.partic.2010.07.001`.

[143] Hannes Preiß. "Bestimmung der Pulverhomogenität mittels Nar-Infrarot Hyper Spectral Imaging Kamera System." Diploma Thesis. Graz University of Technology, 2011.

[144] Ola Berntsson, Lars-Göran Danielsson, and Staffan Folestad. "Characterization of diffuse reflectance fiber probe sampling on moving solids using a Fourier transform near-infrared spectrometer." In: *Analytica Chimica Acta* 431 (2001), pp. 125–131.

[145] Michele Forina et al. "Validation procedures in near-infrared spectrometry." In: *Analytica Chimica Acta* 295.1-2 (Sept. 1994), pp. 109–118. ISSN: 00032670. DOI: `10.1016/0003-2670(94)80340-4`.

[146] Karl Sommer. “Mixing of Solids.” In: *Ullmann's Encyclopedia of Industrial Chemistry*. Wiley-VCH Verlag GmbH & Co. KGaA, 2012, pp. 403–419.

[147] Brenda Remy, Johannes G. Khinast, and Benjamin J. Glasser. “Polydisperse granular flows in a bladed mixer: Experiments and simulations of cohesionless spheres.” In: *Chemical Engineering Science* 66.9 (May 2011), pp. 1811–1824. ISSN: 00092509. DOI: `10.1016/j.ces.2010.12.022`.

[148] Patricia M. Portillo, Marianthi G. Ierapetritou, and Fernando J. Muzzio. “Characterization of continuous convective powder mixing processes.” In: *Powder Technology* 182.3 (Mar. 2008), pp. 368–378. ISSN: 00325910. DOI: `10.1016/j.powtec.2007.06.024`.

[149] Lakshman Pernenkil and Charles L. Cooney. “A review on the continuous blending of powders.” In: *Chemical Engineering Science* 61.2 (Jan. 2006), pp. 720–742. ISSN: 00092509. DOI: `10.1016/j.ces.2005.06.016`.

[150] Volker Kehlenbeck. “Use of Near Infrared Spectroscopy for in- and Off-Line Performance Determination of Continuous and Batch Powder Mixers: Opportunities & Challenges.” In: *Procedia Food Science* 1.Icef 11 (Jan. 2011), pp. 2015–2022. ISSN: 2211601X. DOI: `10.1016/j.profoo.2011.10.002`.

[151] Georg Weber. “Parametrisierung eines kontinuierlichen Mischers mittels Infrarotspektroskopie.” Bachelor Thesis. Graz University of Technology, 2013.

[152] Jarka Glassey et al. “Process analytical technology (PAT) for biopharmaceuticals.” In: *Biotechnology Journal* 6.4 (Apr. 2011), pp. 369–77. ISSN: 1860-7314. DOI: `10.1002/biot.201000356`.

[153] Carlo Benedetti et al. “Cohesive, multicomponent, dense powder flow characterization by NIR.” In: *International Journal of Pharmaceutics* 336.2 (May 2007), pp. 292–301. ISSN: 0378-5173. DOI: `10.1016/j.ijpharm.2006.12.014`.

[154] Jérôme Mantanus et al. “Building the quality into pellet manufacturing environment–feasibility study and validation of an in-line quantitative near infrared (NIR) method.” In: *Talanta* 83.2 (Dec. 2010), pp. 305–11. ISSN: 1873-3573. DOI: `10.1016/j.talanta.2010.09.009`.

[155] Kylee R. Goode et al. “Fouling and Cleaning Studies in the Food and Beverage Industry Classified by Cleaning Type.” In: *Comprehensive Reviews in Food Science and Food Safety* 12.2 (Mar. 2013), pp. 121–143. ISSN: 15414337. DOI: `10.1111/1541-4337.12000`.

[156] Ai T. Tok et al. “Monitoring granulation rate processes using three PAT tools in a pilot-scale fluidized bed.” In: *AAPS PharmSciTech* 9.4 (Jan. 2008), pp. 1083–91. ISSN: 1530-9932. DOI: `10.1208/s12249-008-9145-6`.

[157] Paul Frake et al. “Near-infrared mass median particle size determination of lactose monohydrate, evaluating several chemometric approaches.” In: *The Analyst* 123.10 (Oct. 1998), pp. 2043–6. ISSN: 0003-2654.

[158] Herbert Hüttlin. “Device for Treating Particulate Material.” Patent US 6,898,869. May 31, 2005.

[159] Robert L. Green et al. “In-line monitoring of moisture content in fluid bed dryers using near-IR spectroscopy with consideration of sampling effects on method accuracy.” In: *Analytical Chemistry* 77.14 (July 2005), pp. 4515–22. ISSN: 0003-2700. DOI: `10.1021/ac050272q`.

[160] Maximiliane Engler et al. “Die Lighthouse-Probe, eine neuartige Sonde für die Prozessanalytik.” In: *Chemie Ingenieur Technik* 81.8 (Aug. 2009), pp. 1114–1115. ISSN: 0009286X. DOI: `10.1002/cite.200950260`.

[161] Karl-Friedrich Klein et al. “Optical fibers in instrumental UV-analytics.” In: *Proceedings of SPIE* 7173 (2009), pages. DOI: `10.1117/12.818663`.

[162] Andrey Bogomolov et al. “In-line analysis of a fluid bed pellet coating process using a combination of near infrared and Raman spectroscopy.” In: *Journal of Chemometrics* 24.7-8 (July 2010), pp. 544–557. ISSN: 08869383. DOI: `10.1002/cem.1329`.

[163] Anna G. Mignani et al. “Anti-biofouling coatings for optical fiber sensors.” In: *Proceedings of SPIE 4578, Fiber Optic Sensor Technology and Appications*. Boston, 2001.

[164] Roland Hohl et al. “Advantages of multipoint monitoring of a hot melt coating process.” In: *European Journal of Pharmaceutical Sciences (in preparation)* (2014).

[165] Edward W. Stark and Harald Martens. “Improved Multiplicative Signal Correction Method and Apparatus.” Patent EP 0,415,401. Oct. 29, 1997.

[166] Edward W. Stark and Harald Martens. “Multiplicative Signal Correcton Method and Apparatus.” Patent US 5,568,400. Oct. 22, 1996.